Microfluidic & microrheological studies of protein interactions at the single–molecule & single–cell level

Marcus Otten

SIGILL. UNIVERSITAT. LUDOVIC. MAXIM.

München 2014

Microfluidic & microrheological studies of protein interactions at the single–molecule & single–cell level

Marcus Otten

Dissertation
an der Fakultät für Physik
der Ludwig-Maximilians-Universität
München

vorgelegt von
Marcus Otten
aus Starnberg

München, den 18. Februar 2014

Erstgutachter: Prof. Dr. Hermann E. Gaub
Zweitgutachter: Prof. Dr. Joachim O. Rädler
Tag der mündlichen Prüfung: 9. April 2014

Zusammenfassung

Das Bestreben, biologisches Leben auf der molekularen Nano-Skala zu verstehen, hat das breite Feld der Nanobiowissenschaften hervorgebracht. Die Physik unterstützt dieses Vorhaben durch die quantitative Beschreibung von Gesetzmäßigkeiten, denen diese Moleküle und ihre Wechselwirkungen unterliegen. Besonders in der molekularen und zellulären Biophysik hat sich der Schwerpunkt von einem rein genomischen Verständnis des Lebens hin zu dynamischen Prozessen und funktionalen Wechselwirkungen in Zellen und Geweben verschoben. *Proteine* nehmen an verschiedensten Aufgaben des zellulären Lebens, wie Genregulation, metabolischen Enzymreaktionen oder Zellmechanik des Zytoskeletts, teil. Sie sind daher von besonderem Interesse für das Verständnis der dynamischen Prozesse. In jeder dieser Aufgaben wechselwirken sie mit anderen Biomolekülen, sei es mit DNA in transkriptioneller Genregulation, mit anderen Proteinen in enzymatischen Reaktionen, oder als Teil von makromolekularen Komplexen wie dem Zytoskelett. Diese Wechselwirkungen und die sie beherrschenden Kräfte sind eng mit der biologischen Funktion gekoppelt.

Zur Untersuchung dieser Wechselwirkungen, sogar auf Einzelmolekül- oder Einzelzell-Ebene, wurden eine Vielzahl von Methoden entwickelt. Zudem bilden „Lab-on-a-Chip“-Systeme das biochemische Pendant zu der aus der Mikroelektronik und digitalen Revolution bekannten Miniaturisierung und Parallelisierung. Nichtsdestotrotz wurden diese beiden Gebiete, Einzelmolekül-Mechanik und Lab-on-a-chip-Systeme, bisher nicht verknüpft.

In der vorliegenden Dissertation werden Protein-Wechselwirkungen auf Einzelmolekül- und Einzelzell-Ebene mit neuartigen mikrofluidischen Lab-on-a-Chip- und mikrorheologischen Techniken erläutert. Erstens wird in einem Rasterkraftmikroskop-basierten Einzelmolekül-Kraftspektroskopie-Experiment ein Mikrofluidik-Chip zur Untersuchung der Molekularmechanik von *in vitro* synthetisierten Proteinen benutzt, in einem direkten Format vom Gen-Array zur Proteinmechanik. Dies ermöglicht den Vergleich der Entfaltungs- oder Abriß-Eigenschaften von ganzen Protein-Bibliotheken mit einem einzigen Cantilever. Zweitens wird der „Molecular Force Assay“ (MFA), eine komparative und programmierbare Methode mit DNA-Oligomeren als Kraftsensoren, mittels Mikrofluidik miniaturisiert und parallelisiert um DNA-bindende Proteine in einem Prototyp-Experiment mit der Endonuklease EcoRI zu untersuchen. Dies erlaubt den kombinatorischen Vergleich von mehreren Proteinen mit mehreren Zielsequenzen und Referenzsensoren. Drittens werden in einem Einzelzell-Mikrorheologie-Experiment Proteine als Teil von supramolekularen Komplexen untersucht: Eine Wechselwirkung zwischen Aktin-Filamenten und Mikrotubuli und ihre Auswirkungen auf Zellmechanik und intrazellulären Transport werden identifiziert. Diese Entwicklungen und Resultate werden den Weg für Einzelmolekül-Techniken hin zu biotechnologischen Hoch-Durchsatz-Methoden in der post-genomischen Ära ebnen.

Abstract

The endeavor to understand biological life at the molecular nano-scale has given rise to the wide interdisciplinary field of nanobiosciences. The physical sciences contribute to this venture by quantitative description of laws concerning the involved constituents and their interactions. In particular, in molecular and cellular biophysics, focus has shifted from a purely genomic view of life to dynamic processes and functional interactions in cells and tissues. *Proteins* are the workhorses of cellular life and involved in tasks as diverse as gene regulation, enzymatic reactions of the metabolism or cytoskeletal cell mechanics. They are thus of special interest to understanding these dynamics. In each of these tasks, they interact with a variety of biomolecules, be it with DNA in transcriptional gene regulation, with other proteins in enzymatic reactions, or as part of macromolecular assemblies such as the cytoskeleton. These interactions and their governing forces have been found to be closely related to biological function.

A range of methods have been developed to study these types of interactions, even at the single–molecule or single–cell level. At the same time, the miniaturization and parallelization known from microelectronics and the digital revolution, have found their counterpart in biochemical laboratory techniques in the form of microfluidic lab–on–a–chip technologies. Nevertheless, these two fields of single-molecule mechanics and lab–on–a–chip parallelization have so far resisted conjunction.

In the present thesis, the outlined question of elucidating protein interactions at the single-molecule or single-cell levels is tackled with novel microfluidic lab–on–a–chip and microrheology technologies. First, in an atomic force microscopy (AFM)–based single–molecule force spectroscopy study, a microfluidic chip is employed to probe molecular mechanics of *in vitro* synthesized proteins in a streamlined format from gene array to protein mechanics. This enables the screening of entire libraries of proteins with respect to their unfolding or rupture properties with a single cantilever. Second, the molecular force assay (MFA), a comparative and programmable assay to collect significant statistics by using surface-bound DNA oligomers as force sensors, is miniaturized and parallelized using microfluidic chip technology to tackle questions concerning DNA-binding proteins in a proof–of–principle study on the endonuclease EcoRI. This allows for combinatorial probing of multiple proteins against multiple target sequences and reference sensors. Third, in a single–cell microrheology experiment, proteins are studied as part of supramolecular, cytoskeletal assemblies and an interaction between actin filaments and microtubules is identified with respect to cell mechanics and intracellular transport. These developments and findings will pave the way for single-molecule techniques to follow biotechnological advances in terms of high throughput in the post-genomic era.

Contents

1 Introduction

A growing body of interdisciplinary research at the intersection between biology, chemistry, and physics is concerned with *biologically* relevant questions, involving the building blocks of the animate world, ranging from single DNA or protein molecules to cells and further to organisms. The answers to these questions have been found to require knowledge about phenomena at the *nano-scale*. In this area of *nanobioscience*, fundamental research has considerably gained ground, notably with the ability to create and manipulate artificial objects at the nanoscale [1,2], to read and decipher biological information [3,4], and to apply these insights for diagnostic and therapeutic purposes [5, 6].

Considerable as these advances, *e.g.* in genomics, might be, it has also become clear that interest is increasingly shifting towards *interactions* between molecular constituents, rather than the static information encoded in genes [1].Thus, the study of interactomes [7] or gene regulatory networks [8] are constantly gaining attention. In both cases, proteins play a central role, as do their interactions with other proteins in the former case and with DNA sequences in the latter case. Furthermore, the interactions of proteins as part of macromolecular assemblies are essential to understanding cell behavior. The study of entire networks of interaction partners – interactomes or gene regulatory networks – intrinsically requires large amounts of data, for not only the *nodes* of the networks but also their connecting *edges* are probed. When interactions are studied, the governing forces are of particular interest from a physicist's perspective. On the single protein scale, force is closely related to function, exemplarily demonstrated in the case of mechanically activated enzymes [9]. In analogy, in single cells macromolecular structures such as the cytoskeleton are closely related to force generation, transmission, and sensing [10].

At the same time, lab–on–a–chip technologies have immensely contributed to the parallelization, miniaturization and comparability of scientific methods [11], in particular in the nanobiosciences. Microfluidic technology and large–scale integration are prominent examples of lab–on–a–chip implementations. They have helped to further develop existing protocols and enabled the invention of new methods. Thus, they are perfectly suited for the study of these data–intensive networks. Nevertheless, the most widespread lab–on–a–chip methods still rely on ensemble averaging for ease of use. Recent advances in non-averaging single–molecule techniques have for the most part resisted integration into high–throughput methods. Singular examples of high–throughput single–molecule experiments are primarily found in the field of sequencing technologies [3, 4] and demonstrate the disruptive effect of combining single–molecule methods with high throughput: Previous sequencing technologies have been virtually outpaced.

The scientific scope of this thesis thus lies at the intersection of interaction studies of single proteins as part of larger networks and their potential integration into parallelized experimental approaches for higher throughput and facilitated comparability. More specifically, it addresses questions concerning the miniaturization and parallelization of single–molecule or single–cell studies of protein interactions.

---

[1] Genomes are not static on an evolutionary time-scale. Furthermore, epigenetic effects do introduce changes over the course of a life-time. Nevertheless, dynamic response to external and internal stimuli occurs at other levels, such as ion channel switching, signaling cascades or transcriptional regulation, rather than at the genomic level. At these time-scales, the genome can be considered static.

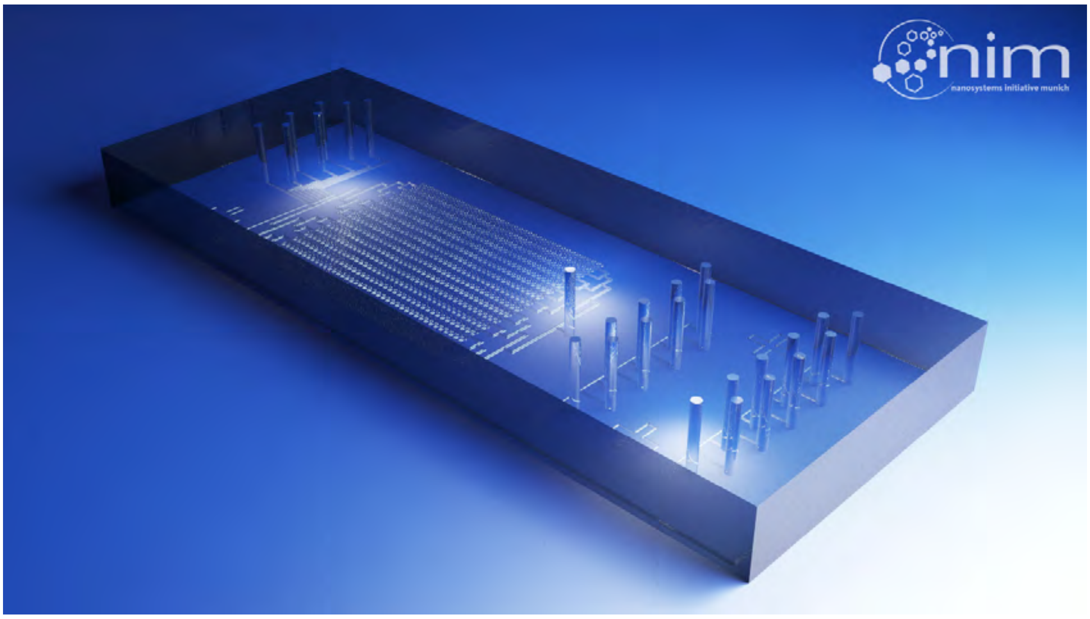

Figure 1: **Lab–on–a–chip** technologies and microfluidic devices have advanced miniaturization and parallelization in nanobioscience laboratory techniques. Shown here is an artistic rendering of the microfluidic chip used in the context of this thesis. Image by C. Hohmann, Nanoinitiative Munich (NIM).

To contribute to the elucidation of this question, three studies are described in the present thesis, which all are devoted to proteins and the forces governing their interplay with other proteins, with DNA, or as part of a macromolecular assembly. The method of choice is – wherever fit – a microfluidic chip. Before diving into the heart of this work, I will sketch the scientific context with a particular emphasis on the interactions of interest, the introduction of relevant methodology, and an overview of the field of lab–on–a–chip technologies.

2 Scientific context

To foster understanding of what governs life at the micro– and nano–scale, the study of life's "elementary particles", the biomolecules, has long been at the center of fundamental life–science research. A physicist's perspective on "elementary particles"cannot be complete without a profound understanding of the interactions and forces governing their interplay. Therefore, the methods to study these biomolecular interactions and the knowledge about them have evolved rapidly over the past decade.

To illustrate the scientific context of the work presented in this thesis, this chapter serves a three–fold purpose: First, an overview of the different types of molecular interactions of interest in this thesis is given: interactions of proteins with other proteins, with DNA, or as part of a macromolecular assembly. Second, the previous method development work is sketched. Three methods related to interaction force measurements, which are used and further developed in this thesis are the core interest of this section. And third, the relatively new field of microfluidics and lab–on–a–chip is introduced. Some examples of how it transformed existing methods or enabled new methods are given, with an exclusive focus on nanobiotechnology.

2.1 Molecular interactions

2.1.1 Protein–protein interactions

Proteins are the functional workhorses of living cells, carrying out tasks ranging from enzymatic reactions in metabolism to stimulus response. In most of these tasks, they interact with other proteins. Especially palpable is the case for enzymatically active proteins. More often than not, distortion of the protein–protein interaction interface or misfolding are disease–related [12,13]. As a result, the pair–wise interactions of proteins are at the core of current efforts of protein engineering and drug design.

Two hypotheses for the pair-wise interaction of proteins were formulated on the basis of data from X-ray crystallography and refined by nuclear magnetic resonance (NMR) [14] and molecular dynamics (MD) simulations [15]. These hypotheses are named *induced fit* and *conformational selection* [16]: The induced fit involves a stepwise conformational change upon binding. Conformational selection, on the other hand, presumes a dynamic equilibrium of multiple configurations, one of which is selectively favored by the binding partner and consequently more frequently populated upon binding. Both models rely on a free energy landscape, which explains folding of binding partners into a functional state, and on the presence of hot spots, which are interface regions with high structural conservation, high density and a particular amino acid composition [17].

Building on this knowledge, focus shifted towards system–level understanding of entire networks of proteins and their interactions. Analogous to genome studies, these interactome studies focus on a few model organisms, primarily *Saccharomyces cerevisiae* [18], *Caenorhabditis elegans* [19], and *Drosophila* *melanogaster* [7]. The acquired amount of data is impressive [1] and can only be handled by computational *in silico* methods and graph theory [20]. Nevertheless, the knowledge about these system–level networks is biased: statistical bias favors a few cellular environments due to experimental constraints. Furthermore, highly expressed or more ancient, conserved proteins are overrepresented [20].

Contrary to simple identification of binding partners in high–throughput, some methods have contributed to relate force and function for single protein pairs [21], which is particularly interesting in the case of enzymes. The quantitative characterization includes information about the energy landscape, such as potential widths and dissociation rates.

Model system: Cohesin–Dockerin interaction

Figure 2 introduces a particularly intriguing class of enzymes, presented in the context of this thesis and involved in biomass degradation by multimodular protein assemblies, the cellulosomes [22]. These assemblies are directed by a strong and high–affinity protein–protein interaction between dockerin and cohesin. Their affinity is characterized by a dissociation constant in the pM range and driven by a double 22-residue calcium binding loop–helix F–hand motif, forming the dockerin interface [23]. Cellulolytic enzymes each bear a dockerin module and can thus modularly bind to the scaffoldin on the cell wall presenting multiple cohesin modules.

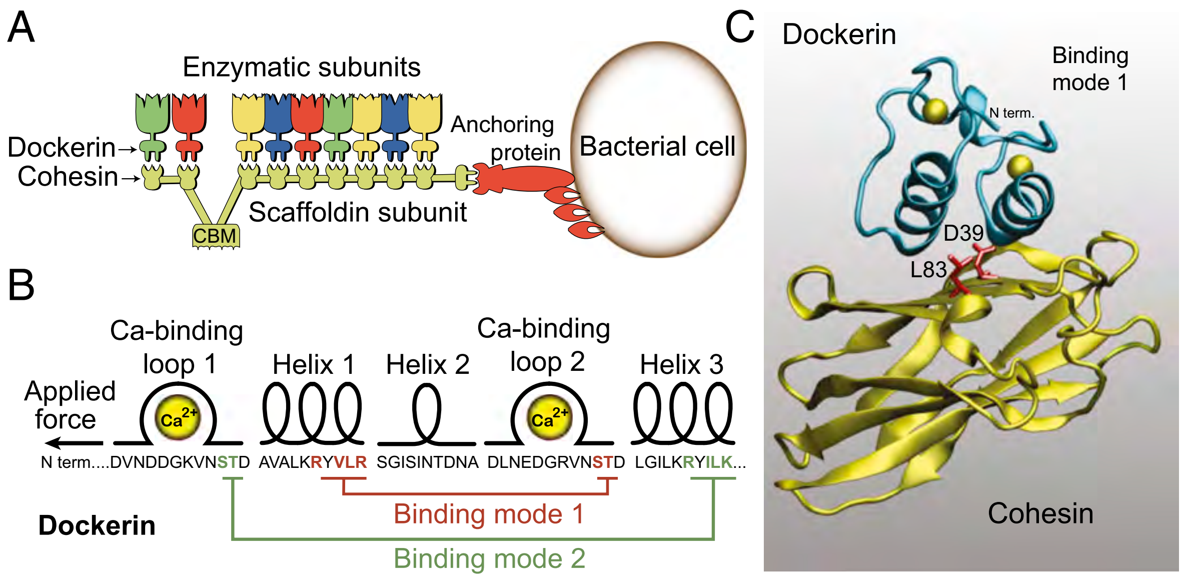

Figure 2: Cohesin–Dockerin interaction (A) Dockerin and cohesin proteins establish high–affinity and high–rupture–force binding between enzymatic subunits and a scaffoldin protein of cellulosomes on the outer cell walls of cellulolytic bacteria, *e.g. C. thermocellum*. **(B)** The binding interface of dockerin shows a double calcium binding loop–helix F–hand motif (black). Cohesin can bind to this interface in two modes (red and green). **(C)** Crystal structure of both dockerin (blue) and cohesin (yellow) in binding mode 1. reproduced from Ref. [23]

---

[1] Yeast is arguably best studied, with an estimated 50% of interactions identified. Although, the numbers of involved proteins and numbers of interactions found in different studies range from 1200 interactions (of 1000 proteins) to 11.000 interactions (between 3000 involved proteins).

2.1.2 Protein–DNA interactions

Proteins and DNA interact in a variety of contexts in all living systems, including immune response, mismatch repair and gene regulation. The immune system relies on the recognition of pathogenic nucleic acids by dedicated proteins [24]. DNA-damage response proteins are involved in detecting, signaling and repairing endogenous and environmental damage to the genetic material of an organism [25] [26].

Nonetheless, the most prominent example of interaction between proteins and DNA occurs in transcriptional gene regulation, when transcription factors bind to genes – typically in close proximity to the promoter – in order to activate or repress the RNA polymerase binding and activity [8]. Taking the example of transcription factor binding, it has recently become evident, that different measures must be combined to fully understand the underlying mechanisms [27]. These measures include binding force [28], specificity [29, 30], affinity [31], and turnover [32]. Compared to binding and turnover dynamics, mere occupancy levels are not reliable in predicting functional regulation [33].

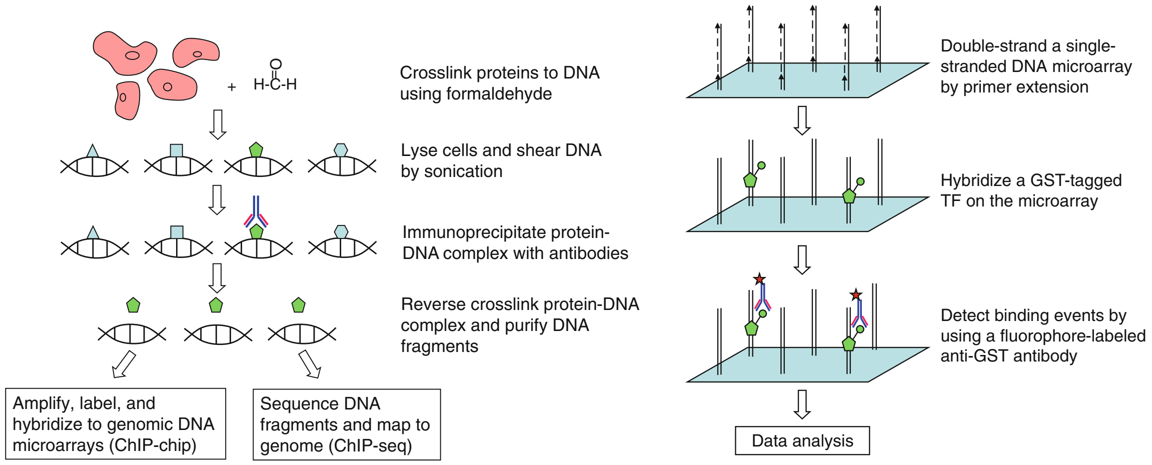

(a) Chromatin-immunoprecipitation (ChIP) **(b)** Protein-binding arrays (PBM)

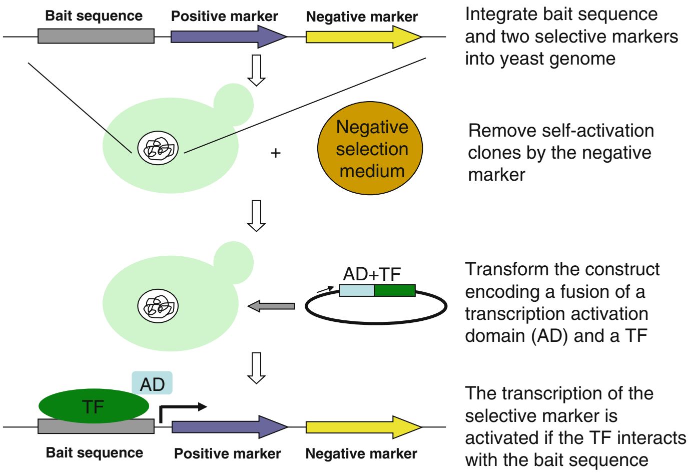

(c) Yeast-one-hybrid (Y1H)

Figure 3: Methods to study protein–DNA interactions, reproduced from Ref. [34], ©Springer Basel AG 2010, with kind permission from Springer Science and Business Media.

This central and complex role of protein–DNA interactions has spurred the development of a wide range of methods to study them. The most widespread can be classified as based on yeast–one–hybrid (Y1H) [35, 36], chromatin–immunoprecipitation (ChIP) [37] or protein–binding arrays (PBM) [38, 39], as summarized in Figure 3. Each one of these has its intrinsic strengths and weaknesses. ChIP detects the interactions in their physiological *in vivo* environment, but requires specific antibodies for precipitation. If one protein is to be screened against a wide range of binding sequences, a PBM approach is typically chosen, although high amounts of the protein are required and mostly high affinity sequences will be detectable. Y1H is thus a complimentary approach in the sense that it detects binders to a single given DNA sequence.

An additional challenge is the growing need for high–throughput implementations of these established methods, for example in yeast–one–hybrid as proposed by Hens *et al.* [40]. Currently, no single method is known, which works without specific antibodies and is capable of screening multiple DNA sequences against multiple proteins at high sensitivity or resolution. Given the importance of protein–DNA interactions in living systems, the development of improved methods is thus inevitable.

Model system: EcoRI

For many of these protein–DNA interaction detection methods, the restriction endonuclease EcoRI from *Escherichia coli* has emerged as a standard proof–of–principle system before they are applied to physiologically more relevant or complex proteins. As a homodimer, it presents a high affinity and specificity to its preferred (palindromic) binding sequence 5'-GAATTC-3' (*cf.* Figure 4), which it cleaves by hydrolysis in the presence of its cofactor Mg^{2+} [41].

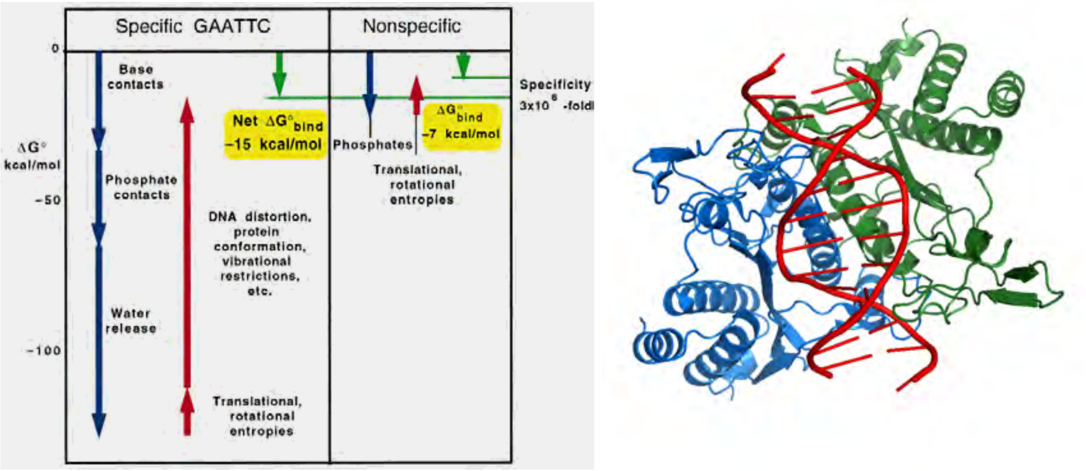

(a) Energetic components.

(b) Crystal structure.

Figure 4: EcoRI binds its target DNA sequence highly specific as a homodimer. **(a)** The energetic components differ between specific (left) and nonspecific (right) binding and show both favorable (blue) and unfavorable (red) contributions to yield a difference in net binding free energy ΔG (green). **(b)** The crystal structure shows two EcoRI monomers (blue and green) forming a homodimer to bind to their consensus dsDNA ligand (red). (a) reproduced from Ref. [42] ©1997 John Wiley & Sons, Inc., with kind permission from John Wiley and Sons. (b) rendered from PDB code 1ERI, Ref. [43].

The energetic contributions, shown in Figure 4 show conceptually different thermodynamic driving forces: The nonspecific complex is formed with any other sequence than the consensus sequence and is enthalpically driven by formation of bonds between protein and *DNA phosphates*, whereas the specific complex with the consensus sequence additionally presents bonds between protein and *DNA bases*, and energetic contributions based on the hydrophobic effect. These additional contributions are necessary to overcome the entropically driven restrictions of the rotational and translational freedom [42].

2.1.3 Interactions of macromolecular assemblies

Conserved through all branches of life, the main cellular constituents can be classified in four simple classes: nucleic acids, amino acids, sugars and fatty acids. These monomers assemble into polymers, typically DNA/RNA, proteins, polysaccharides and lipids, respectively. The underlying building schemes are astonishingly solid and yield macromolecules which surpass their building blocks in size by orders of magnitude: For example, amino acids have an average molecular weight of approximately $110\,Da$, but the giant muscle protein titin – assembled from amino acids alone – is $3.6 \cdot 10^6\,Da$ in size. The involved length scales are thus very different and the interactions governing their interplay accordingly disparate. In some cases, these macromolecules can be assembled non–covalently into even larger structures. Examples of macromolecular assemblies include membranes, viral capsids, enzyme complexes, and protein filaments.

Model system: Actin filaments and microtubules

In the context of this thesis, one particular pair of macromolecular assemblies was chosen to be studied in detail *in vivo*: actin filaments (AF) and microtubules (MT), two main constituents of the cytoskeleton. They are both assembled from polypeptide subunits: actin and tubulin. Actin filaments are typically organized in the cortex, beneath the plasma membrane. MT are typically stretched radially outward from the centrosome. The cytoskeleton in general, and AF and MT in particular, are involved in a series of physiologically relevant phenomena, including cell division [44], mechanical stimulus response [10], and migration [45].

Various modes of interaction between actin filaments and microtubules have been found and studied. An important distinction must be made between regulatory and structural interactions [46]. An exemplary *regulatory* interaction is mediated by the GTPase RhoA, which responds to MT shortening [47] by inducing MT stabilization [48] and actomyosin contraction [49]. *Structural* interactions on the other hand typically involve mechanical contact, for example *via* plectin [50] or some molecular motor proteins binding both to microtubules and actin filaments and thus being susceptible of mediating interactions between the two macromolecules.

Besides its many important roles in cell shape, migration and division, the cytoskeleton plays a central role in intracellular transport [51], both in a directed, ballistic mode and in a diffusive manner. For reasons of crowding, caging and obstruction [52], these diffusive phases are not perfectly Brownian, which is hypothesized to be partially due to cytoskeleton components, although the exact contributions and effects remained to be elucidated.

2.2 Force spectroscopy and force assays

The previous section described three types of molecular interactions involving proteins, each one with a representative model system. Accordingly, each of these interactions and model systems have brought about specifically suited methods to study them. It is of core relevance in the context of this thesis to recapitulate common points and differences between them.

2.2.1 Single–molecule AFM force spectroscopy

Designed originally for imaging purposes on the basis of a scanning tunneling microscope, the atomic force microscope (AFM) [53] relies on a cantilever, whose vertical position or deflection is typically determined *via* the reflection of an infrared (IR) laser off its tip onto a quadrant photodiode. Beyond the use as an imaging microscope, it was soon adapted to record forces rather than simple height differences of the cantilever by determining its spring constant. The force spectroscopy of receptor–ligand interactions, such as biotin–avidin, was a prime example for its use in biological systems [54].

More recently, a combined Total Internal Reflection Fluorescence (TIRF) – AFM was proposed to facilitate and improve on single–molecule studies involving fluorescence imaging [55]. This combined setup is shown in Figure 5 and allows for the simultaneous confocal surface imaging from below the sample and the access with the AFM cantilever from above for single–molecule force spectroscopy experiments.

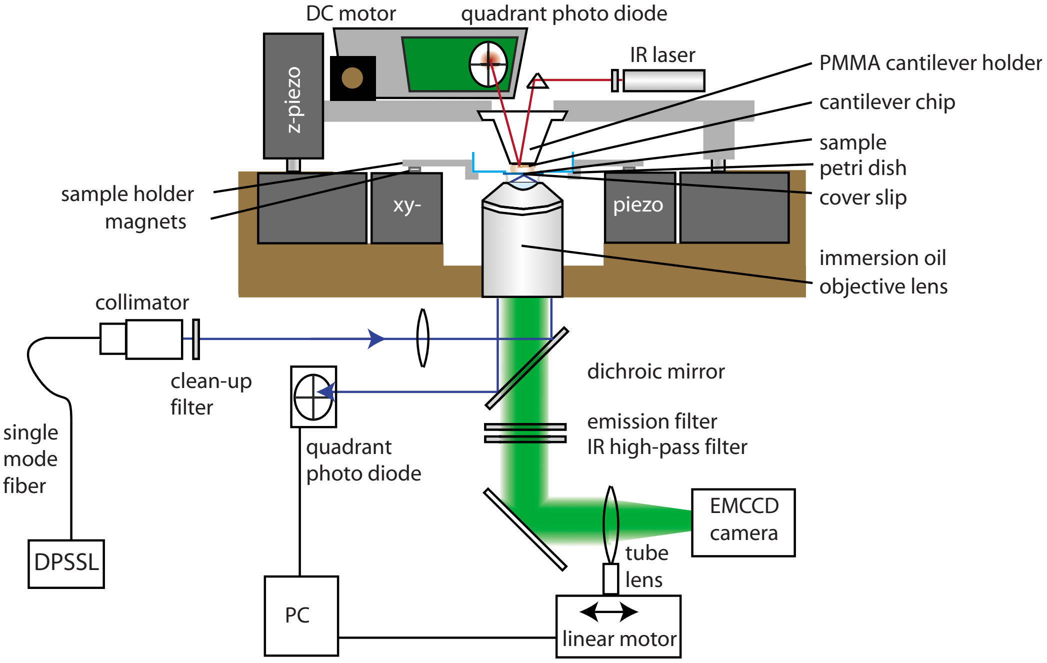

Figure 5: Combined TIRF/AFM setup: The sample (blue) is accessed from above with an atomic force microscope (AFM) (grey), featuring IR laser, cantilever, photodiode and z-piezo and from below with a Total Internal Reflection Microscope (TIRF) (black) featuring an excitation laser, filters, a motorized tube lens and an EMCCD camera. The sample and cantilever can be moved *via* a xy-piezo stage. Reprinted with permission from Ref. [55]. ©2009, AIP Publishing LLC.

In single–molecule force spectroscopy (SMFS), the recorded force–extension traces are then typically transformed into contour length space using polymer elasticity models [56]. The most widely used model, the worm–like–chain (WLC) model, is based on the assumption of a thermally fluctuating, flexible rod with an exponential correlation function of the rod element directions. Other models include the freely–jointed–chain (FJC) model and the freely–rotating–chain (FRC) model. Transformation into contour length space facilitates data interpretation, for the length increment is closely related to the number of monomers in the ruptured element, for example the number of amino acids in a protein of interest. It has become clear, that the interaction forces and the function of molecules are closely related on the single–molecule level [57]. The mechanoenzymatics relating force and function have exemplarily been elucidated with the protein titin kinase [58]: AFM–based SMFS revealed that mechanical strain–induced conformational changes unveil the ATP binding site necessary for lifting the autoinhibition of the kinase enzymatics. The capabilities of AFM–SMFS continue to be expanded, as highlighted by a recent investigation, which showed force–extension traces at high–speed with retraction velocities of up to $1\,mm \cdot s^{-1}$, comparable to the μs-timescales studied by steered molecular dynamics (MD) simulations [59].

AFM–SMFS has brought about important insights into the dynamics of single molecules. The most widespread alternatives to study similar questions are magnetic tweezers and optical traps [60]. Both use external fields to control micrometer–sized beads. In the case of magnetic tweezers paramagnetic beads are subjected to forces in a magnetic field gradient with the advantage of good force resolution. Optical traps, on the other hand, rely on momentum transfer upon refraction, reflection and scattering of light, generating forces towards the focal point of a laser beam.

2.2.2 The molecular force assay MFA

Despite the numerous advantages of single–molecule force spectroscopy using an AFM cantilever, some biological investigations call for statistics from ensembles of a high number of probes. The experimental technique known as molecular force assay (MFA) addresses exactly this need [61].

It is based on the assembly of two molecular bonds in series on a surface, one probe and one reference bond. A force is applied by coupling to a retracting surface. The coupling typically occurs via biotin–avidin interaction. After retraction, fluorescent labels reveal the bond rupture site, as shown in Figure 6. The probe bond rupture probability can be shifted by a potential binder, such as a DNA-binding protein. The molecular force assay boasts important advantages: First, the high surface density of force probes and parallel force load allow for significant statistics in a single run. Second, the active force load makes strong binders up to pM dissociation rates experimentally accessible. Third, the sensor being a single molecule, the noise is reduced to a minimum and sensitivity is high. Furthermore, binder molecules do not require fluorescent labeling, in particular, no cloning or immunolabelling are needed. Finally, the reference bond strength can be tuned over a wide range *via* its oligomer length.

The applications of the molecular force assay in its classic, macroscopic form are numerous and span a wide variety of molecular interactions: Properties of DNA were elucidated in detail from detection of mismatches [62] to epigenetic modifications by methylation [63] or hydroxymethylation [64]. Beyond pure DNA probes, the effect of binding by polyamides, transcription factors and nucleases [65] and the interaction between RNA and proteins [66] were studied in high detail.

2.2.3 Measuring intracellular dynamics and forces

The presented methods of SMFS and MFA yield remarkable insight into the dynamics and interactions between single molecules. When it comes to single–cell dynamics, the collective behavior of supramolecular assemblies needs to be taken into account. For the generation, transmission and sensing of forces, the assembly of interest is the cytoskeleton [10]. In addition, intracellular dynamics occur

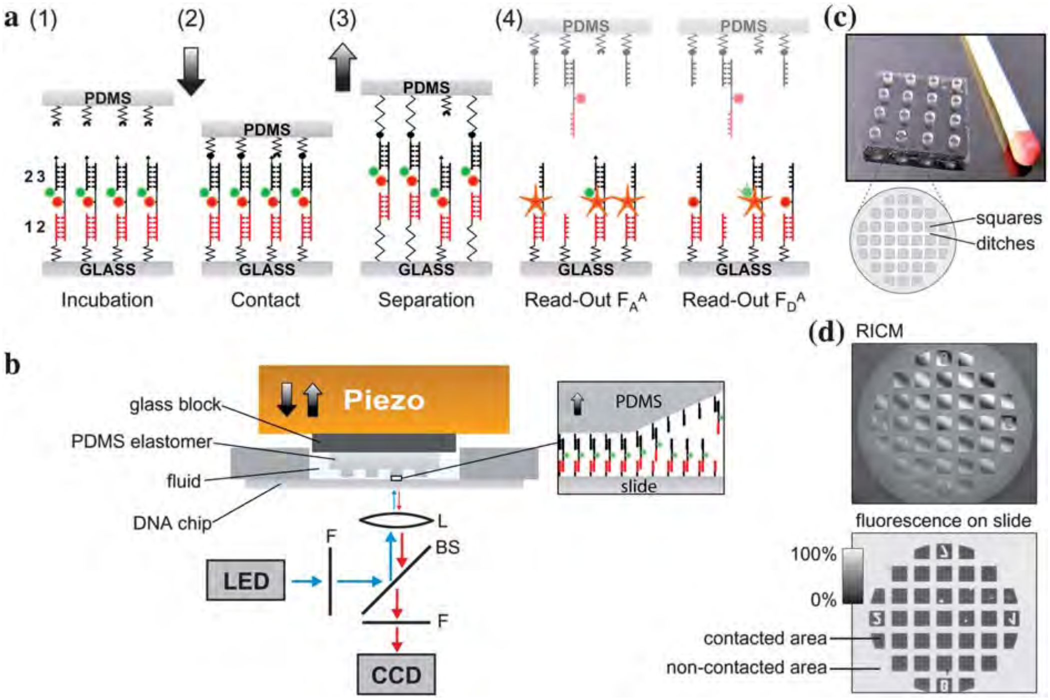

Figure 6: Classical **Molecular Force Assay (MFA).** **(a)** The molecular principle of the MFA builds on a sequence of five steps: incubating the molecular force probes on the lower glass surface; establishing contact with the elastomeric (PDMS) top surface; applying rupture forces by surface separation; fluorescence readout of the rupture signal; and fluorescence read–out of the coupling efficiency signal. **(b)** The macroscopic setup of the classical MFA features a piezo to establish contact between PDMS and glass surfaces, a fluid chamber, and an inverted epifluorescence microscope with LED excitation and CCD camera. **(c)** The elastomeric top of the classical MFA feature 16 macroscopic pillars with 100μ m-sized elevations. **(d)** The readout of Reflection Interference Contrast Microscopy (RICM) shows approach and retract dynamics. The readout of fluorescence signal after contact and separation reveals relative rupture probabilities. ©The Royal Society of Chemistry 2011; Reproduced from Ref. [61] with permission of The Royal Society of Chemistry.

on a wide range of timescales [67]: Switching of ion channels upon external stimulus is a matter of seconds; subsequent responses by the cell involving signaling cascades take minutes to hours; ultimate cell fate (division, differentiation, apoptosis) may take days. At the same time, the behavior of cell populations is heterogenous and noisy, so single–cell data is collected for quantitative studies of their dynamics. Accordingly varied are the *methods* to study each of these events and dynamics and their plurality is beyond the scope of this thesis. Many are based on fluorescence imaging, some label–free, others use external probes such as cantilevers. A remarkable review of the specific uses and applications in single–cell studies for each of these has been given by Spiller *et al.* [67].

Nevertheless, these imaging techniques do not allow direct visualization of the underlying forces. Therefore, the acquired data must be processed in numerous ways. When probing the elastic properties with an AFM cantilever [68], the recorded force–indentation curves can be fitted with a Hertz/Sneddon model to obtain Young's moduli [69]. An exemplary study involving the effect of cytoskeleton depolymerizing drugs found characteristic responses associated with actin filaments and microtubules [70]. Alternative approaches include the *in vitro* reconstitution of purified cytoskeletal components and the measurement of their mechanical response. There, a clear differentiation between entropic and elastic contributions to elasticity can be made [71]. Based on these microrheology frameworks, an alternative model of the living cell cytoplasm has been proposed, which bears close resemblance to soft glassy materials, with scaling laws of the rheological moduli and a continuous distribution of relaxation times [72].

Another particularly popular variant is based on the tracking of internalized particles [73]: The location of particles is determined in high precision by Gaussian fits to their fluorescence signal. The recorded single–particle traces can then be analyzed, typically by calculating Mean Squared Displacements (MSD) in the lagtime space.

$$\langle \Delta R^2(\tau) \rangle = \langle (\vec{R}(t'+\tau) - \vec{R}(t'))^2 \rangle_{t'} = A \cdot \tau^{\alpha}$$

Some qualitatively different regimes are typically distinguished, according to the value of the MSD exponent α:

MSD exponent	**regime**
$\alpha = 0$	no net movement
$\alpha < 1$	subdiffusive
$\alpha = 1$	Brownian
$\alpha > 1$	superdiffusive
$\alpha = 2$	directed or ballistic

These MSD curves can then be transformed into frequency–space yielding viscoelastic moduli. Low values of $\alpha \approx 0$ correspond to elastic–like behavior (the in–phase rheological response function $G'(\omega)$), whereas $\alpha \approx 1$ is characteristic of viscous behavior (similar to the out–of–phase rheological response $G''(\omega)$). Lag–time dependent motion exponents $\alpha(\tau)$ correspond to viscoelastic materials with frequency–dependent moduli $G^*(\omega)$. In the context of this thesis, a *Local MSD* analysis algorithm is of particular interest: A rolling window screens the data subtrace by subtrace and calculates local motion parameters (in time), namely the effective diffusion constant and the MSD exponent [74].

2.3 Microfluidic lab–on–a–chip technologies

In an effort to miniaturize, parallelize and automize typical biochemical tasks from established laboratory processes, the fields of lab–on–a–chip in general and microfluidics in particular have spurred innovation over the past decade with significant success both in academic research and in commercial applications. The diversity of methods and applications is astonishing, ranging from pressure driven laminar flow to droplet–based digital microfluidics. This section covers the multilayer soft lithography technique used in the context of this thesis and gives an overview of alternative approaches.

2.3.1 Multilayer soft lithography and the MITOMI chip

One prominent variant of microfluidics is the multilayer soft lithography technique pioneered by Unger *et al.* [75] and depicted in Figure 7. Molds are manufactured by spin–coating positive or negative photoresist layers on silicon wafers, exposing them to radiation through a high–resolution transparency mask, and finally developing the structures. The molds can in a second step be repeatedly replica–molded with elastomeric materials, such as polydimethylsiloxane (PDMS) [76]. Different wafers yield different layers, both spin–coated thin layers and poured thick layers. Multiple layers can be aligned and bonded to form a single device. Bonding occurs thermally by relative excess of base in the flow

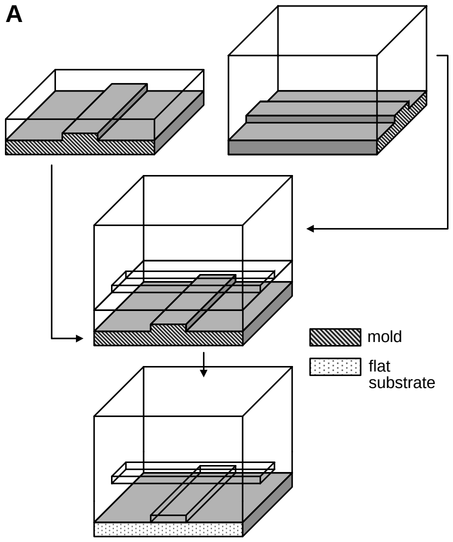

Figure 7: Multilayer Soft Lithography uses two silicon wafers, whose features are replica–molded with polydimethylsiloxane elastomer (top). The molds are aligned onto each other (middle) and bonded to form a single device (bottom) with hollow channels for microfluidic experiments. ©AAAS 2000. From Ref. [75]. Reprinted with permission from AAAS.

layer and of curing agent in the control layer. This lithography–based principle thus transfers advantages such as rapid prototyping and ease of fabrication to lab–on–a–chip device fabrication. The use of suitable elastomers ensures the desired biocompatibility needed for devices handling proteins or living cells. Design principles [77] analogous to electronic integrated circuits yield networks of thousands of pneumatically actuated valves and are the origin of the term *microfluidic large scale integration* [78]. Simple combinations of control layer valves yield pumping or mixing units (Fig. 8).

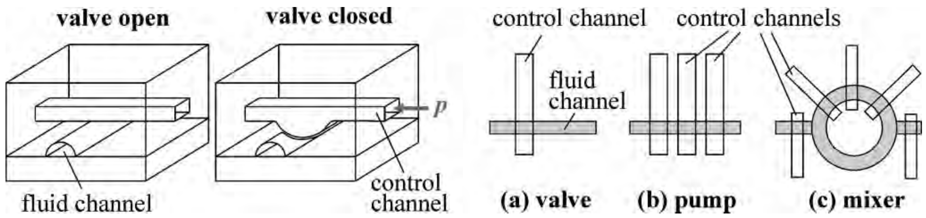

Figure 8: Pneumatic valve operation. The microfluidic devices formed by multilayer soft lithography present two channel layers: a fluid flow channel below and a control channel above. Upon pressurization of the control channel, the flow in the fluid channel is stopped, which corresponds to the actuation of a pneumatic valve. By combining multiple control channel valves, pump or mixer units can be designed. ©The Royal Society of Chemistry 2007; Reproduced from Ref. [11] with permission of The Royal Society of Chemistry.

In the context of this thesis, a particular multilayer chip design named MITOMI, acronym for *mechanically induced trapping of molecular interactions* [79], is used. Shown in Figure 9, it features hundreds of double chambers with the required valves for chamber separation and fluid flow control. One distinctive feature is the button valve in each double chamber, which can be used to seal and protect a detection area. It has been exploited in combination with *in vitro* transcription and translation of microspotted DNA to study the interaction of proteins with other proteins [80] or RNA [81]. The chip design continues to be expanded in size [82] and in its capability of fast button valve response time to record association and dissociation traces [83].

Fluid physics are highly dependent on the length scales at which the flow occurs. A very comprehensive review of fluid physics at the nanoliter scale has been published by T.M. Squires and S.R. Quake [85].

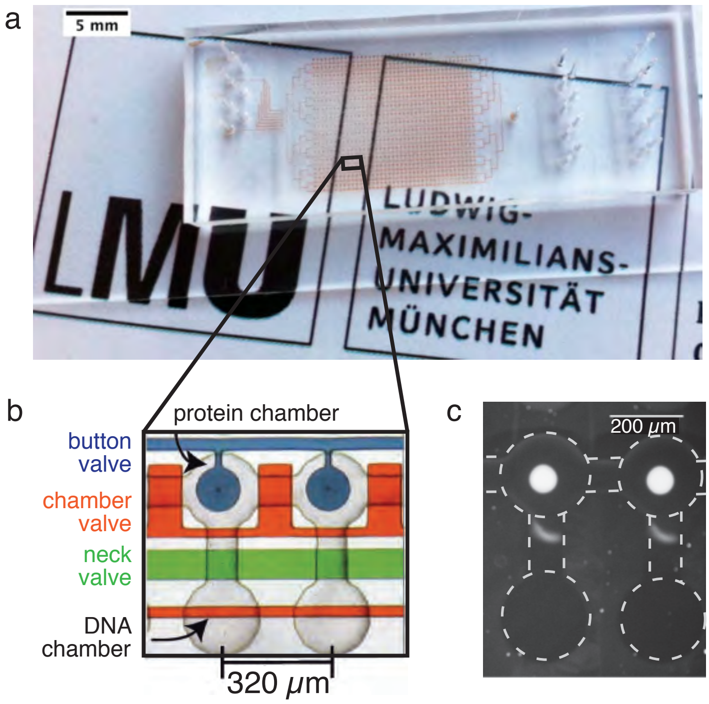

Figure 9: The microfluidic **MITOMI chip.** **(a)** shows a photograph of the 640–chamber MITOMI chip, fabricated by multilayer soft lithography and bonded onto a glass slide. Flow inlets are shown on the left, control inlets on the right. The flow layer is colored with food dye (red). **(b)** shows two of 640 double chambers in the flow layer (grey) and the superseding control layer channels (narrow) and valves (broad) for control: button valve (blue), chamber valve (red) separating double chambers and neck valve (green) separating back chambers. **(c)** shows a fluorescence micrograph signal from Green Fluorescent Protein (GFP) immobilized specifically under the button valve after selective surface modifications. (b) reprinted by permission from Macmillan Publishers Ltd: Nature Biotechnology, Ref. [84], ©2010

It gives an excellent overview of half a dozen dimensionless numbers describing the nature of fluid flow at these length scales. The most known of these numbers, the Reynolds number, gives an estimate of the relative prevalence of inertial *versus* viscous effects. The problem of diffusive mixing is described by the Péclet number. Furthermore, the effect of boundaries and surfaces is put in a broader context of device design and applications.

An interesting development lies in the growing number of microfluidic circuits with integrated logics. These include microfluidic equivalents of high and low pass filters, logic NOT gates, diodes and transistors [86, 87]. These devices do not need external pressure sources for the actuation of the embedded control layer functionalities, but react to changes in flow layer pressures and are thus a closer relative to integrated microelectronic circuits.

2.3.2 Biotechnological applications

Biotechnology is arguably the area of applications which was the fastest adaptor of microfluidic large scale integration. A few examples ranging from chemical synthesis to single–cell sequencing shall highlight this ingenuity and future potential.

- In a widely noticed work, the labs of Hsian-Rong Tseng and Stephen R. Quake carried out an automated *multistep chemical synthesis* on a single chip in variable physical and chemical environments to produce the medically highly relevant radio–imaging probe [^{18}F]FDG [88], as depicted in Figure 10.
- Long–term controlled cell culturing in a parallel format was achieved in a *microchemostat* [89].
- Hong *et al.* have devised a chip which isolates small numbers of bacterial or mammalian cells, induces cell lysis, purifies and recovers the contained DNA or mRNA. This small–scale *nucleic*

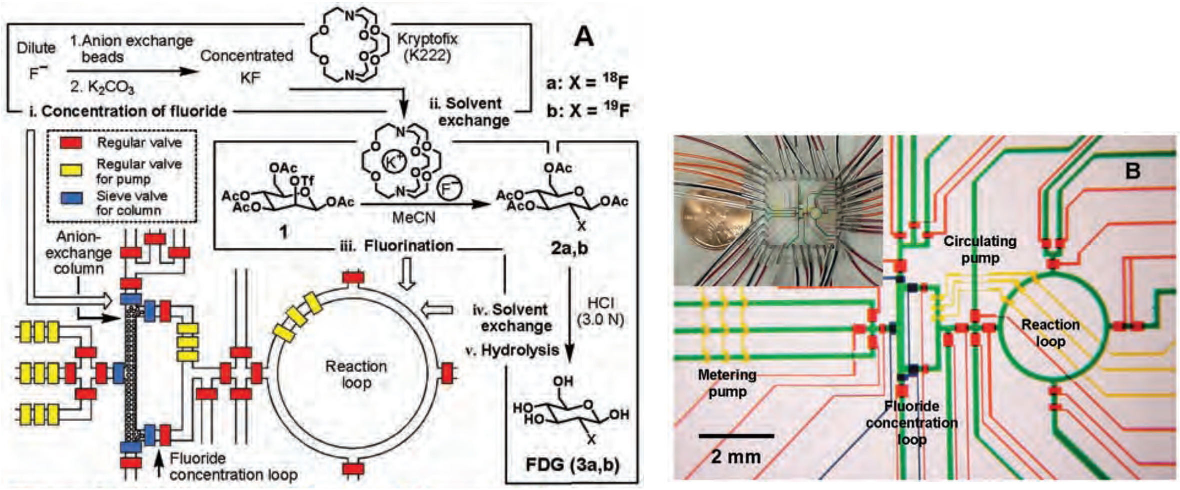

Figure 10: An example of **microfluidic integration of chemical synthesis.** **(A)** shows the microfluidic design of flow layer (black) and control valves (colored) alongside the five–step workflow from fluoride concentration (i.) to hydrolysis (v.) **(B)** shows a food dye colored micrograph of the according microfluidic chip with the flow layer (green) and the control layer (colored accordingly to (A)). ©AAAS 2005. From Ref. [88]. Reprinted with permission from AAAS.

acid processor achieves parallel purification and thus paved the way for integrated sequencing efforts [90].

- Fan *et al.* have combined these insights and designed a chip which isolates a single human cell, separates and amplifies each chromosome for subsequent use in single–nucleotide polymorphism array analysis yielding a complete human haplotype [91].

2.3.3 Diversity in microfluidics

The field of microfluidics has come a long way since the first lateral flow tests, simple point–of–care diagnostic devices based on capillary forces. A vast number of methods has emerged, which differ in ease–of–handling, high–throughput capabilities and means of liquid propulsion. The most widespread devices are driven by pressure gradients, acoustic waves, centrifugal force or electrokinetics [92]. For centrifugal microfluidics, rotation–frequency–dependent liquid transport, routing, metering, mixing and separation routines have been proposed and applied, including in a white blood immunoassay [93]. In surface acoustic wave (SAW) based implementations, droplets on a hydrophobic surface are controlled using ultrasonic waves generated by an interdigital transducer assembled on a piezoelectric layer [94].

Within the group of pressure–driven flow, one can distinguish between single–phase laminar flow (including the devices used in the context of this thesis) and droplet–based flow. Droplet–based or digital microfluidics feature picolitre volume liquid droplets in an immiscible carrier liquid or gas [96]. These droplets can be generated, handled, merged or split, and sorted (*cf.* Figure 11) with high precision making them a viable candidate for high–throughput screening with little reagent consumption. A striking demonstration of these capabilities is the implementation of high–throughput polymerase chain reaction (PCR) to amplify single molecules in droplet microfluidics [97].

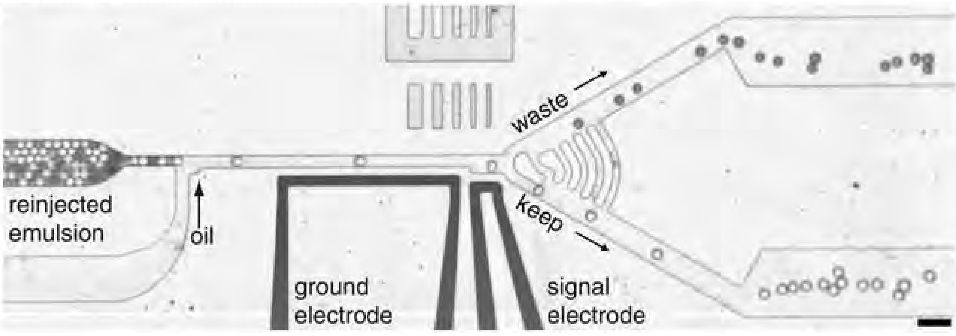

Figure 11: An example of **droplet microfluidics**: A mixture of fluorescent and non–fluorescent droplets (bright and dark, respectively) are re-injected from an emulsion (left), into a sorting device (center), where a laser interrogates their fluorescence and electrodes (bottom) deflect the fluorescent droplets into the lower channel (lower right), whereas non–fluorescent droplets are not deflected and go into the waste channel (top right). Reproduced from Ref. [95]

3 Microfluidic protein micro–arraying for single–molecule force spectroscopy

Single–Molecule Force Spectroscopy (SMFS) has immensely advanced the understanding of molecular mechanics, in particular for biomolecules. Its high precision, especially piconewton and nanometer resolution, and its independence of ensemble averaging have helped spread its merits. Nevertheless, it is intrinsically low throughput and each sample is typically prepared and probed independently, often with a different cantilever. For delicate protein samples, these considerations are particularly valid and underline the need for a systematic and parallelized preparation of protein samples for SMFS in an integrated method. Key requirements are a streamlined workflow, covalent protein immobilization, scalability, and sample purity.

In this chapter and in manuscript M1, the development of an integrated method of microfluidic protein expression, purification and covalent immobilization, followed by AFM–based single–molecule force spectroscopy is presented. It relies on the MITOMI [79] chip layout with its button valve and covalent surface immobilization *via* ybbR peptide tag [98].

3.1 Summary of associated manuscript M1

In the associated manuscript M1, the microfluidic MITOMI chip is for the first time applied for covalent protein arraying for force spectroscopy experiments. This fulfills all requirements to propel SMFS into a method of high throughput:

- The method features a direct and streamlined workflow from gene array to molecular mechanics by cell–free expression, a well–characterized protein synthesis system [99].
- Proteins are immobilized covalently onto the glass slide via a polyethylene glycol linker and the versatile, genetically encoded ybbR peptide tag.
- The approach is readily scalable. Parallelization capabilities are demonstrated using four proteins of interest: fibronectin type III, the gold standard of SMFS, spectrin, green fluorescent protein (GFP), and xylanase, an enzyme involved in plant cell wall degradation and thus of interest for next–generation biofuel synthesis.

The manuscript M1 describes the experimental workflow of this new integrated microfluidics and force spectroscopy method and its application to four proteins of interest. The genes of interest are spotted onto a glass slide by conventional microarraying technology. A microfluidic chip is aligned to this gene array. The microfluidic chip serves to functionalize the glass slide sample areas, to introduce the cell extract for *in vitro* transcription and translation, to immobilize the proteins *via* N-terminal ybbR tag and to label the sample areas fluorescently for navigation purposes. Finally, the chip is removed and the protein array is accessed from above using a cohesin–functionalized cantilever, binding C-terminal dockerin tags of the sample proteins. Thus, force–extension traces are recorded for single proteins sequentially, moving from sample spot to sample spot in the array – each one with a different type of protein but with the same cantilever. Analysis of single force–extension traces, of assembled rupture probability densities and of rupture–force-*vs.*-loading–rate populations confirms the specificity and purity of the prepared sample proteins. The yield of interpretable force curves per spot of up to 5% is comparable to classic SMFS samples and thus yields significant statistics.

In summary, the results detailed in manuscript M1 pave the way onto a new level of parallelization and integration for single–molecule force spectroscopy studies. Both protein unfolding and protein–protein unbinding studies can readily be implemented. For instance, a library of receptor mutants can be screened against a single ligand. The collected data are easily comparable when collected under identical conditions with the same cantilever. Furthermore, the chip can be used for single–molecule cut–and–paste (SMC&P) of proteins [2], one button area serving as *target* area and the surrounding button areas as *depots*.

3.2 Associated manuscript M1

From Genes to Protein Mechanics on a Chip

by
Marcus Otten*, Wolfgang Ott*, Markus A. Jobst*, Diana Pippig,
Michael A. Nash and Hermann E. Gaub
(∗ contributed equally)

submitted for peer-review to
Science (2014)

Title: From Genes to Protein Mechanics on a Chip

Authors: Marcus Otten[1,2,†], Wolfgang Ott[1,2,†], Markus A. Jobst[1,2,†], Diana Pippig[1,2], Michael A. Nash[1,2,], Hermann E. Gaub[1,2,*]*

Affiliations: [1]Lehrstuhl für Angewandte Physik, Ludwig-Maximilians-Universität, 80799 Munich, Germany, [2]Center for Nanoscience (CeNS), Ludwig-Maximilians-Universität, 80799 Munich, Germany

[†] These authors contributed equally.
* To whom correspondence should be addressed: michael.nash@lmu.de; gaub@lmu.de.

ABSTRACT

Forces are key to the function of biomolecules and single molecule force spectroscopy provides a unique means for analyzing their mechanical response. In practice, however, low experimental throughput has limited our ability to screen constructs in parallel, and in many cases only a limited number of molecular variants have been characterized. Here we describe a versatile microfluidic platform for the on-chip expression of protein constructs and the measurement of their mechanical properties at the single molecule level. We constructed microarrays of fusion proteins covalently attached to a chip surface at their N termini, bearing dockerins at their C-terminal ends. We expressed libraries of structural proteins (e.g., fibronectin tandem repeats), cytoskeletal constituents (e.g., alpha spectrin), enzymes (e.g., xylanase), GFPs and other proteins. We found that a single cohesin-modified cantilever that bound to the terminal dockerin tag of each protein remained stable over thousands of pulling cycles, enabling clear identification of the unfolding fingerprints of each protein in the array. The ability to express and covalently attach protein libraries and perform single-molecule force spectroscopy in a parallel format presents new opportunities for high-throughput screening of protein mechanical properties.

MAIN TEXT

Mechanical forces are known to play a pivotal role in biological systems, performing tasks such as guiding cell adhesion(*1*), inducing gene expression patterns(*2*), and directing stem cell differentiation(*3*). At the molecular level, mechano-sensitive proteins act as sensors and transducers(*4*), communicating the presence and direction of applied forces to downstream signaling cascades. Conformational changes in response to mechanical forces are known to modulate protein interactions, for example, by exposing cryptic binding sites(*5*), and removing autoinhibitory helices(*6*), and can be probed directly using single molecule force spectroscopy (SMFS) (*7*). SMFS is an experimental method to apply mechanical forces to individual macromolecules, and measure energetic barriers along unfolding pathways. Optical tweezers, magnetic tweezers, and atomic force microscopy(*8*) (AFM) have been used to interrogate high-affinity receptor-ligand binding(*9*), measure unfolding and refolding dynamics of individual protein domains(*10-12*), observe base-pair stepping of RNA polymerases(*13*), and identifying DNA stretching and twisting moduli(*14*, *15*).

Despite these successes, until now SMFS experiments have been significantly limited by low throughput. In SMFS, the requisite force probe (e.g., cantilever tip, bead surface) must be sparsely populated with molecules in order to maximize the likelihood of observing single-molecule interactions. Experimental data sets typically contain a majority of force-distance traces that are unusable due to the presence of too many observed molecular interactions in parallel, or no specific interactions at all. A typical yield of interpretable single-molecule interaction traces in an SMFS experiment would be 1-25%. Additionally, a general incapacity to screen libraries of molecular variants and read out the results in parallel, as is commonly done with protein and DNA microarrays, has hindered progress toward understanding sequence-structure-function relationships in these systems. In particular, preparing each protein sample and each cantilever separately increases experimental workload and gives rise to calibration uncertainties. Therefore, the ability to interrogate the mechanical behavior of different individual proteins in a parallel and streamlined format with the same cantilever would be a distinct advantage. Such a system would enable screening large protein libraries based on properties such as mechanical opening forces, interdomain mechanical signatures, and mechanically-activated catch bond behavior(*1*). Screening of these mechanical properties could find applications in biotechnology and human health studies where mechanical dysregulation or misfolding is suspected to play a role in disease pathology(*16*).

Here, we developed a platform for parallel characterization of protein mechanics in a single experiment. The method we describe achieves a considerable boost in throughput for single molecule AFM experiments. An overview of the process is shown in **Figure 1**. The process started with spotting of gene microarrays on a glass slide. Microarrays of single domain and multimer proteins were then synthesized *in situ* using cell-free gene expression, and covalently linked in defined spatial patterns to glass surfaces inside multilayer microfluidic circuits. A single cantilever was then positioned above the protein array, and used to probe the mechanical response of each protein via a common C-terminal dockerin fusion tag.

Genes encoding target proteins with identifiable mechanical unfolding signatures were first cloned, and microarrayed onto a glass slide using a microplotter system. Genes of interest were chosen such that each gene product exhibited an identifiable unfolding pattern when stretched from the N- to C-terminus by the AFM. Each target protein was expressed with flanking peptide sequences. As the N-terminal flanking sequence, an 11 amino acid ybbR tag was used as a means to covalently link the gene products to the glass surface in a site-specific manner *via* Sfp phosphopantetheinyl transferase-catalyzed reaction with coenzyme A (CoA)(*17*). As the C-terminal flanking region, a 75 amino acid cellulosomal dockerin domain from *C. thermocellum* was chosen, which served as the specific handle domain targeted by the cohesin-modified cantilever.

The gene microarray was aligned and reversibly bonded to a microfluidic chip known as MITOMI (mechanically induced trapping of molecular interactions). The chip has been used in the past for screening transcription factor consensus sequences(*18*), and mapping protein interaction networks(*19*). More recently, our group demonstrated the use of MITOMI chips for performing molecular force assays(*20*). In the current work, our MITOMI chips featured 640 dumbbell shaped unit cells in a flow layer and 2,004 micromechanical valves in a control layer. Each unit cell was equipped with pneumatic ‘neck’, ‘sandwich’, and ‘button’ valves (**Fig. 1A)** according to design principles of soft lithography (*21*, *22*). Each neck valve protected the microspotted cDNA in the back chamber from exposure to other reagents during surface patterning in the front chamber. The sandwich valves prevented chamber-to-chamber cross contamination, ensuring only a single construct was present in each sample spot. To pattern the surface in the front chamber, the button valve was actuated to shield a sample spot, allowing for BSA passivation in the surrounding area. Releasing the button valve allowed subsequent functionalization with CoA-PEG in the sample area under the button. The CoA-modified spot served as a protein-binding patch that could be covalently linked to target proteins containing an N-terminal ybbR peptide tag. Expression of the designed genes was initiated by incubating an *in vitro* transcription and translation cell extract at 37°C with the spotted cDNA in the back chamber. The synthesized proteins were then allowed to diffuse to the front chamber where they were covalently linked to the surface *via* Sfp-catalyzed reaction of surface-bound CoA with solution phase N-terminal ybbR peptide tags (**Fig. 1B)**. Partial pressurization of the button valve (*23*) was further used for tagging an outer concentric portion of the sample area with a fluorescently labeled cohesin that specifically bound to the C-terminal dockerin tag of each target protein, thereby confirming successful protein synthesis and surface immobilization (Supporting Figure S1). Finally, the microfluidic device was removed from the glass slide, providing access to the protein array from above. This microfluidic protocol thus served as a means to generate microarrays of site-specifically and covalently immobilized proteins for subsequent single-molecule force spectroscopy experiments, starting from a conventional gene array.

For fluorescence imaging and single-molecule force measurements, we used an inverted three-channel total internal reflection fluorescence/ atomic force microscope (TIRF-AFM) hybrid (*24*). The fluorescence signal from the concentric rings also supported navigation and positioning of the cantilever. During the TIRF-AFM experiment, the cantilever was positioned in the center of the fluorescent rings at known locations in the protein array (**Fig. 1C**). The cohesin-modified cantilever was used to probe the surface for expressed target proteins containing the C-terminal dockerin tag. Upon contact of the AFM cantilever with the surface, formation of a single cohesin-dockerin molecular pair allowed attachment of the target protein to the cantilever in a well-controlled pulling geometry (N- to C-terminus). We then retracted the cantilever at constant velocity and recorded force-extension traces that characterized the unfolding fingerprint of the target protein. This approach-retract process could be repeated many times at each array address across the entire microarray by moving from protein spot to protein spot to generate large statistics for each expression construct.

Each protein construct contained a C-terminal dockerin tag as a specific and high affinity handle that bound to the cohesin-modified cantilever during the force assay. Several unique features of the dockerin module made it particularly suitable in this application as a protein handle for SMFS-MITOMI. Natively, this module serves as a conserved C-terminal module found on cellulolytic enzymes of the anaerobic bacterium *C. thermocellum*(*25*). Its relatively small size of 8 kDa did not significantly add to the molecular weight of the gene products, which was an advantage since premature termination of translation can lead to lower efficiency expression of large molecular weight proteins in cell-free expression systems. In addition to its manageable size, the dockerin exhibits a specific and high affinity interaction with a cohesin domain from the *C. thermocellum* scaffold protein CipA, which was used both for fluorescence detection of the expression constructs and for modification of the cantilever. Based on our prior work, we knew the cohesin-dockerin interaction to be high affinity, with a K_d in the picomolar range and a rupture force >125 pN at a loading rate of 10 nN/s(*26*). Our prior work also indicated that upon forced dissociation, the dockerin exhibited a characteristic double sawtooth rupture peak with a contour length increment of 8 nm separating the two peaks. We used this two-pronged double rupture event at the end of each force-extension trace as an internal control, a positive indicator that the gene of interest was completely expressed through to the C-terminus. Furthermore this double rupture peak indicated that the interaction with the cohesin-modified cantilever was specific, and that the pulling geometry was strictly controlled such that force was applied to the molecule of interest from the N to C-terminus.

As a demonstration of our SMFS-MITOMI approach, we chose to express genes of interest comprising well-known fingerprint domains in the SMFS literature. We produced multimeric polyproteins including tetrameric human type-III fibronectin (*27*) and dimeric chicken brain alpha spectrin (*28*). We also produced monomers of endo-1, 4-xylanase T6 from *G. stearothermophilus* (*26*), superfolder green fluorescent protein(*29*), and twitchin kinase(*30*). In all cases, surface immobilization and single molecule force assay were enabled by N-terminal ybbR and C-terminal dockerin tags on the target proteins. Unfolding data for fibronectin, spectrin, and xylanase obtained with a single cantilever are shown in Figures 2 and 3, with GFP characterization shown in Supporting Figure S2. Twitchin kinase was found not to express in sufficient yield to provide reliable unfolding statistics.

Single molecule unfolding traces for three of our selected fingerprint domains are shown in **Figure 2**. We transformed the force-extension data into contour length space (*31*) using a worm-like chain model for polymer elasticity. We could then compare the contour length increments observed upon unfolding monomer or multimer target proteins at each spot in the array from the N- to the C-terminus with our expectation based on the number of amino acids and the length of the folded domains. In all cases, the observed contour length increments and rupture forces were consistent with the contour length estimations. The fibronectin tetramer (**Fig. 2A**), for example, showed a four-fold sequence of rupture peaks at contour length increments of 31 nm, sometimes interrupted by an intermediate peak at 10-12 nm, both characteristics typical of fibronectin type III. The spectrin homodimer fusion protein (**Fig. 2B**) showed two regular sawtooth-like peaks with contour lengths of 34 nm, as well as the characteristic cohesin-dockerin double peak at the end of the trace. The monomer endo-1, 4-beta-xylanase (**Fig. 2C**), exhibited a decreasing three pronged unfolding fingerprint, with a total contour length of 93 nm, followed by the final double rupture peak of the cohesin-dockerin complex, an unfolding pattern that was consistent with our prior study(*26*). Thus, at known locations in the array, we could record unfolding traces of individual custom encoded proteins, stretching them from the surface with a cohesin-modified cantilever by grabbing the high-affinity and mechanically stable C-terminal dockerin tags. Since each protein in the array contained the same C-terminal dockerin tag, the final rupture peaks in each force trace represented rupture of the cohesin-dockerin complex.

For AFM based SMFS, the surface density of proteins should be high enough to collect sufficient spectra, but at the same time low enough to avoid the formation of multiple bonds. In our system, surface densities of expressed proteins were comparable to existing SMFS experiments, such that in a single spot we had a yield of interpretable curves of up to 5 %. The assembled statistics for three proteins of interest are shown in **Figure 3**. We assembled contour length histograms for each protein of interest (**Fig 3A-C**) (*31*-*33*), and confirmed the predicted contour length increments based on the encoded amino acid sequences in each cDNA spot. Typically in SMFS experiments, rupture force – loading rate plots are used to characterize k_{off} and Δx, the unbinding (or unfolding) probability and the distance to the transition state along the reaction coordinate, respectively, providing direct information about the energy landscape governing protein folding (*34*). The information gleaned from SMFS experiments are also complemented by all-atom simulations of such systems *in silico*. Recently, it was shown that high speed SMFS experiments could be performed at speeds achievable in molecular dynamics simulations(*35*), overcoming a long standing discrepancy between experiment and simulation. Shown in Figure 3D are the rupture statistics of the cohesin-dockerin handle for each protein in the array. The rupture force distributions **(Fig. 3D)** of cohesin-dockerin unbinding events were independent of the preceding rupture peaks from the protein of interest. As shown in **Figure 3E**, the unfolding statistics for the proteins of interest provided independent distributions in the force – loading rate plots. Spectrin, for example, an elongated 3-helix bundle showed a broader energy well (i.e., larger Δx) compared with the more compact globular fibronectin and xylanase domains.

The system we described for *in vitro* expression and covalent immobilization inside a microfluidic device is highly flexible and efficiently streamlines protein expression, purification, and single molecule force assay into a single integrated platform. We have demonstrated the system with an *E. coli* cell free expression system, but the approach is generally viable with other systems including extracts derived from insects, rabbit reticulocytes, and human cell lines. *In vitro* expression is also generally capable of introducing post-translational modifications and non-natural amino acids, further widening the pool of target proteins, for example screening of site-directed mutants for mechanical properties. Using the fluorescent rings for orientation, computerized image analysis can also be used to automate cantilever positioning and acquisition of unfolding traces for each construct in the array. In addition to greatly improved throughput, our system has the advantage of measuring multiple constructs with one cantilever. Contrary to previous calibration procedures with uncertainties up to ±10%(*36*), our system interrogates an entire protein array with a single cantilever, eliminating errors introduced by performing multiple calibrations on different samples. Detecting subtle differences in mechanical stability between similarly stable mutants with this approach could therefore be enabled. Additionally, well-characterized reference proteins on the same chip may serve as calibration standards further minimizing uncertainty. This workflow opens the door to large-scale screening studies of protein nanomechanical properties, a possibility that was until now not achievable.

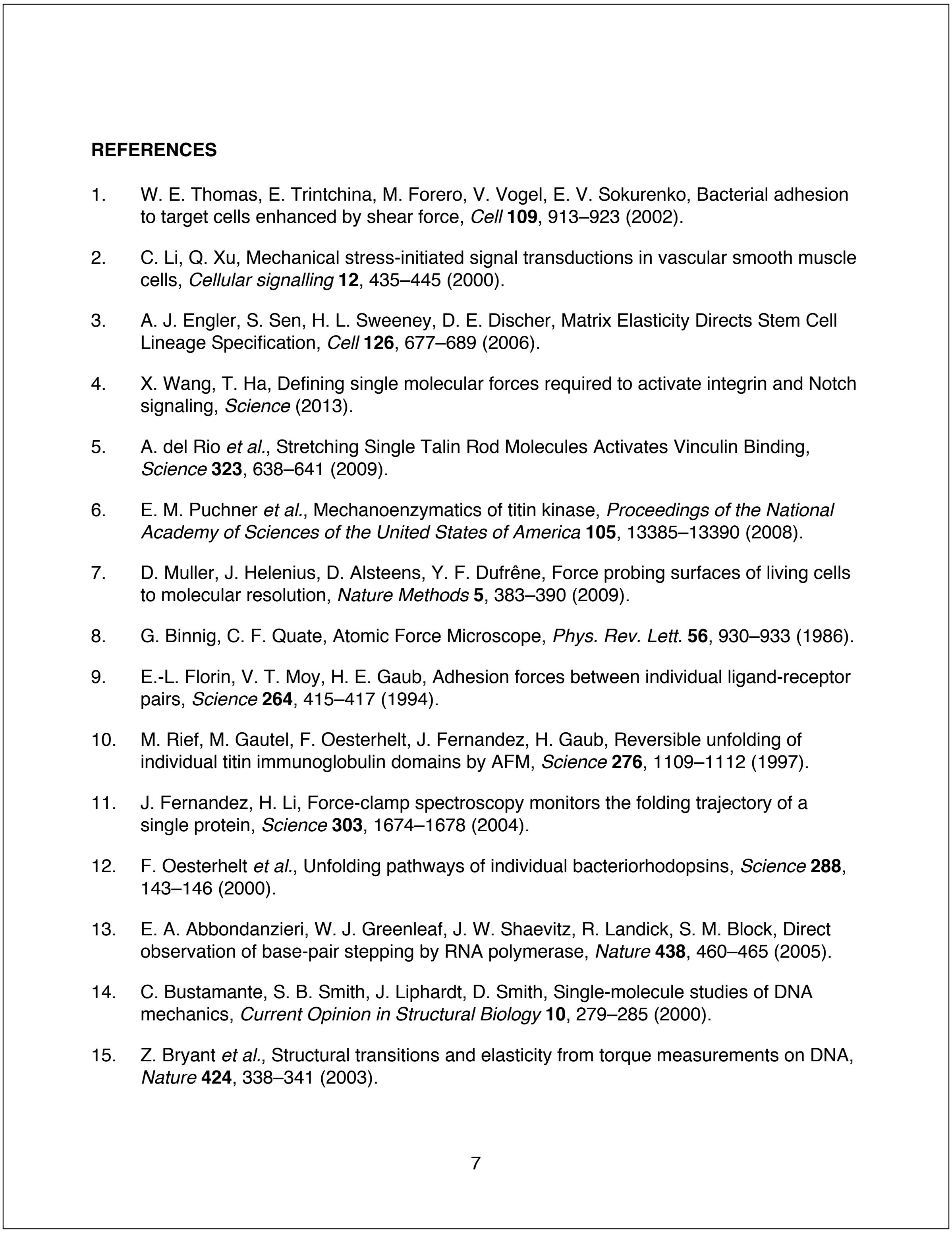

REFERENCES

1. W. E. Thomas, E. Trintchina, M. Forero, V. Vogel, E. V. Sokurenko, Bacterial adhesion to target cells enhanced by shear force, *Cell* **109**, 913–923 (2002).

2. C. Li, Q. Xu, Mechanical stress-initiated signal transductions in vascular smooth muscle cells, *Cellular signalling* **12**, 435–445 (2000).

3. A. J. Engler, S. Sen, H. L. Sweeney, D. E. Discher, Matrix Elasticity Directs Stem Cell Lineage Specification, *Cell* **126**, 677–689 (2006).

4. X. Wang, T. Ha, Defining single molecular forces required to activate integrin and Notch signaling, *Science* (2013).

5. A. del Rio *et al.*, Stretching Single Talin Rod Molecules Activates Vinculin Binding, *Science* **323**, 638–641 (2009).

6. E. M. Puchner *et al.*, Mechanoenzymatics of titin kinase, *Proceedings of the National Academy of Sciences of the United States of America* **105**, 13385–13390 (2008).

7. D. Muller, J. Helenius, D. Alsteens, Y. F. Dufrêne, Force probing surfaces of living cells to molecular resolution, *Nature Methods* **5**, 383–390 (2009).

8. G. Binnig, C. F. Quate, Atomic Force Microscope, *Phys. Rev. Lett.* **56**, 930–933 (1986).

9. E.-L. Florin, V. T. Moy, H. E. Gaub, Adhesion forces between individual ligand-receptor pairs, *Science* **264**, 415–417 (1994).

10. M. Rief, M. Gautel, F. Oesterhelt, J. Fernandez, H. Gaub, Reversible unfolding of individual titin immunoglobulin domains by AFM, *Science* **276**, 1109–1112 (1997).

11. J. Fernandez, H. Li, Force-clamp spectroscopy monitors the folding trajectory of a single protein, *Science* **303**, 1674–1678 (2004).

12. F. Oesterhelt *et al.*, Unfolding pathways of individual bacteriorhodopsins, *Science* **288**, 143–146 (2000).

13. E. A. Abbondanzieri, W. J. Greenleaf, J. W. Shaevitz, R. Landick, S. M. Block, Direct observation of base-pair stepping by RNA polymerase, *Nature* **438**, 460–465 (2005).

14. C. Bustamante, S. B. Smith, J. Liphardt, D. Smith, Single-molecule studies of DNA mechanics, *Current Opinion in Structural Biology* **10**, 279–285 (2000).

15. Z. Bryant *et al.*, Structural transitions and elasticity from torque measurements on DNA, *Nature* **424**, 338–341 (2003).

16. W. A. Linke, Sense and stretchability: The role of titin and titin-associated proteins in myocardial stress-sensing and mechanical dysfunction†, *Cardiovascular Research* **77**, 637–648 (2008).

17. J. Yin *et al.*, Genetically encoded short peptide tag for versatile protein labeling by Sfp phosphopantetheinyl transferase, *Proceedings of the National Academy of Sciences of the United States of America* **102**, 15815–15820 (2005).

18. S. J. Maerkl, S. R. Quake, A Systems Approach to Measuring the Binding Energy Landscapes of Transcription Factors, *Science* **315**, 233–237 (2007).

19. D. Gerber, S. J. Maerkl, S. R. Quake, An in vitro microfluidic approach to generating protein-interaction networks, *Nature Methods* **6**, 71–74 (2008).

20. M. Otten, P. Wolf, H. E. Gaub, Protein–DNA force assay in a microfluidic format, *Lab on a Chip* **13**, 4198 (2013).

21. D. C. Duffy, J. C. McDonald, O. J. A. Schueller, G. M. Whitesides, Rapid Prototyping of Microfluidic Systems in Poly(dimethylsiloxane), *Anal. Chem.* **70**, 4974–4984 (1998).

22. T. Thorsen, S. J. Maerkl, S. R. Quake, Microfluidic large-scale integration, *Science* **298**, 580–584 (2002).

23. J. L. Garcia-Cordero, S. J. Maerkl, Multiplexed surface micropatterning of proteins with a pressure-modulated microfluidic button-membrane, *Chemical Communications* **49**, 1264 (2013).

24. H. Gumpp, S. W. Stahl, M. Strackharn, E. M. Puchner, H. E. Gaub, Ultrastable combined atomic force and total internal fluorescence microscope, *Review of Scientific Instruments* **80**, 063704 (2009).

25. E. A. Bayer, J.-P. Belaich, Y. Shoham, R. Lamed, THE CELLULOSOMES: Multienzyme Machines for Degradation of Plant Cell Wall Polysaccharides, *Annual Review of Microbiology* **58**, 521–554 (2004).

26. S. W. Stahl *et al.*, Single-molecule dissection of the high-affinity cohesin–dockerin complex, *Proceedings of the National Academy of Sciences of the United States of America* **109**, 20431–20436 (2012).

27. L. Li, H. H.-L. Huang, C. L. Badilla, J. M. Fernandez, Mechanical Unfolding Intermediates Observed by Single-molecule Force Spectroscopy in a Fibronectin Type III Module, *Journal of Molecular Biology* **345**, 817–826 (2005).

28. M. Rief, J. Pascual, M. Saraste, H. E. Gaub, Single molecule force spectroscopy of spectrin repeats: low unfolding forces in helix bundles, *Journal of Molecular Biology* **286**, 553–561 (1999).

29. H. Dietz, M. Rief, Protein structure by mechanical triangulation, *Proceedings of the National Academy of Sciences of the United States of America* **103**, 1244–1247 (2006).

30. D. N. Greene *et al.*, Single-Molecule Force Spectroscopy Reveals a Stepwise Unfolding of Caenorhabditis elegans Giant Protein Kinase Domains, *Biophysical Journal* **95**, 1360–1370 (2008).

31. E. M. Puchner, G. Franzen, M. Gautel, H. E. Gaub, Comparing Proteins by Their Unfolding Pattern, *Biophysical Journal* **95**, 426–434 (2008).

32. M. A. Jobst, C. Schoeler, K. Malinowska, M. A. Nash, Investigating Receptor-ligand Systems of the Cellulosome with AFM-based Single-molecule Force Spectroscopy, *Journal of Visualized Experiments (JoVE)* (2013), doi:10.3791/50950.

33. P. D. Bosshart *et al.*, High-throughput single-molecule force spectroscopy for membrane proteins, *Nanotechnology* **19**, 384014 (2008).

34. R. Merkel, P. Nassoy, A. Leung, K. Ritchie, E. Evans, Energy landscapes of receptor–ligand bonds explored with dynamic force spectroscopy, *Nature* **397**, 50–53 (1999).

35. F. Rico, L. Gonzalez, I. Casuso, M. Puig-Vidal, S. Scheuring, High-Speed Force Spectroscopy Unfolds Titin at the Velocity of Molecular Dynamics Simulations, *Science* **342**, 741–743 (2013).

36. C. T. Gibson, D. A. Smith, C. J. Roberts, Calibration of silicon atomic force microscope cantilevers, *Nanotechnology* **16**, 234–238 (2005).

Acknowledgements: M.O. is grateful to the Elite Network of Bavaria (IDK-NBT) for a doctoral fellowship. M.A.N. gratefully acknowledges support from Society in Science – The Branco Weiss Fellowship administered by the ETH Zürich. The authors acknowledge support from the European Research Council.

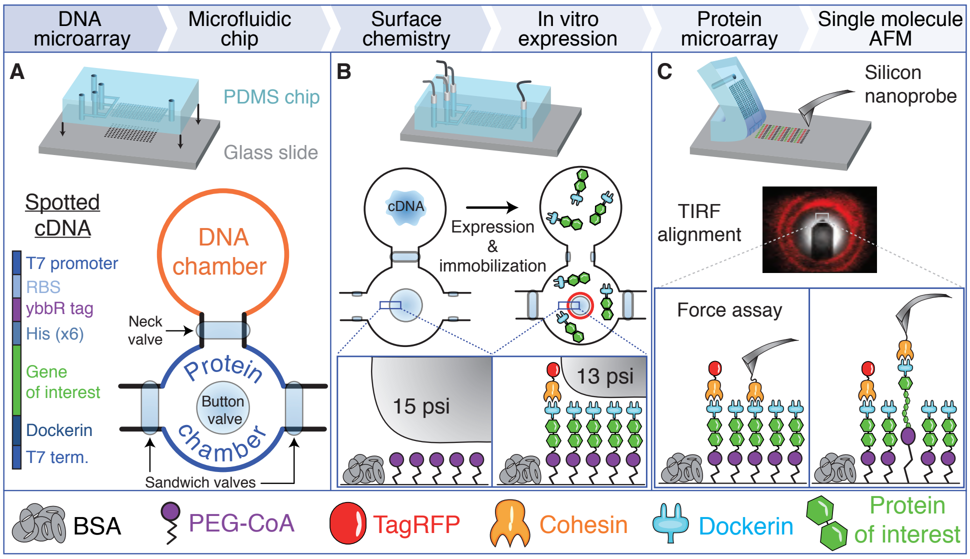

Figure 1: Method workflow from gene array to single-molecule mechanics.
(A) A gene array was spotted onto a glass slide. Genes were designed with a common set of flanking sequences, including a T7 promoter region, a ybbR tag, a dockerin tag and a T7 terminator. The multilayer microfluidic chip featuring 640 unit cells was aligned to the DNA microarray and bonded to the glass slide. Each unit cell comprised a DNA chamber, a protein chamber, and superseding elastomeric control valves, actuated by pneumatic pressure.
(B) Control valves were utilized for spatially selective surface modification of each protein chamber with PEG-CoA, and for fluidic isolation of each chamber prior to *in vitro* expression of the microspotted cDNA. Fluorescent labelling with TagRFP-cohesin was achieved by partial button valve pressurization, leaving only an outer concentric ring of immobilized gene products exposed to the labelling solution.
(C) After removal of the microfluidic device, the resulting well-defined, covalently attached protein microarray was accessed from above with a cohesin-functionalized AFM cantilever. Single-molecule unfolding traces of each of the investigated proteins were thus acquired sequentially at each array address with a single cantilever in a single experiment.

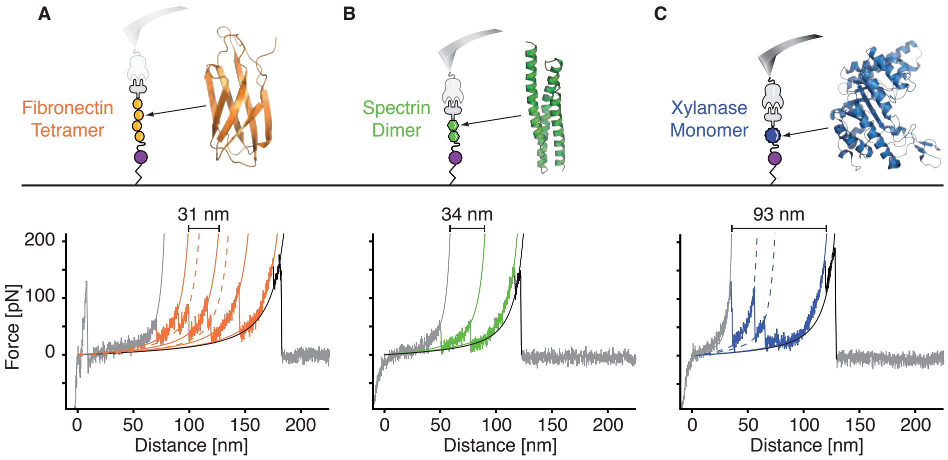

Figure 2: Single-molecule force traces recorded in three protein spots on a single chip with a single cantilever.
Three proteins of interest, anchored between the CoA-functionalized surface and the cohesin-functionalized cantilever were probed: fibronectin tetramer (A, orange), spectrin dimer (B, green), and xylanase monomer (C, blue). The crystal structure and pulling configuration (top) are shown for each construct. Each single-molecule force-distance trace (bottom) showed unfolding of the protein of interest followed by a common, final double sawtooth peak (black), characteristic of the cohesin-dockerin rupture. Experimental data were fitted with the worm-like chain model (solid lines). Unfolding intermediates for fibronectin and xylanase were also observed (dotted lines).

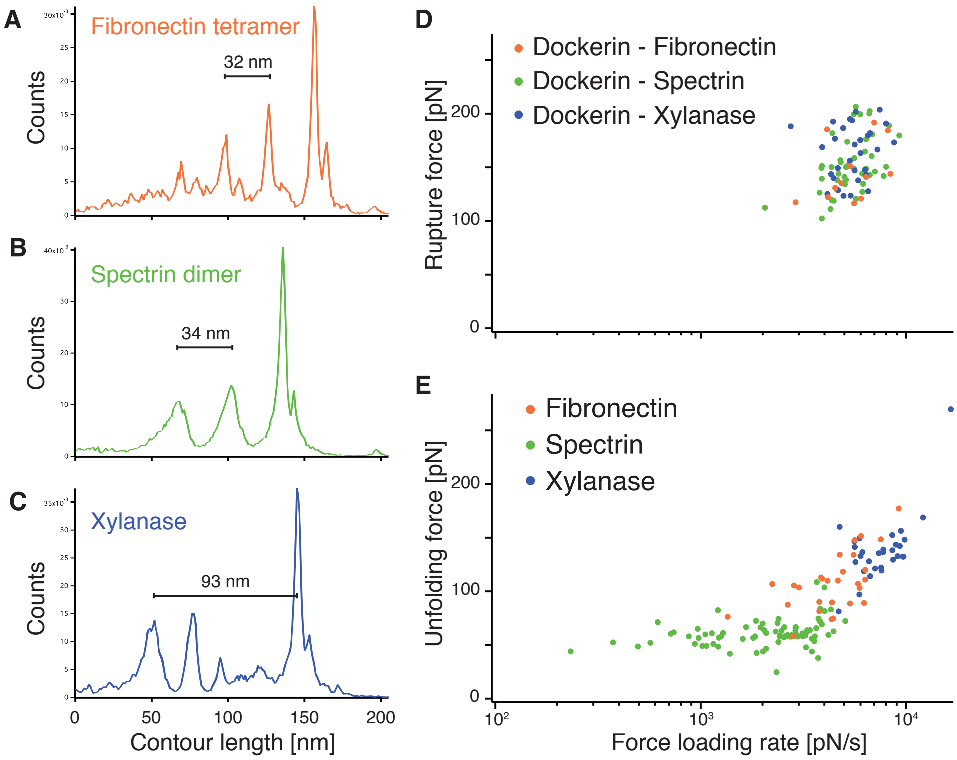

Figure 3: Unfolding and rupture statistics from multiple force traces.
Panels (A)-(C) show contour length histograms assembled by transforming and aligning multiple force traces into contour length space *via* the WLC model. Shown are histograms for the fibronectin tetramer (A) (n=12, L_c=32 nm), spectrin dimer (B) (n=48, L_c=34 nm) and xylanase monomer (C) (n=30, L_c=93nm). (D) Rupture force *vs.* loading rate scatter plot of final cohesin-dockerin dissociation event. (E) Unfolding force *vs.* loading rate scatter plot for each protein of interest.

4 A microfluidic chip to probe protein–DNA interaction forces

The established Molecular Force Assay (MFA) method has proven extremely powerful in quantifying various types of intermolecular bonds [61]. In particular, the interaction between DNA and proteins, *e.g.* transcription factors, is of great interest [33]. However, current efforts to study these interactions rely on a growing set of data gathered by high–throughput means [40]. Therefore, the need for an integrated high–throughput version of the MFA is manifest.

In this chapter and in publication P1, the development of an integrated microfluidic MFA method to probe protein–DNA interactions is presented. It relies on the MITOMI [79] chip layout with its button valve and confocal fluorescence readout.

4.1 Summary of associated publication P1

In the associated publication P1, the molecular force assay method is for the first time transferred into a microfluidic chip format. This entails a few changes to the protocol and advantages in experiment and analysis workflow:

- The macroscopic piezo actuator is replaced by a pneumatic pressure valve as force–loading element.
- An alternative single–run confocal fluorescence readout method is used, rather than the previously used before–after series of fluorescent images.
- High–throughput by miniaturization and parallelization is accessible due to the microfluidic format.

The publication P1 describes the characterization, validation and application of this new on–chip–MFA method. In particular, the geometry and dynamics of the button valve membrane are characterized using reflection interference contrast microscopy. The experimentally determined approach and retraction velocities of 0.23 $\mu m \cdot s^{-1}$ and 0.26 $\mu m \cdot s^{-1}$ are in accordance with low velocities of previous MFA experiments. The validation of the method is carried out with a symmetric DNA probe, which typically exhibits equal rupture probabilities at both duplexes. The median normalized fluorescence indeed proves to be close to 0.5. To apply the method in a multiplexing experiment and to demonstrate its high–throughput capabilities, the chip is loaded with different combinations of EcoRI binding sequences (*consensus* and *star*) and reference oligomer lengths (from 25 to 40 bp). The resulting set of data, shown in Figure 4 of the associated publication P1, is consistent with simulations based on the Bell–Evans model and permits the quantification of the mechanical stabilizing effect of EcoRI binding to its consensus sequence.

In summary, the results detailed in associated publication P1 herald quantitative studies of protein–DNA interactions in a microfluidic chip format based on the established MFA method beyond this proof–of–principle. EcoRI can be replaced by one or more other proteins of interest. In particular, the *in vitro* expression capabilities of the chip, as demonstrated in manuscript M1, can potentially be harnessed for a MFA experiment. Thus, the proteins of interest can be expressed in the back chamber of the chip from microspotted cDNA before binding to probe strands in the button area.

4.2 Associated publication P1

Protein–DNA force assay in a microfluidic format

by
Marcus Otten, Philip Wolf and Hermann E. Gaub

published in
Lab on a Chip, **13**, 4198-4204 (2013)

Lab on a Chip RSCPublishing

PAPER

Protein–DNA force assay in a microfluidic format†

Marcus Otten, Philip Wolf and Hermann E. Gaub

Cite this: *Lab Chip*, 2013, **13**, 4198

Received 12th July 2013,
Accepted 2nd August 2013

DOI: 10.1039/c3lc50830g

www.rsc.org/loc

The detailed study of protein–DNA interactions is a core effort to elucidate physiological processes, including gene regulation, DNA repair and the immune response. The molecular force assay (MFA) is an established method to study DNA-binding proteins. In particular, high-affinity binder dissociation is made possible by the application of force. Microfluidic lab-on-a-chip approaches have proven helpful for parallelization, small sample volumes, reproducibility, and low cost. We report the successful combination of these two principles, forming a microfluidic molecular force assay and representing a novel use for the established MITOMI chip design. We present, characterize, validate and apply this integrated method. An alternative confocal fluorescence microscopy readout and analysis method is introduced and validated. In a multiplexing application, EcoRI binding is detected and characterized. This method paves the way for quantitative on-chip force measurements. It is suited for integration with DNA micro-spotting and *in vitro* expression of transcription factors to form a high-throughput chip for detailed DNA–protein interaction studies.

Introduction

DNA–protein studies

Interactions between proteins and DNA are ubiquitous in living systems. Most prominently, DNA-binding transcription factors regulate gene expression.[1] Furthermore, proteins are involved in DNA repair[2,3] and the immune response.[4] In each of these tasks, the binding process and forces involved are crucial for function and can only be understood by combining a range of measurements, including affinity,[5] specificity,[6,7] turnover[8] and binding force.[9] As a most prominent example, transcription factor binding and turnover dynamics are a better predictor for functional regulation than mere occupancy levels.[10] A variety of methods for measuring DNA–protein interactions have been proposed, which differ most notably in measurement environment (*in vivo versus in vitro*), in washing requirements, in labeling needs, and in multiplexing capabilities. Chromatin-immunoprecipitation (ChIP)-based methods[11] have proven very valuable for *in vivo* measurements, despite the need for specialized antibodies for precipitation. Protein-binding microarrays (PBM)[12,13] are well suited to detect high affinity binding sequences for a given protein, if available in high amounts. Yeast-one-hybrid (Y1H)[14,15] and bacterial one-hybrid (B1H)[16] approaches are typically used to determine the proteins that bind to a given DNA sequence and are thus complementary to ChIP and PBM. High-throughput versions have been proposed.[17] These methods have a common set of drawbacks, including the need for labeling antibodies, low sensitivity or resolution and lack of parallel screening of multiple DNA sequences against multiple proteins and multiple references. This highlights the need for integrated methods, which will help overcome these drawbacks.

The molecular force assay

The molecular force assay (MFA) is an established method to probe intermolecular bonds, *e.g.* DNA–protein interactions. A probe bond and a known reference are assembled in series on a surface, bond-breaking forces are applied *via* surface retraction and a fluorescence readout reveals the bond rupture site. This approach has numerous advantages, including high sensitivity, statistical significance, its ability to detect both weak and strong binders and its independence of binder labels. Its sensitivity is due to the use of single molecules as the reference force sensor. Statistics are readily assembled in a single run, because many bonds are probed in parallel on a surface. By tuning the reference bond *via* its length, one can adapt to binders of varying strength. The active force load upon surface retraction speeds up unbinding of strong binders, up to dissociation constants in the pM range. The force probe DNA oligomers are labeled and used for the fluorescent readout, but these fluorophores are not directly at the probe or binding sites. The binder is not labeled. MFA has been used for a variety of applications and alterations of the DNA, including mismatches,[18] methylation[19] or hydroxymethylation[20] have been shown to be detectable. Its measurement principle has been applied to the binding of transcription factors, nucleases and polyamides[21] and RNA–protein interactions.[22]

Lehrstuhl für Angewandte Physik and Center for Nanoscience (CeNS), Ludwig-Maximilians-Universität, Amalienstrasse 54, 80799 Munich, Germany

† Electronic supplementary information (ESI) available. See DOI: 10.1039/c3lc50830g

Microfluidics and MITOMI

The advent of microfluidics and lab-on-a-chip technologies has recently spurred miniaturization and parallelization of tried-and-tested methods. Advantages include smaller sample volumes, higher throughput, facilitated reproducibility and reduced experimental time. One particular variant of microfluidics involves the use of multi-layer soft lithography, as pioneered by Quake *et al.*[23] One layer, the flow layer, can be used for biochemical reactions, whereas another is used to control these flows by application of pneumatic pressure. With respect to the study of protein–DNA interactions, Maerkl and Quake applied these design principles to obtain what is now known as the MITOMI chip, acronym for mechanically induced trapping of molecular interactions.[24] A button valve is used to seal and protect the sample area from contamination by neighbors or from stringent washing.[25] The chip has been applied to measure a variety of other interactions, including protein–protein[26] and protein–RNA.[27] In some cases, reaction chambers have been used for *in vitro* expression of the proteins to be probed.[26] Recently, the chip design has been improved for fast response times and the chip is now capable of recording association and dissociation traces.[28]

In the present publication, we introduce a novel method, which for the first time combines the MFA measurement principle with a microfluidic design. In particular, the button valve of the MITOMI chip is used to apply the force necessary for bond rupture. We characterize the setup, validate it by comparison to non-microfluidic measurements, introduce a novel readout and analysis route and apply it to detect a model binder, the endonuclease EcoRI, which shows no nuclease activity in the absence of its cofactor Mg^{2+}.

Results & discussion

Method summary

The microfluidic chip design is identical to the 640-chamber MITOMI chip introduced by Maerkl and Quake.[24] The chips are produced by two-layer soft lithography of polydimethylsiloxane (PDMS). The inner walls of the flow layer display covalently attached DNA duplexes after a series of treatments

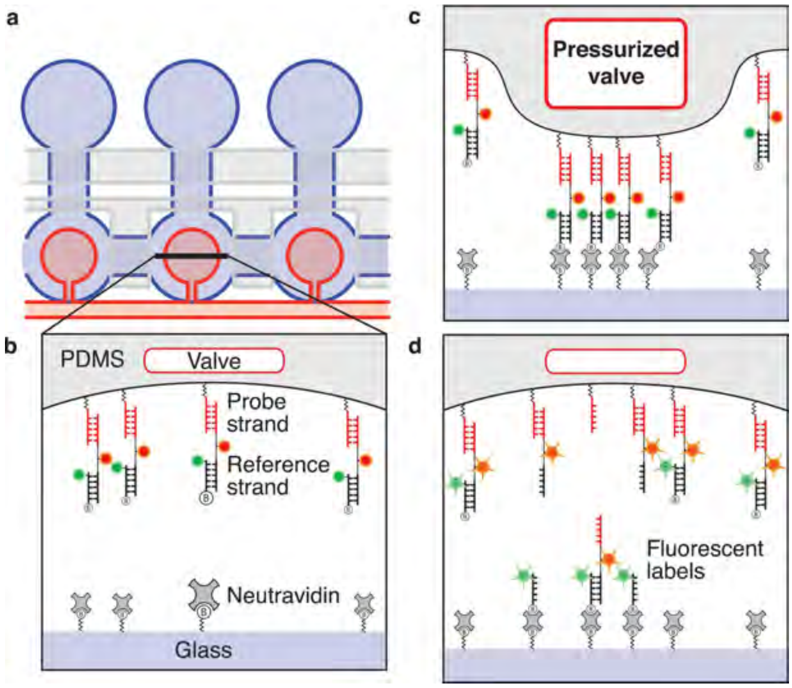

Fig. 1 Experimental design. (a) shows three of 640 double chambers in the flow layer (blue) and the overlying control layer valves (red and grey), which can expand into the flow layer by pneumatic pressure. (b) shows the initial distribution of PEG–biotin–neutravidin complexes at the glass surface and PEG–DNA probe–fluorophore–biotin complexes along the flow layer PDMS wall. (c) Actuation of the button valve establishes contact between the glass and PDMS surfaces within the button valve region only. (d) After pressure release and button retraction, the fluorophore distribution is recorded on a confocal fluorescence readout. Transferred Cy3 fluorophores (green) denote the coupling efficiency, whereas transferred Cy5 (red) is a measure of the force probes broken at the top DNA duplex bond.

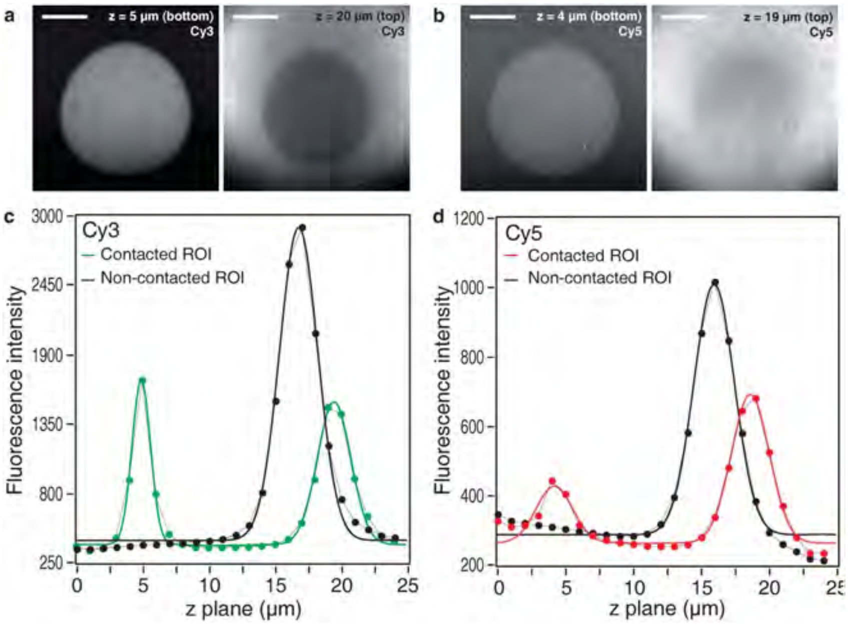

Fig. 2 Single-chamber data readout. (a) and (b) show fluorescence images of the Cy3 and Cy5 channels, respectively. The bottom glass surface slices and top PDMS surface slices are shown after button retraction. The bottom slices show transferred fluorophores and DNA strands, which are missing from the top surfaces. Scale bar: 25 µm. (c) and (d) show the vertical intensity profiles of the Cy3 and Cy5 channels, respectively. The mean intensity of the two regions of interest (ROI) is computed and plotted (dots) against the *z* slice position and fitted with Gaussian functions (lines). The contacted ROI (under the button valve) data is shown in color (green or red), the non-contacted ROI (to the side of the chamber) is shown in black. The Gaussian fit data serve for all follow-up analysis. The vertical shifts between the contacted and non-contacted ROI data are due to the PDMS chamber curvature.

with hydrochloric acid, aminosilane, NHS–polyethylene glycol–maleimide, and thiolized DNA oligomers[29,30] (Supplemental Fig. 1, ESI†). After bonding the functionalized chip to a neutravidin-coated glass slide, the button valve of the PDMS control layer is actuated by a linear pressure increase. Upon button retraction, one of the bonds will give, according to their relative rupture probabilities. The relative fluorophore distributions (top *vs.* bottom surfaces, or contacted *vs.* non-contacted regions) are determined by confocal fluorescent microscopy and analyzed to determine the relative rupture probabilities of the DNA duplex bonds (Fig. 1). The Cy3 transfer is proportional to the coupling efficiency of the biotin–neutravidin bond, whereas the location of the Cy5 signal reveals the stronger bond. For a more detailed description of the experimental workflow, we refer to the ESI†.

MFA principle & characterization

Fig. 1 shows the experimental design and measurement principle of the MFA. Each of the 640 chambers of the MITOMI chip displays two DNA duplexes in series at the top PDMS surface. The known bond will serve as a reference whereas the other one is the probe. By actuation of the button valve, a circular region is brought into contact with the glass surface underneath and coupling occurs *via* biotin–neutravidin interactions. Upon pressure release and button retraction, both duplexes are probed under force and one of them ruptures, with probabilities related to their relative strengths.[31] The fluorophores attached to strands 2 and 3 allow for their localization by confocal fluorescence imaging.

We characterize the button valve actuation by reflection interference contrast microscopy. The spatial succession of the interference maxima and minima reveals the shape of the PDMS button just prior to glass contact. We find the surface to be parabola-shaped with high reproducibility. The temporal succession of the interference maxima and minima reveals the approach and retraction velocities of this surface perpendicular to the glass surface. The approach and retraction speed can be controlled by variation of the pressure slope. In the present publication, this slope was chosen to be 0.1 psi s^{-1}, ensuring an equal valve actuation across all chambers and chips. We find good agreement between the approach velocity of 0.23 µm s^{-1}, and the retraction velocity of 0.26 µm s^{-1}, independent of the radial distance from the parabola tip (Supplemental Fig. 2, ESI†). These values are compatible with the low speeds of the piezoelectric actuator used in previous MFA implementations between 0.2 and 20 µm s^{-1}.

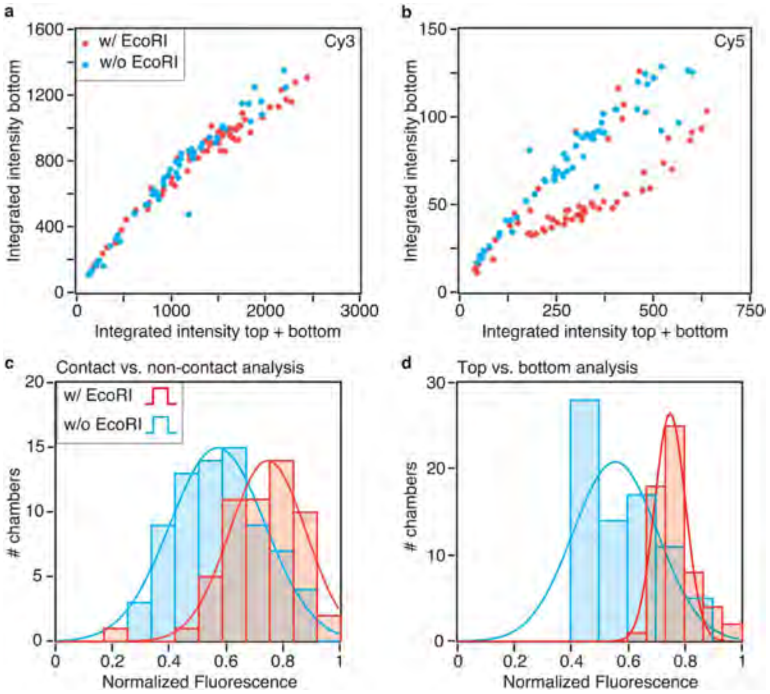

Fig. 3 Chip analysis. (a) and (b) show scatter plots of Cy3 and Cy5 intensity data from hundreds of chambers, respectively. For each chamber the integrated bottom signal is plotted against the sum of its integrated bottom and top signals in the contacted ROI only. (c) and (d) show histograms of the normalized fluorescence (corresponding to the relative bond rupture probability) computed using the contact-*vs.*-non-contact and top-*vs.*-bottom analysis methods, respectively. The histograms are fitted with Gaussian distributions. The histograms and fits are shown with and without the presence of EcoRI binders (red and blue, respectively).

Multiple key differences to previous MFA implementations emerge. First, the force application occurs by pneumatic means, rather than by a voltage-controlled piezo element. No bulk PDMS can dampen the retraction movement, which allows more direct control of the retraction speed. Second, the contact and separation occurs between a flat glass surface and a rounded PDMS surface, as opposed to two planar surfaces. This is predicted to be a more favorable geometry to avoid non-linear retraction effects. Soft lithography and photoresist reflow are versatile tools to tune the actuation of this membrane.[32] Third, the small distance separating the two fluorescent surfaces facilitates comparable readouts of both surfaces. Previously, only the glass surface was analyzed. This additional set of data opens up a top-*vs.*-bottom analysis route, rather than the traditional contact-*vs.*-non-contact method.

Comparison of analysis methods

The data readout and analysis for a single chamber are shown in Fig. 2. Confocal scans are performed identically for two fluorescent channels, Cy3 and Cy5. The Cy5 signal is a measure of the number of transferred middle strands, whereas the Cy3 signal is a measure of the coupling efficiency of the probe *via* biotin–neutravidin bonding to the glass surface. The contacted region of interest (ROI) beneath the button valve shows fluorescence signals both at the glass surface and at the PDMS surface, whereas the non-contacted ROI shows no fluorescence transfer from the PDMS onto the glass surface, as can be seen in Fig. 2c and 2d. Both distributions can be fitted with Gaussian functions. This data collection opens up two alternative analysis routes: (1) a contact-*vs.*-non-contact method similar to the previously introduced MFA analysis, and (2) a top-*vs.*-bottom method. The first compares the two regions at the PDMS surface to determine the missing dye fraction at the contacted ROI, whereas the second method compares the two peaks of the contacted ROI to determine the transferred dye fraction.

The quantity of interest is the relative rupture probability of the two bonds. On the basis of previous MFA studies, it is named ''normalized fluorescence'' (NF) and denotes the fraction of probes ruptured at the lower bond, normalized to the number of probes coupled and under load. It is thus equivalent to the relative rupture probability of the two bonds. It can be expressed as follows for the contact-*vs.*-non-contact

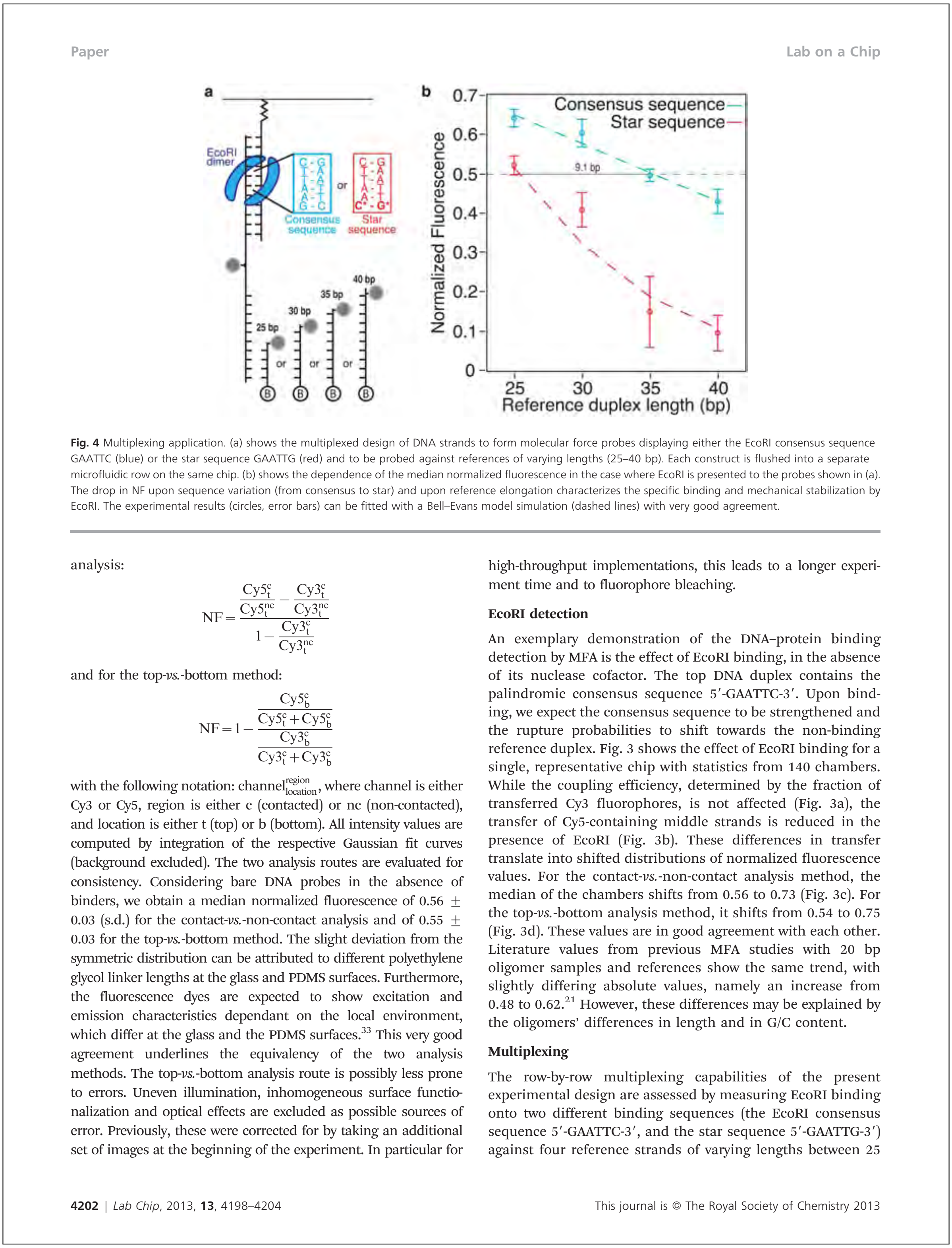

Fig. 4 Multiplexing application. (a) shows the multiplexed design of DNA strands to form molecular force probes displaying either the EcoRI consensus sequence GAATTC (blue) or the star sequence GAATTG (red) and to be probed against references of varying lengths (25–40 bp). Each construct is flushed into a separate microfluidic row on the same chip. (b) shows the dependence of the median normalized fluorescence in the case where EcoRI is presented to the probes shown in (a). The drop in NF upon sequence variation (from consensus to star) and upon reference elongation characterizes the specific binding and mechanical stabilization by EcoRI. The experimental results (circles, error bars) can be fitted with a Bell–Evans model simulation (dashed lines) with very good agreement.

analysis:

$$\mathrm{NF} = \frac{\dfrac{\mathrm{Cy5}^{\mathrm{c}}_{\mathrm{t}}}{\mathrm{Cy5}^{\mathrm{nc}}_{\mathrm{t}}} - \dfrac{\mathrm{Cy3}^{\mathrm{c}}_{\mathrm{t}}}{\mathrm{Cy3}^{\mathrm{nc}}_{\mathrm{t}}}}{1 - \dfrac{\mathrm{Cy3}^{\mathrm{c}}_{\mathrm{t}}}{\mathrm{Cy3}^{\mathrm{nc}}_{\mathrm{t}}}}$$

and for the top-*vs.*-bottom method:

$$\mathrm{NF} = 1 - \frac{\dfrac{\mathrm{Cy5}^{\mathrm{c}}_{\mathrm{b}}}{\mathrm{Cy5}^{\mathrm{c}}_{\mathrm{t}} + \mathrm{Cy5}^{\mathrm{c}}_{\mathrm{b}}}}{\dfrac{\mathrm{Cy3}^{\mathrm{c}}_{\mathrm{b}}}{\mathrm{Cy3}^{\mathrm{c}}_{\mathrm{t}} + \mathrm{Cy3}^{\mathrm{c}}_{\mathrm{b}}}}$$

with the following notation: $\mathrm{channel}^{\mathrm{region}}_{\mathrm{location}}$, where channel is either Cy3 or Cy5, region is either c (contacted) or nc (non-contacted), and location is either t (top) or b (bottom). All intensity values are computed by integration of the respective Gaussian fit curves (background excluded). The two analysis routes are evaluated for consistency. Considering bare DNA probes in the absence of binders, we obtain a median normalized fluorescence of 0.56 ± 0.03 (s.d.) for the contact-*vs.*-non-contact analysis and of 0.55 ± 0.03 for the top-*vs.*-bottom method. The slight deviation from the symmetric distribution can be attributed to different polyethylene glycol linker lengths at the glass and PDMS surfaces. Furthermore, the fluorescence dyes are expected to show excitation and emission characteristics dependant on the local environment, which differ at the glass and the PDMS surfaces.[33] This very good agreement underlines the equivalency of the two analysis methods. The top-*vs.*-bottom analysis route is possibly less prone to errors. Uneven illumination, inhomogeneous surface functionalization and optical effects are excluded as possible sources of error. Previously, these were corrected for by taking an additional set of images at the beginning of the experiment. In particular for high-throughput implementations, this leads to a longer experiment time and to fluorophore bleaching.

EcoRI detection

An exemplary demonstration of the DNA–protein binding detection by MFA is the effect of EcoRI binding, in the absence of its nuclease cofactor. The top DNA duplex contains the palindromic consensus sequence 5′-GAATTC-3′. Upon binding, we expect the consensus sequence to be strengthened and the rupture probabilities to shift towards the non-binding reference duplex. Fig. 3 shows the effect of EcoRI binding for a single, representative chip with statistics from 140 chambers. While the coupling efficiency, determined by the fraction of transferred Cy3 fluorophores, is not affected (Fig. 3a), the transfer of Cy5-containing middle strands is reduced in the presence of EcoRI (Fig. 3b). These differences in transfer translate into shifted distributions of normalized fluorescence values. For the contact-*vs.*-non-contact analysis method, the median of the chambers shifts from 0.56 to 0.73 (Fig. 3c). For the top-*vs.*-bottom analysis method, it shifts from 0.54 to 0.75 (Fig. 3d). These values are in good agreement with each other. Literature values from previous MFA studies with 20 bp oligomer samples and references show the same trend, with slightly differing absolute values, namely an increase from 0.48 to 0.62.[21] However, these differences may be explained by the oligomers' differences in length and in G/C content.

Multiplexing

The row-by-row multiplexing capabilities of the present experimental design are assessed by measuring EcoRI binding onto two different binding sequences (the EcoRI consensus sequence 5′-GAATTC-3′, and the star sequence 5′-GAATTG-3′) against four reference strands of varying lengths between 25 and 40 base pairs, on the same chip. Statistical significance for all 8 combinations is aimed for by preparing multiple chambers with the same combination of probe and reference. The variation of the normalized fluorescence dependent on the reference duplex length and the binding sequence composition is shown in Fig. 4. A drop in NF for increasing reference duplex length is indicative of a decreasing fraction of probes rupturing at the reference duplex. This observation is consistent with expectations and previous studies.[21] At the same time, the consensus sequence probe shows consistently higher NF values at all reference lengths, which indicates a more stable top duplex, in accordance with the expected higher binding affinity.[34,35] The data shown in Fig. 4 facilitates the quantitative understanding of the difference in EcoRI binding between its consensus and star sequences. At an equilibrated rupture probability of NF = 0.5, the mechanical stabilizing action of EcoRI binding to its consensus sequence is equivalent to an addition of 9.1 bp dsDNA in the reference strand. This analysis is supported by the very good agreement of the experimental results with a fit based on the Bell–Evans model.[36]

Conclusion

In the present publication, we have introduced a versatile method for the quantification of DNA–protein interactions, based on the application of pneumatic forces in a microfluidic chip. Upon force load, the relative rupture probabilities of two molecular bonds in series are determined by confocal fluorescence readout. We have characterized the method, with respect to the geometry and dynamics of the button valve. The method was validated with a known all-DNA probe. Then, we have introduced and validated an alternative analysis route, based on the comparison of the fluorophore distributions at the top and bottom surfaces of the sample chamber. Finally, we have applied the method to the study of EcoRI binding. This application involving multiple target and reference strands has illustrated the multiplexing capabilities of the setup. EcoRI was used as a model protein in this proof-of-principle experiment. It can readily be substituted, thus paving the way for studies of currently unknown protein–DNA interactions, including those of transcription factors. In particular, the binding forces of transcription factors were found to correlate strongly with functional regulation, more strongly even than occupancy levels.[10] Therefore, it is very promising to use the presented method with various protein variants and/or binding sequences. The multiplexing capabilities of the setup can be further expanded. DNA array microspotting technology has been shown to be compatible with the MFA without loss of validity.[21] One can choose to spot different binding and/or reference sequences. The chip also features back chambers for the spotting of cDNA plasmids or PCR products and for the expression of DNA binding protein. This on-chip expression will further increase multiplexing.

Acknowledgements

We thank S. R. Quake and M. Meier for invaluable help in setting up the microfluidic chip production and operation. We thank D. Aschenbrenner, K. Limmer, and P. Severin for helpful discussions. M. O. is grateful to the Elite Network of Bavaria (IDK-NBT) for a doctoral fellowship. This work was supported by the European Research Council.

References

1 A. Ozdemir and A. Stathopoulos, *Nat. Methods*, 2011, **8**, 1016–1017.
2 J. Jiricny, *Nat. Rev. Mol. Cell Biol.*, 2006, **7**, 335–346.
3 S. P. Jackson and J. Bartek, *Nature*, 2009, **461**, 1071–1078.
4 V. Hornung and E. Latz, *Nat. Rev. Immunol.*, 2010, **10**, 123–130.
5 R. Nutiu, R. Friedman, S. Luo, I. Khrebtukova, D. Silva, R. Li, L. Zhang, G. Schroth and C. Burge, *Nat. Biotechnol.*, 2011, **29**, 659–664.
6 G. D. Stormo and Y. Zhao, *Nat. Rev. Genet.*, 2010, **11**, 751–760.
7 M. T. Weirauch, A. Cote, R. Norel, M. Annala, Y. Zhao, T. R. Riley, J. Saez-Rodriguez, T. Cokelaer, A. Vedenko, S. Talukder, D. Consortium, H. J. Bussemaker, Q. D. Morris, M. L. Bulyk, G. Stolovitzky and T. R. Hughes, *Nat. Biotechnol.*, 2013, **31**, 126–134.
8 T. S. Karpova, M. J. Kim, C. Spriet, K. Nalley, T. J. Stasevich, Z. Kherrouche, L. Heliot and J. G. Mcnally, *Science*, 2008, **319**, 466–469.
9 J. L. Arlett, E. B. Myers and M. L. Roukes, *Nat. Nanotechnol.*, 2011, **6**, 203–215.
10 C. R. Lickwar, F. Mueller, S. E. Hanlon, J. G. Mcnally and J. D. Lieb, *Nature*, 2012, **484**, 251–255.
11 C. E. Massie and I. G. Mills, *EMBO Rep.*, 2008, **9**, 337–343.
12 M. L. Bulyk, X. Huang, Y. Choo and G. M. Church, *Proc. Natl. Acad. Sci. USA*, 2001, **98**, 7158–7163.
13 G. Badis, M. F. Berger, A. A. Philippakis, S. Talukder, A. R. Gehrke, S. A. Jaeger, E. T. Chan, G. Metzler, A. Vedenko, X. Chen, H. Kuznetsov, C.-F. Wang, D. Coburn, D. E. Newburger, Q. Morris, T. R. Hughes and M. L. Bulyk, *Science*, 2009, **324**, 1720–1723.
14 H. Yokoe and R. R. Anholt, *Proc. Natl. Acad. Sci. USA*, 1993, **90**, 4655–4659.
15 J. J. Li and I. Herskowitz, *Science*, 1993, **262**, 1870–1874.
16 X. Meng, M. H. Brodsky and S. A. Wolfe, *Nat. Biotechnol.*, 2005, **23**, 988–994.
17 K. Hens, J.-D. Feuz, A. Isakova, A. Iagovitina, A. Massouras, J. Bryois, P. Callaerts, S. E. Celniker and B. Deplancke, *Nat. Methods*, 2011, **8**, 1065–1070.
18 C. Albrecht, K. Blank, M. Lalic-Mülthaler, S. Hirler, T. Mai, I. Gilbert, S. Schiffmann, T. Bayer, H. Clausen-Schaumann and H. E. Gaub, *Science*, 2003, **301**, 367–370.
19 P. M. D. Severin, X. Zou, H. E. Gaub and K. Schulten, *Nucleic Acids Res.*, 2011, **39**, 8740–8751.
20 P. M. D. Severin, X. Zou, K. Schulten and H. E. Gaub, *Biophys. J.*, 2013, **104**, 208–215.
21 P. M. D. Severin and H. E. Gaub, *Small*, 2012, **8**, 3269–3273.
22 K. Limmer, D. Aschenbrenner and H. Gaub, *Nucleic Acids Res.*, 2013, **41**, e69.

23 M. Unger, H.-P. Chou, T. Thorsen, A. Scherer and S. R. Quake, *Science*, 2000, **288**, 113–116.

24 S. J. Maerkl and S. R. Quake, *Science*, 2007, **315**, 233–237.

25 J. L. Garcia-Cordero and S. J. Maerkl, *Chem. Commun.*, 2013, **49**, 1264–1266.

26 D. Gerber, S. J. Maerkl and S. R. Quake, *Nat. Methods*, 2009, **6**, 71–74.

27 L. Martin, M. Meier, S. M. Lyons, R. V. Sit, W. F. Marzluff, S. R. Quake and H. Y. Chang, *Nat. Methods*, 2012, **9**, 1192–1194.

28 M. Geertz, D. Shore and S. Maerkl, *Proc. Natl. Acad. Sci. USA*, 2012, **109**, 16540–16545.

29 N. R. Glass, R. Tjeung, P. P. Y. Chan, L. Y. Yeo and J. R. Friend, *Biomicrofluidics*, 2011, **5**, 036501.

30 J. L. Zimmermann, T. Nicolaus, G. Neuert and K. Blank, *Nat. Protoc.*, 2010, **5**, 975–985.

31 G. Neuert, C. H. Albrecht and H. E. Gaub, *Biophys. J.*, 2007, **93**, 1215–1223.

32 P. M. Fordyce, C. A. Diaz-Botia, J. L. DeRisi and R. Gomez-Sjoberg, *Lab Chip*, 2012, **12**, 4287–4295.

33 M. Levitus and S. Ranjit, *Q. Rev. Biophys.*, 2011, **44**, 123–151.

34 D. R. Lesser, M. R. Kurpiewski and L. Jen-Jacobson, *Science*, 1990, **250**, 776–786.

35 N. Y. Sidorova and D. C. Rau, *Biophys. J.*, 2004, **87**, 2564–2576.

36 E. Evans and K. Ritchie, *Biophys. J.*, 1999, **76**, 2439–2447.

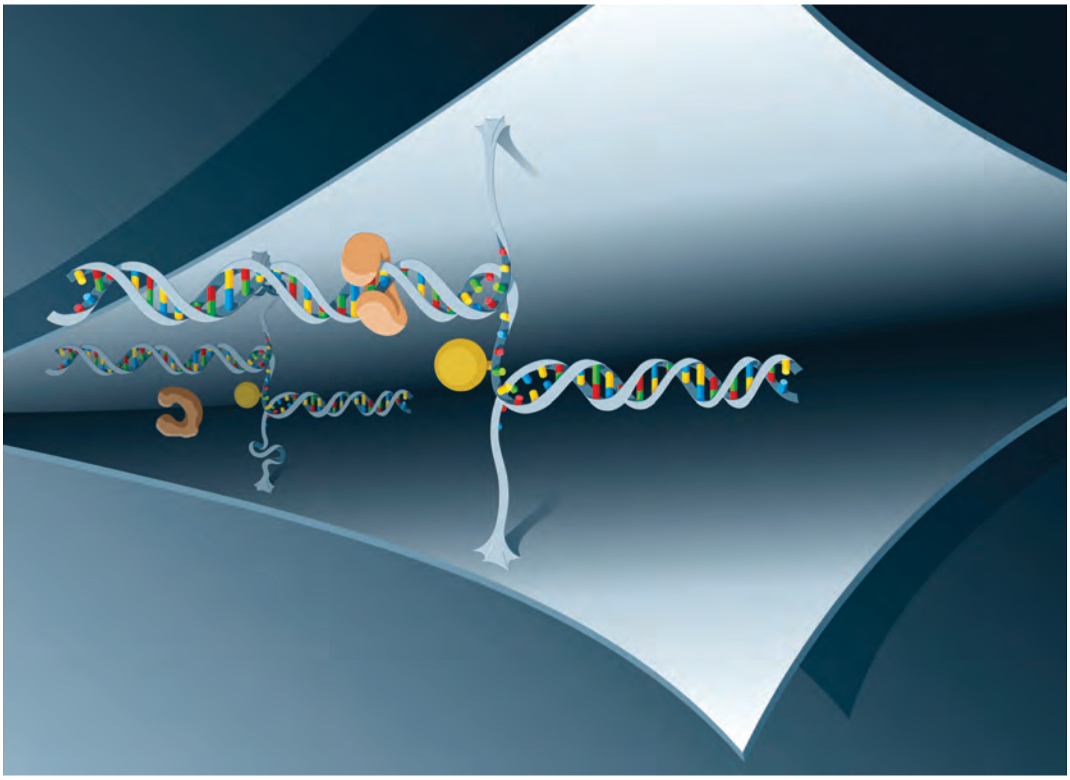

Featuring work from the Single Molecule Biophysics Laboratory of Hermann E. Gaub, Center for Nano-Science, Ludwig-Maximilians-Universität München, Germany.

Title: Protein–DNA force assay in a microfluidic format

Protein–DNA interaction forces are studied using a miniaturized and multiplexed molecular force assay on a microfluidic MITOMI chip and with a new confocal analysis method.

As featured in:

See Marcus Otten *et al.*, *Lab Chip*, 2013, **13**, 4198.

RSC Publishing

www.rsc.org/loc

Registered Charity Number 207890

5 Actin–Microtubule interaction effects on intracellular subdiffusion

The dynamical interplay between actin filaments and microtubules has been revealed in a plethora of cellular contexts, ranging from migration to division. Also its role in intracellular transport, in particular directed, ballistic transport of vesicles and other cargo has been elucidated. Nevertheless, its role in the equally frequent phases of non–ballistic movement has so far resisted uncovering.

This question – what is the effect of actin filaments and microtubules on intracellular subdiffusion? – is at the origin of this chapter and of publication P2. In the context of this thesis, in particular the interaction of these exemplary macromolecular assemblies and their impact on cell microrheology are of foremost interest.

5.1 Summary of associated publication P2

In the associated publication P2, an *in vivo* approach is chosen to study the interplay of two important macromolecular assemblies, microtubules and actin filaments, both in experiment and in simulation:

- The collective dynamics of actin filaments and microtubules and their effect in intracellular subdiffusive motion of tracer particles are elucidated, revealing both liquifying and viscosifying effects.
- A novel analysis method is introduced to resolve the lagtime–dependence of these contributions, based on a Local Mean Squared Displacement (MSD) algorithm.
- A simulational model is proposed, based solely on the Langevin equation (*i.e.* overdamped Brownian motion) and experimentally determined, colored (*i.e.* auto–correlated) Gaussian noise, and its predictions are compared to experimental data.

The associated publication P2 describes the experiment, analysis and simulation of single nanoparticle traces during their subdiffusive motion phases. Experimentally, *Dictyostelium discoideum* cells with internalized, fluorescent nanoparticles are subjected to selective cytoskeleton–depolymerizing drugs: Benomyl for microtubules and LatrunculinA for actin filaments. The resulting nanoparticle traces are screened for subdiffusive motion phases, characterized by sub–linear MSD exponents. Ballistic or directed motion phases, *e.g.* resulting from molecular motor transport, are thus excluded from the analysis. The simulational part reports the underlying model, a Langevin equation with colored Gaussian noise, its experimentally determined parameters and its very good agreement with *in vivo* data. Thus, multiple effects could be identified: First, actin filaments induce a decrease in diffusion coefficients. Second, microtubules have a liquifying effect, supposedly *via* their continuous sweeping motion. Third, and most importantly in the context of this thesis: the interaction between microtubules and actin filaments exerts a viscosifying effect on the cytoplasm at timescales larger than 0.2 s.

In summary, the results detailed in publication P2 contribute to a deeper understanding of interactions between cellular constituents relating *force* – as measured by microrheology – and *function*, in this case intracellular transport.

5.2 Associated publication P2

Local Motion Analysis Reveals Impact of the Dynamic Cytoskeleton on Intracellular Subdiffusion

by
Marcus Otten*, Amitabha Nandi*, Delphine Arcizet, Mari Gorelashvili,
Benjamin Lindner and Doris Heinrich
(* contributed equally)

published in
Biophysical Journal, **102**, 758-767 (2012)
Reprinted from Ref. [101], with permission from Elsevier.

758 Biophysical Journal Volume 102 February 2012 758–767

Local Motion Analysis Reveals Impact of the Dynamic Cytoskeleton on Intracellular Subdiffusion

Marcus Otten,[†△] Amitabha Nandi,[‡△] Delphine Arcizet,[†] Mari Gorelashvili,[†] Benjamin Lindner,[‡]
and Doris Heinrich[†*]

[†]Faculty of Physics and Center for NanoScience (CeNS), Ludwig-Maximilians-Universität, Munich, Germany; and [‡]Max Planck Institute for the Physics of Complex Systems, Dresden, Germany

ABSTRACT Intracellular transport is a complex interplay of ballistic transport along filaments and of diffusive motion, reliably delivering material and allowing for cell differentiation, migration, and proliferation. The diffusive regime, including subdiffusive, Brownian, and superdiffusive motion, is of particular interest for inferring information about the dynamics of the cytoskeleton morphology during intracellular transport. The influence of dynamic cytoskeletal states on intracellular transport are investigated in *Dictyostelium discoideum* cells by single particle tracking of fluorescent nanoparticles, to relate quantitative motion parameters and intracellular processes before and after cytoskeletal disruption. A local mean-square displacement (MSD) analysis separates ballistic motion phases, which we exclude here, from diffusive nanoparticle motion. In this study, we focus on intracellular subdiffusion and elucidate lag-time dependence, with particular focus on the impact of cytoskeleton compartments like microtubules and actin filaments. This method proves useful for binary motion state distributions. Experimental results are compared to simulations of a data-driven Langevin model with finite velocity correlations that captures essential statistical features of the local MSD algorithm. Specifically, the values of the mean MSD exponent and effective diffusion coefficients can be traced back to negative correlations of the motion's increments. We clearly identify both microtubules and actin filaments as the cause for intracellular subdiffusion and show that actin-microtubule cross talk exerts viscosifying effects at timescales larger than 0.2 s. Our findings might give insights into material transport and information exchange in living cells, which might facilitate gaining control over cell functions.

INTRODUCTION

Energy-driven dynamics and network-like organization of the cytoskeleton, with cross-linkers and molecular motors, affect intracellular transport, which is of particular interest for theoretical physics, biochemistry, and pathophysiology. A malfunctioning transport system might lead to molecular motor deficiencies in neurodegenerative diseases such as amyotrophic lateral sclerosis (1–3) or Huntington's disease (4). These medical applications motivate a detailed investigation of the underlying processes.

Cellular cytoskeleton components interact to establish multiple functions, including migration (5), division (6,7), deformation (8), and intracellular transport (9,10). In addition, molecular motors of the dynein, kinesin, and myosin families lead to different transport regimes involving directed ballistic motion, in contrast to random subdiffusion (11,12). Although molecular motors and their role in ballistic motion are a major scientific focus, the intricacies of nonballistic motion for relating structures with cell function also remain unclear (13). Subdiffusion is characterized by mean-square displacements (MSDs) obeying a power law at exponents <1 (MSD $\sim t^{\alpha}$, $\alpha < 1$) (14). The hindering or confining origins of subdiffusion can be manifold (15,16), including trapping cages, obstruction barriers, crowding, or stalling.

Caged dynamics is the favored model for nanoscale displacements of beads in the living cell cytoskeleton. Directional persistence versus antipersistence of tracer particle motion, characterized by motion angle variations, depends on the investigated timescales (17), yielding antipersistence at small timescales and persistence at larger timescales. Collisions with the cage boundaries generate motion reversal and antipersistence of the direction of motion. Cage-hopping brings about persistent motion on timescales larger than the typical cage exploration time (17). Furthermore, cellular transport behavior in these models depends on the presence of cytoskeleton components (18–20), most notably microtubules (MT), actin filaments (F-actin), and intermediate filaments. The motion type is generally quantified by the nondimensional MSD exponent α, ranging from subdiffusion to ballistic motion. Caspi et al. (9) have observed anomalous subdiffusion using live cell single particle tracking and MSD analysis: Transient α values of 1.5 and 0.75 indicate partly superdiffusive and subdiffusive modes, respectively. Experiments with both externally driven and spontaneous motion of tracer particles anchored to the cytoskeleton lead to another

---

Submitted April 15, 2011, and accepted for publication December 19, 2011.

△Marcus Otten and Amitabha Nandi contributed equally to this work.

*Correspondence: doris.heinrich@lmu.de

Amitabha Nandi's present address is Department of Molecular, Cellular and Developmental Biology, Yale University, New Haven, CT .

Benjamin Lindner's present address is Bernstein Center for Computational Neuroscience, and Physics Department, Humboldt University, Berlin, Germany.

Editor: Gijsje Hendrika Koenderink.

0006-3495/12/02/0758/10 $2.00

doi: 10.1016/j.bpj.2011.12.057

conclusion. A model of soft glassy behavior features both cages and crowding effects: Inspired by typical soft glasses, such as crowded colloidal suspensions (15,16), an analogous interpretation of the cell cytoplasm has been introduced (21). This model is based on scaling laws of the rheological moduli (22), which cannot be interpreted by simple viscoelasticity. Instead, they indicate a continuous distribution of relaxation time constants (23). Characteristics of soft glasses involve disorder and metastability in weakly attractive energy landscapes. The volume of the cage does not affect the degree of subdiffusion (the MSD exponent), but the effective diffusion coefficient. In addition, active intracellular driving forces enhance nonthermal behavior, leading to an increase in diffusion coefficient (24).

In this work, we investigate anomalous subdiffusion phases of intracellular transport in detail, with a particular emphasis on the involved cytoskeleton components and the various timescales on which they act. Our experimental model system, the cytoskeleton in *Dictyostelium discoideum* cells is composed of MTs and F-actin. Intermediate filaments are absent. Benomyl and Latrunculin A are used as depolymerization agents of MT and F-actin, respectively. To study their influence on subdiffusion, we employ a local MSD algorithm to separate out phases of active transport along filaments and focus on phases of subdiffusion.

In terms of a theoretical description, pure diffusion in a highly viscous medium without active contributions is governed by overdamped Brownian motion corresponding to a simple Langevin equation. Even in this simple situation, the local MSD algorithm at a particular time instant does not yield uniquely determined values of exponent and diffusion coefficient but values that scatter around the expected mean values with characteristic distributions. This is the case because the MSD algorithm at a particular instant in time uses only a small sample of data (otherwise it would not be local in time anymore). It is instructive to compare distributions obtained from simulations of a Langevin equation to those obtained from intracellular particle trajectories. Although the two kinds of distributions are qualitatively similar, we will discuss important differences and we present a simple data-driven extension of the classical Langevin model, which describes the motility of the tracer particle within the living cell under various conditions. In this approach, the common white (uncorrelated) Gaussian noise of the standard overdamped Langevin equation is replaced by a colored (correlated) Gaussian noise accounting for finite temporal correlations of the particle's velocity. The correlation function of this noise (velocity) is taken from the experimental data measured under the respective conditions in living cells. Our results indicate that important aspects of the statistics resulting from the local MSD algorithm (distributions of exponent and diffusion coefficient; their mean values as a function of the MSD algorithm's timescale) can be understood solely based on such a Gaussian model with finite velocity correlations.

We will present results and their implications on intracellular transport in three consecutive steps: First, the transport parameters are introduced for regular diffusion in glycerol and motion in living cells. These parameters are then studied for different cytoskeleton states for depolymerized MT and/or F-actin. Finally, this cytoskeleton analysis is extended to include lag time-dependent effects of MT and F-actin on subdiffusion.

MATERIALS AND METHODS

Cell culture

D. discoideum cells of the AX2 wild-type (WT) strain (25), provided by the Max-Planck-Institut für Biochemie (Martinsried, Germany), are maintained at 21°C on tissue culture dishes in AX2 medium. Cells are kept in the exponential growth phase and below 50% confluence by addition of fresh nutrient medium every 48 h. To verify cytoskeleton depolymerization agent effects, cells of the LimEΔcc-GFP (26) and α-Tub-GFP (provided by the Max-Planck-Institute for Biochemistry) strains are used. Gentamycin and Blasticidin antibiotics are added for preservation of the mutation. Before experiments, AX2 medium is replaced by nonfluorescent medium, lacking yeast extract and peptone.

Nanoparticles

Nanoscreen MAG-D nanoparticles (ChemiCell, Germany) of 150 nm diameter are added to the cell suspension at a final concentration of 18.25 nM. Before uptake, nanoparticles (NPs) are agitated by vortexing for 10 s and by supersonication for 5 min. The sterile, green-fluorescent magnetic NPs consist of a superparamagnetic iron oxide core (Fe_2O_3), surrounded by a lipophilic green-fluorescent dye, with excitation wavelength 476 nm and an emission maximum at 490 nm. The dye is surrounded by a hydrophilic outer polymer matrix of polysaccharide starch ($C_6H_{10}O_5$). NP uptake is performed by slow centrifugation at 3000 rpm in a Heraeus Biofuge Pico centrifuge in four subsequent legs of 3, 4, 4, and 5 min duration, respectively, each followed by gentle agitation and 5 min at rest to prevent undue stress on the cells. Directly after the final centrifugation, supernatant medium is replaced by nonfluorescent medium. Excess NPs are removed.

Cytoskeleton depolymerization agents

A Benomyl ($C_{14}H_{18}N_4O_3$, Sigma-Aldrich, Germany) solution in phosphate buffered saline is added 30 min before MT depolymerization measurements to the NP-cell suspension at a concentration of 100 μM. A diluted Latrunculin A ($C_{22}H_{31}NO_5S$, Invitrogen, Germany) solution in phosphate buffered saline is added 20 min before F-actin depolymerization measurements to the NP-cell suspension at a concentration of 10 μM.

Microscopy

The sample chamber consists of a 24 mm × 40 mm glass coverslip and an 18 mm × 18 mm teflon enclosure and is mounted on an Axiovert 135 TV microscope (Zeiss, Germany) equipped with an EC-Plan Neofluar 100×/1.3NA oil-immersion objective (Zeiss) and an Orca C4880-80 charge-coupled device camera (Hamamatsu, Germany) with a sampling and exposure time of 49 ms per frame of size 384 × 384 pixels, where one pixel corresponds to 0.064 μm × 0.064 μm. The fluorescence intensity distribution is fitted by a two-dimensional Gaussian to determine the particle's position at subpixel resolution using the OpenBox (27) software, version 1.9.

Statistics of the trajectory's increments

We analyze the trajectory in terms of the increments in x and y between consecutive frames (time steps) $\Delta x_i = x_{i+1} - x_i$ and $\Delta y_i = y_{i+1} - y_i$. We estimate probability densities of these increments by standard methods and also calculate their correlation coefficient, e.g., the one for increments in x:

$$\rho_k^{xx} = \frac{\langle(\Delta x_{i+k} - \langle\Delta x_{i+k}\rangle)(\Delta x_i - \langle\Delta x_i\rangle)\rangle}{\langle(\Delta x_i - \langle\Delta x_i\rangle)^2\rangle}, \qquad (1)$$

where $\langle\ldots\rangle$ indicates the average that is taken over the index i. We also measure the correlations ρ_k^{yy} of the increments in y and those ρ_k^{xy} between the increments in x and y. The serial correlation coefficient in Eq. 1 is a measure for the randomization of subsequent steps: vanishing autocorrelation indicates complete independence, whereas unit autocorrelation indicates unchanged increment values from one frame to the next. A negative increment correlation indicates antipersistent behavior and results in a reduced randomness on longer timescales because in the sum of the increments, i.e., in the particle's trajectory, anticorrelated terms partially cancel. This reduced long-term variability may become manifest by an apparent subdiffusive behavior on timescales over which the increment correlations extend.

To estimate the error bar of the correlation coefficient, we use the following equation for the variance of the correlation coefficient (28):

$$\mathrm{Var}(\rho_k) \approx \frac{1 + 2\sum_{j=1}^{\nu}\left(1 - \frac{j}{n}\right)\rho_j^2}{(n-k)(1 + 2\nu/n - \nu^2/n^2)}, \qquad (2)$$

where n is the total number of increments and ν is the maximal lag taken into account, which we set to $\nu = 20$. The error bar for one measurement is then the square root of the variance.

Local MSD algorithm

The algorithm

A conventional method of analyzing intracellular transport is based on the MSD:

$$\begin{aligned}\langle\Delta R^2(\tau)\rangle &= \langle[\boldsymbol{R}(t+\tau) - \boldsymbol{R}(t)]^2\rangle_t \\ &= \langle[x(t+\tau) - x(t)]^2 + [y(t+\tau) - y(t)]^2\rangle_t. \qquad (3)\end{aligned}$$

Local MSD analysis has been introduced previously (29), yielding time-resolved motion type information: For each point along the recorded trajectory a local MSD is computed, considering only the neighboring 60 trajectory points. This local MSD is then fitted by a power law (linear regression in a double-logarithmic MSD plot)

$$\begin{aligned}\langle\Delta R^2(\tau)\rangle &= \langle(\boldsymbol{R}(t'+\tau)\text{-}\boldsymbol{R}(t'))^2\rangle_{t\text{-}T/2<t'<t+T/2\text{-}\tau} \\ &= A \times \left(\frac{\tau}{\tau_0}\right)^{\alpha}, \qquad (4)\end{aligned}$$

yielding the same characteristics as the global MSD, but in a local, time-resolved manner and with additional noise because of the smaller sample. Here τ_0 is a reference time and A has dimensions of the square of a length. The exponent α is a dimensionless number between 0 and 2, indicating different types of motion: $\alpha < 1$ being subdiffusive, $\alpha \approx 1$ Brownian-like, $\alpha > 1$ superdiffusive and $\alpha \approx 2$ ballistic. The prefactor contains an effective diffusion coefficient (see below) or in the case of ballistic motion the velocity. This analysis and fit are repeated for each point along the trajectory resulting in time series for the parameters α and A. In this work, we study long phases of nonballistic transport (typically subdiffusive behavior) in terms of the statistical distributions of the exponent α and the effective diffusion coefficient D, which is proportional to the parameter A.

Parameter settings

The timescale at which the sample is probed depends on the frame rate and the window size. The window size determines the number of points taken into account for the computation of the local MSD, but does not equal the lag time range over which the power law is fitted to the data. For large lag times of $\tau \approx \mathrm{M_w} \times \Delta t$, only a few MSD data points exist within each window, and the statistics risk to be unreliable. Therefore, the fit data range is chosen to be $0 < \tau < 1/4 \times \mathrm{M_w} \times \Delta t$. Thus, the timescale probed by the local MSD is of the order $1/4 \times \mathrm{M_w} \times \Delta t$. We have chosen the values to be $\mathrm{M_w} = 60$ and $\Delta t = 49$ ms, which corresponds to 15 MSD points and a probing at 0.735 s. Experimental and simulational data of bead motion in glycerol were collected at $\Delta t = 55$ ms and analyzed accordingly at $\mathrm{M_w} = 60$. For the analysis of mean motion parameters as functions of lag time, the window size was varied from $\mathrm{M_w} = 8$ frames to $\mathrm{M_w} = 200$ frames in 4-frame steps, including the 60-frame window as a special case. The 4-frame increases in window size and the MSD fit data range of $1/4 \times \mathrm{M_w} \times \Delta t$ amount to a lag time resolution of 49 ms. The power law fit yields reliable results for all investigated window sizes, which was checked using the chi-square measure, which equals $\chi^2 = 0.013$ ($\mathrm{M_w} = 60$) and $\chi^2 = 0.05$ ($\mathrm{M_w} = 200$).

For Brownian diffusion, the MSD scales linearly with time: $\langle\Delta R^2\rangle^2 = A \times \tau/\tau_0$ and the prefactor A determines the diffusion coefficient: $A = 2d\ \tau_0\ \mathrm{D}$ (d is the number of spatial dimensions), which corresponds to $D = \langle\Delta R^2\rangle/(2d\tau)$. For MSD power laws with other exponents, $\alpha \neq 1$, an effective diffusion coefficient (with proper dimension $\mu\mathrm{m}^2/\mathrm{s}$) is directly proportional to the prefactor A if we choose the reference time as the time lag, i.e., for $\tau = \tau_0$ we obtain $D = A/(2d\ \tau_0)$—otherwise the diffusion coefficient will depend explicitly on α. This definition permits a volume-explored interpretation of this effective diffusion coefficient, for a characteristic volume measure can be obtained from projecting the two-dimensional MSD into the third dimension.

Models

Langevin models of intracellular motion

The standard overdamped Brownian motion in a viscous medium is described by the Langevin equation:

$$\begin{aligned}\frac{dx}{dt} = \xi^x(t), \quad \frac{dy}{dt} = \xi^y(t),& \\ \langle\xi^a(t)\xi^b(t')\rangle = 2D\delta_{a,b}\delta(t-t'),&\end{aligned} \qquad (5)$$

with D being the spatial diffusion coefficient; $\xi(t)$ is a white Gaussian noise that models the velocity. A numerical simulation of this model at time step Δt is realized by the simple map:

$$x_i = x_{i-1} + \xi_i^x, \quad y_i = y_{i-1} + \xi_i^x, \quad \langle\xi_i^a\xi_j^b\rangle = 2D\Delta t\delta_{a,b}\delta_{i,j}, \qquad (6)$$

The numbers ξ_i^x, ξ_i^y are independent Gaussian numbers with zero mean and variance $2D\Delta t$. The differences in the trajectory between adjacent time instances, i.e., the increments are thus statistically independent and, in particular, uncorrelated. We used the previous scheme to simulate the tracer particle's diffusion in glycerol.

In this work, we also consider a generalization of the previous equation, in which we replace the white (uncorrelated) Gaussian velocity noise by a colored (correlated) Gaussian velocity noise. We will work exclusively with a discretized version of the Langevin equation and also use a linear map, an autoregressive process (AR) for the generation of the colored noise:

$$x_i = x_{i-1} + v_i^x \Delta t, \quad y_i = y_{i-1} + v_i^y \Delta t,$$

$$\begin{aligned} v_i^x &= \sum_{k=1}^{K} \left(c_k^{xx} v_{i-k}^x + c_k^{xy} v_{i-k}^y \right) + \xi_i^x, \\ v_i^y &= \sum_{k=1}^{K} \left(c_k^{yx} v_{i-k}^x + c_k^{yy} v_{i-k}^y \right) + \xi_i^y. \end{aligned} \tag{7}$$

Noise sources in x and y can be correlated but are always uncorrelated in time, i.e., $\langle \xi_i^x \xi_j^x \rangle = \delta_{i,j} \sigma_{xx}^2, \langle \xi_i^y \xi_j^y \rangle = \delta_{i,j} \sigma_{yy}^2, \langle \xi_i^x \xi_j^y \rangle = \delta_{i,j} \sigma_{xy}$. Note that for $c_k^{xx} = c_k^{yy} = c_k^{yx} = c_k^{xy} = \sigma_{xy} = 0$ (for all k) and $\sigma_{xx}^2 = \sigma_{yy}^2 = 2D/\Delta t$, the model reduces to the simple Brownian motion in Eq. 6.

For each data set, we determine the coefficients of the AR process from (see, e.g. (30).)

$$c^x = B_x^{-1} \psi_x, \quad c^y = B_y^{-1} \psi_y. \tag{8}$$

Here, $c^x = (c_1^{xx}, c_2^{xx}, \ldots, c_1^{xy}, \ldots, c_K^{xy}), c^y = (c_1^{yy}, c_2^{yy}, \ldots, c_1^{yx}, \ldots, c_K^{yx})$ and $\psi_k^{ab} = \langle v_{i-k}^a v_i^b \rangle = \langle v_i^a v_i^b \rangle \rho_k^{ab}$ give the r.h.s. by $\psi^x = (\psi_1^{xx}, \psi_2^{xx}, \ldots, \psi_1^{xy}, \ldots, \psi_K^{xy}), \psi^y = (\psi_1^{yy}, \psi_2^{yy}, \ldots, \psi_1^{yx}, \ldots, \psi_K^{yx})$ and

$$\begin{aligned} B_x &= \begin{bmatrix} \psi_0^{xx} \cdots & \psi_{K-1}^{xx} & \psi_0^{xy} \cdots & \psi_{K-1}^{yx} \\ \cdots & \cdots & \cdots & \cdots \\ \psi_{K-1}^{xx} & \psi_0^{xx} & \psi_{K-1}^{xy} & \psi_0^{yx} \\ \psi_0^{yx} \cdots & \psi_{K-1}^{xy} & \psi_0^{yy} & \psi_{K-1}^{yy} \\ \cdots & \cdots & \cdots & \cdots \\ \psi_{K-1}^{yx} \cdots & \psi_0^{yx} & \psi_{K-1}^{yy} \cdots & \psi_0^{yy} \end{bmatrix}, \\ B_y &= \begin{bmatrix} \psi_0^{yy} \cdots & \psi_{K-1}^{yy} & \psi_0^{yx} \cdots & \psi_{K-1}^{xy} \\ \cdots & \cdots & \cdots & \cdots \\ \psi_{K-1}^{yy} & \psi_0^{yy} & \psi_{K-1}^{yx} & \psi_0^{xy} \\ \psi_0^{xy} \cdots & \psi_{K-1}^{yx} & \psi_0^{xx} & \psi_{K-1}^{xx} \\ \cdots & \cdots & \cdots & \cdots \\ \psi_{K-1}^{xy} \cdots & \psi_0^{xy} & \psi_{K-1}^{xx} \cdots & \psi_0^{xx} \end{bmatrix} \end{aligned} \tag{9}$$

Once the coefficients have been found from solving Eq. 8, the variances and covariance of the noise sources can be calculated from

$$\begin{aligned} \sigma_{xx}^2 &= \psi_0^{xx} - \sum_{k=1}^{K} \left(c_k^{xx} \psi_k^{xx} + c_k^{xy} \psi_k^{xy} \right), \\ \sigma_{xy} &= \psi_0^{xy} - \sum_{k=1}^{K} \left(c_k^{xx} \psi_k^{xy} + c_k^{xy} \psi_k^{yy} \right), \\ \sigma_{yy}^2 &= \psi_0^{yy} - \sum_{k=1}^{K} (c_k^{yy} \psi_k^{yy} + c_k^{yx} \psi_k^{yx}). \end{aligned} \tag{10}$$

To sum up, if we know the covariance, the variances, and the correlation coefficients of the increments in x and y up to lag K, we can determine an AR model, that has Gaussian increments and the same linear correlations as the data. For simulation of all intracellular data, we used Eq. 7 with $K = 100$ (dimension of the AR process). The large set of correlations coefficients $K = 100$ is only needed to reproduce correctly the long-term behavior (see Fig. 5) for the mean values as a function of maximum lag time.

RESULTS AND DISCUSSION

Our study of the cytoskeletal influence on intracellular subdiffusion draws on the combination of experimental NP trajectories and simulations thereof, which are analyzed using a local MSD algorithm (29). We observe internalized NPs inside living cells using fluorescence microscopy. Frame-by-frame tracking yields NP trajectories, which are evaluated by a local MSD analysis, as laid out in the Methods section and depicted schematically in Fig. 1. Local MSD transport variables are studied in various *D. discoideum* cytoskeleton environments, including partial or complete depolymerization. In this work, we select diffusive motion states exclusively, disregarding active intracellular transport phases, mediated by motor-driven filament attachment. This distinction is performed by the local MSD analysis (29). In this study, we use only the subdiffusive motion phases to compare the impact of different cytoskeleton depolymerization states for finite size experimental tracks.

Increment statistics

We first compare the motion of fluorescent NPs in glycerol and in living WT cells' cytoplasm. This exemplifies the analysis method, highlights the differences between Brownian motion and intracellular motility, and yields insight into the importance of increment statistics. Increment statistics consist of a size distribution and their temporal autocorrelation function, which are shown in Fig. 2, *a* and *b*, for trajectories in glycerol and in WT cells' cytoplasm, respectively. Gaussian fits to the experimental data are also shown.

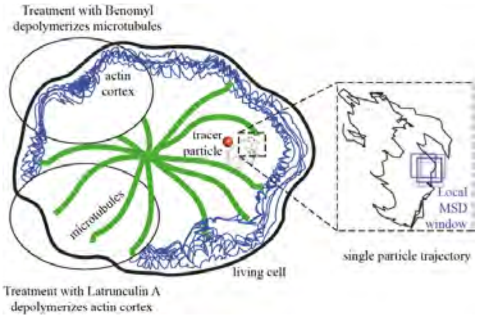

FIGURE 1 Tracking of single NPs, transported in living *D. discoideum* cells, yields this type of trajectories. Cytoskeleton depolymerization agents, namely Benomyl and Latrunculin A, are used to discern the influence of particular cytoskeleton constituents, MT and F-actin, on the intracellular transport. Trajectories are analyzed using a local MSD algorithm shifting a rolling window across the NP trajectories.

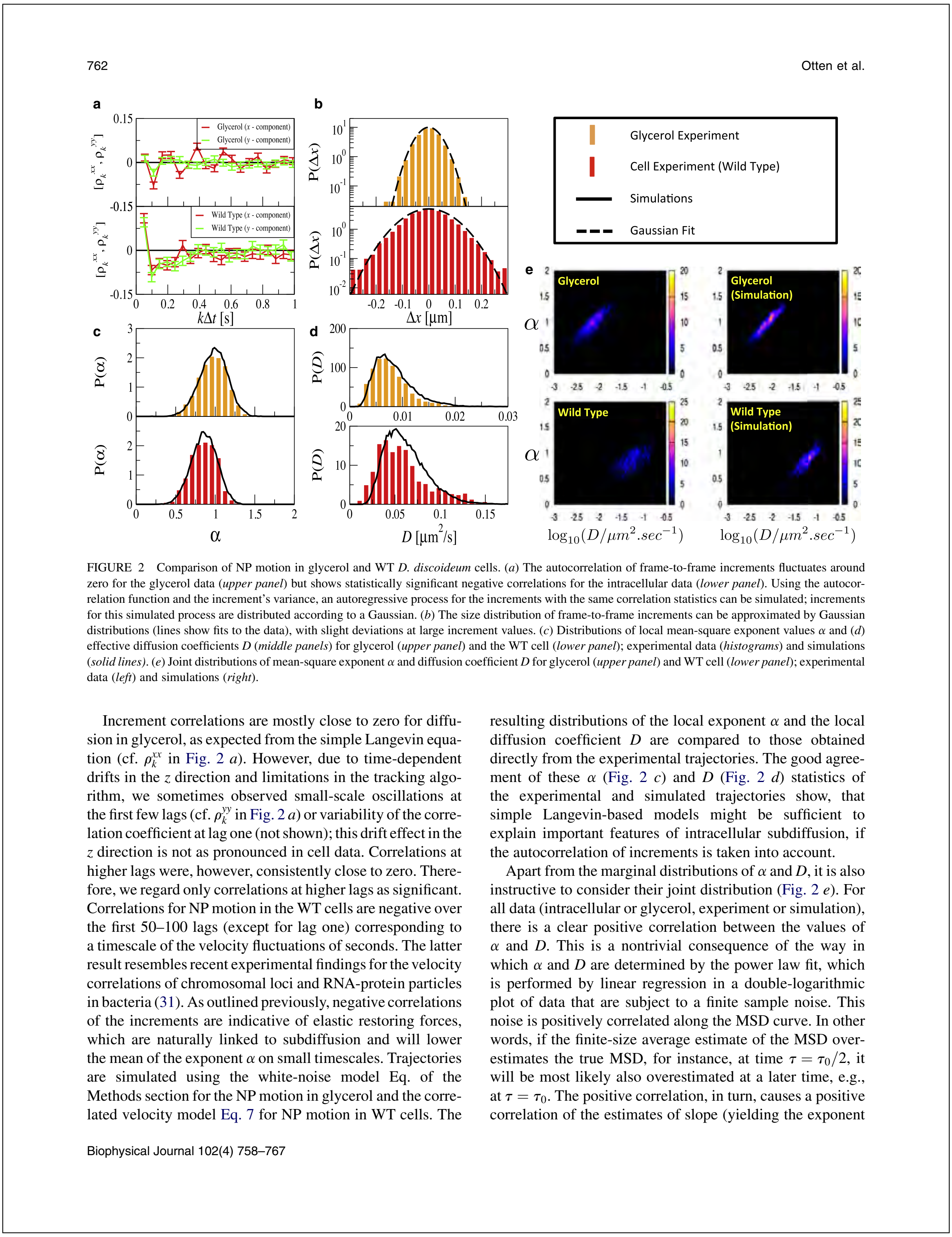

FIGURE 2 Comparison of NP motion in glycerol and WT *D. discoideum* cells. (*a*) The autocorrelation of frame-to-frame increments fluctuates around zero for the glycerol data (*upper panel*) but shows statistically significant negative correlations for the intracellular data (*lower panel*). Using the autocorrelation function and the increment's variance, an autoregressive process for the increments with the same correlation statistics can be simulated; increments for this simulated process are distributed according to a Gaussian. (*b*) The size distribution of frame-to-frame increments can be approximated by Gaussian distributions (lines show fits to the data), with slight deviations at large increment values. (*c*) Distributions of local mean-square exponent values α and (*d*) effective diffusion coefficients D (*middle panels*) for glycerol (*upper panel*) and the WT cell (*lower panel*); experimental data (*histograms*) and simulations (*solid lines*). (*e*) Joint distributions of mean-square exponent α and diffusion coefficient D for glycerol (*upper panel*) and WT cell (*lower panel*); experimental data (*left*) and simulations (*right*).

Increment correlations are mostly close to zero for diffusion in glycerol, as expected from the simple Langevin equation (cf. ρ_k^{xx} in Fig. 2 *a*). However, due to time-dependent drifts in the z direction and limitations in the tracking algorithm, we sometimes observed small-scale oscillations at the first few lags (cf. ρ_k^{yy} in Fig. 2 *a*) or variability of the correlation coefficient at lag one (not shown); this drift effect in the z direction is not as pronounced in cell data. Correlations at higher lags were, however, consistently close to zero. Therefore, we regard only correlations at higher lags as significant. Correlations for NP motion in the WT cells are negative over the first 50–100 lags (except for lag one) corresponding to a timescale of the velocity fluctuations of seconds. The latter result resembles recent experimental findings for the velocity correlations of chromosomal loci and RNA-protein particles in bacteria (31). As outlined previously, negative correlations of the increments are indicative of elastic restoring forces, which are naturally linked to subdiffusion and will lower the mean of the exponent α on small timescales. Trajectories are simulated using the white-noise model Eq. of the Methods section for the NP motion in glycerol and the correlated velocity model Eq. 7 for NP motion in WT cells. The resulting distributions of the local exponent α and the local diffusion coefficient D are compared to those obtained directly from the experimental trajectories. The good agreement of these α (Fig. 2 *c*) and D (Fig. 2 *d*) statistics of the experimental and simulated trajectories show, that simple Langevin-based models might be sufficient to explain important features of intracellular subdiffusion, if the autocorrelation of increments is taken into account.

Apart from the marginal distributions of α and D, it is also instructive to consider their joint distribution (Fig. 2 *e*). For all data (intracellular or glycerol, experiment or simulation), there is a clear positive correlation between the values of α and D. This is a nontrivial consequence of the way in which α and D are determined by the power law fit, which is performed by linear regression in a double-logarithmic plot of data that are subject to a finite sample noise. This noise is positively correlated along the MSD curve. In other words, if the finite-size average estimate of the MSD overestimates the true MSD, for instance, at time $\tau = \tau_0/2$, it will be most likely also overestimated at a later time, e.g., at $\tau = \tau_0$. The positive correlation, in turn, causes a positive correlation of the estimates of slope (yielding the exponent

α) and intercept with the log[MSD]-axis (yielding the diffusion coefficient). (Even if the finite-sample noise would be uncorrelated and equal in intensity for each data pair $[\log(\tau/\tau_0),\ \log(MSD(\tau))]$, the estimates of α and D would be positively correlated, although weaker than in the case of positively correlated MSD fluctuations.)

In all cases, probability is distributed along and around a line in the α-D plane, the position and slope of which agrees fairly well for experimental and simulation data. For the glycerol data in Fig. 2 *e*, also the width of the distribution is in good agreement for experiment and simulation. For the WT data, however, there is a significant difference between model simulations and experimental results: the experimental data exhibit a broader distribution around the aforementioned line. This difference is found for all intracellular data (see Fig. 4 *c*). The larger width of the experimental distribution may be caused by inhomogeneities within the cytoplasm, not incorporated in our model, such as the weak non-Gaussian statistics of the increments or higher-order correlations (the autoregressive process Eq. 7 reproduces only the second-order statistics). However, we expect slight experimental errors for the glycerol and WT cell experiments.

Subdiffusive phenomena after cytoskeleton depolymerization

We extend increment statistics based on the analysis of WT cells to modified cytoskeleton states. *D. discoideum* cells show the rare capacity to survive despite cytoskeleton depolymerization. The four investigated cytoskeleton states are WT cytoskeleton, depolymerized MT (Benomyl), depolymerized F-actin (Latrunculin A), and simultaneous depolymerization of MT and F-actin (Benomyl and Lat A). Fig. 3 shows the autocorrelation of increments for these four different cytoskeleton states. The former three conditions, characterized by the presence of at least one of the cytoskeleton constituents, show very similar behavior: the increment autocorrelation function is consistently negative at higher time differences. The case of simultaneous depolymerization of both cytoskeleton constituents displays significantly different increment statistics with positive autocorrelation at higher time differences. These findings indicate a fundamental difference between partial and complete cytoskeleton depolymerization, but do not yield direct insight into the consequences on intracellular transport. In addition, increment distributions show in some cases deviations from the fitted Gaussians at large arguments, which can be interpreted as an indication for a nonequilibrium dynamics at work in the cell.

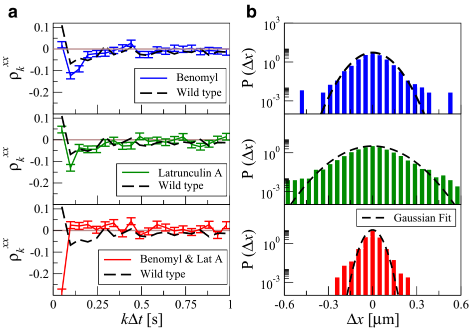

FIGURE 3 Increment correlation coefficient in x (*a*) and histograms of increments in x (*b*) in three different cytoskeleton states: WT cells (*black lines without error bars*) as reference, Benomyl-assisted MT depolymerization (*first row*), Latrunculin A-assisted F-actin depolymerization (*second row*), and simultaneous MT and F-actin depolymerization (*third row*). Correlations and histograms were similar for all cases when measured for the increments of y instead of x.

We applied the local MSD analysis algorithm to both, experimental trajectories and simulations using experimental increment statistics. Indeed, the four cases can be well differentiated by their local α and D distributions, as depicted in Fig. 4. Experimental and simulated distributions again show good agreement. The α distributions in Fig. 4 *a* show various degrees of subdiffusion, quantified by the mean value of the MSD exponent $\langle\alpha\rangle$. The experimental mean values for $\langle\alpha\rangle$ are 0.85 (WT), 0.76 (Benomyl), 0.79 (Latrunculin A), and 0.90 (Benomyl and Latrunculin A). Furthermore, the mean diffusion coefficient shows characteristic behavior for each cytoskeleton state: In total absence of both MT and F-actin, the mean diffusion coefficient $\langle D\rangle$ equals 0.86×10^{-2} μm^2/s. In contrast, presence of at least one cytoskeleton constituent leads to enhanced diffusion coefficients, with mean values of $\langle D\rangle$ amounting to 6.10×10^{-2} μm^2/s (WT), 3.53×10^{-2} μm^2/s (Benomyl), and 10.7×10^{-2} μm^2/s (Latrunculin A), as shown in Fig. 4 *b*.

The joint α-D distributions are shown in Fig. 4 *c*. As already discussed for the WT data in Fig. 2 *e*, the widths of the joint distributions are larger in the experiment than in the simulational data, in particular in the case of complete cytoskeleton depolymerization by application of both Benomyl and Latrunculin A. Thus, the increase in the width of the joint distribution can be attributed to an effect, which is not mediated by F-actin or MT. The large spread of the experimental P(α,D) is not accounted for in our model and may be resolved by further intracellular transport studies whose scope extends beyond the influence of the cytoskeletal main players.

Microtubule and F-actin depolymerization

After removal of MT and F-actin, we observe a Brownian-like diffusion characterized by $\alpha \approx 1$ and a low D, contrary to enhanced subdiffusion in WT cells, characterized by $\alpha < 1$ and a high D. In the absence of both, MT sweeping motion and actin cortex rearrangement, no other active cytoskeleton components, driven for example by ATP-consuming

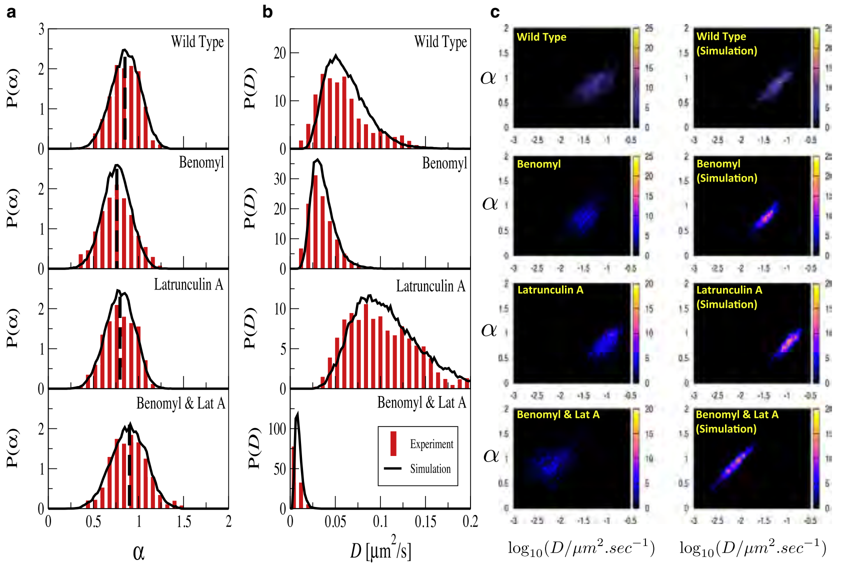

FIGURE 4 Distributions of α (*a*), of D (*b*), and their joint distribution (*c*) in various cytoskeleton states: WT cells (*top row*), Benomyl-assisted MT depolymerization (*second row*), Latrunculin A-assisted F-actin depolymerization (*third row*), and simultaneous MT and F-actin depolymerization (*bottom row*) for both experimental data (*red bars*) and simulations (*black lines*). In *a* mean values of α are indicated by vertical dashed lines.

molecular motor cross-links, are capable of inducing active behavior or specific forces due to the polymerization of actin or MTs. This result is a strong indicator for the importance of the enhancing effect of actively driven cytoskeleton components on subdiffusion (24). *D. discoideum* cells survive instantaneous depolymerization of the actin cortex and of MT, as depolymerization of cytoskeleton components in the living cell can never be complete. Small amounts of F-actin and little MT-stumps persist in the cell, enabling the bare survival of the cell by contributing little to active processes. It is thus in concordance with our model with velocity correlations to assume a nonequilibrium system, even in the case of simultaneous MT and F-actin depolymerization.

Microtubule depolymerization

Selective removal of MTs alters cell behavior: ballistic transport via biomotors is impossible (32). However, this effect is filtered from our subdiffusive motion data by analysis with the local MSD algorithm. In the context of subdiffusion, the MT sweeping causes long range effects for the NPs: Active MT sweeping motion renders the cytoplasm more fluid-like and viscous, its absence thus more solid-like. We expect a decrease in spatial extent of the volume probed by the particle. As the effective diffusion constant is directly calculated from local MSD values, it gives an estimate of the volume probed per unit time and our experimental results do show a slight decrease in D in the absence of MTs.

F-actin depolymerization

F-actin mediates migration, so F-Actin-depleted cells show accompanying effects, such as rounding up and immotility, in addition to changes in intracellular transport. We find that depolymerization of F-actin causes a slight drop in α with respect to WT cells, a sign of enhanced elastic properties of the cytoplasm and lack of actin pushing forces. As in the case of MT depletion, this more elastic-like behavior can be attributed to the absence of myosin II motors along actin filaments and actin polymerization dynamics. Second, we find increasing $\langle D\rangle$ values, which is a sign of a larger volume probed by the tracer particle, in the absence of a densely packed actin network. These seemingly contradictory observations result from the absence of myosin-actin activity.

The closely cross-linked actin cortex undergoes active rearrangements, driven for example by ATP-consuming actomyosin (33). Entangled actin networks, which were reconstituted in vitro, were probed by bead microrheology (34). It was found that viscosity is prevalent at high frequencies, down to 1 Hz, which corresponds to a probing on the 1 s timescale. The scaling of the viscoelastic moduli as $\omega^{3/4}$ yields a MSD exponent of $\alpha = 3/4$ at these timescales, similar to values observed experimentally for tracer particles (35). At larger times, the elastic properties prevail and the MSD exponent α experiences a drop down to ~0.32. These data, both in vitro (34) and in living cells, as reported in this work, support the hypothesis of a viscosifying effect of F-actin at timescales smaller than or comparable to 1 s. The exact crossover time depends on filament length (34) and probe size (36). It seems plausible that it also depends on motor presence and ATP concentration, which must be kept in mind when comparing quantitative in vitro and in vivo data.

Lag-time dependence

Up to now, effects of cytoskeleton disruption were investigated at one specific maximal lag time of 0.735 s. We now investigate the lag-time dependence and, in particular, the lag time-dependent α and D statistics by varying the window size from $M_w = 8$ frames to $M_w = 200$ frames, always keeping the MSD fit data range at $1/4 \times M_w$ points. This corresponds to a range of the maximal lag times from 0.098 to 2.45 s. The results of these experiments and simulations are shown in Fig. 5, again for the previously studied four cytoskeleton states: WT, MT depolymerization, F-actin depolymerization, and simultaneous depolymerization of MT and F-actin. The α statistics show good agreement between experimental and simulation results at all maximal lag times (Fig. 5 *a*); for comparison, we show the mean alpha for NP diffusion in glycerol, which remains close to one for all lag times. The cytoskeleton states with only one depolymerized component display qualitatively similar behavior to WT, whereas the case of simultaneous depolymerization of both components is qualitatively different. Here, we find a smaller degree of subdiffusion. This is indicated by larger mean α values at maximal lag times >0.6 s. The respective diffusion coefficients are smaller (Fig. 5 *b*). At lag times larger than ~1 s, the mean diffusion coefficients approach plateau values, with actin-depleted cells exceeding WT and MT-depleted cells' plateau values. Overall, the strong variations of the mean alpha versus maximal lag time is another indication that intracellular motility is far more complicated than simple Brownian motion (cf. $\langle\alpha\rangle$ for the glycerol data, which does not vary much—even if one excludes active transport along filaments and focuses on apparently passive phases of motion. A weak variation of mean alpha versus maximal lag time can be also expected from simple Brownian motion; see our simulation results, which yield $\langle\alpha\rangle$ close to but slightly smaller than one. This will be studied in detail elsewhere.)

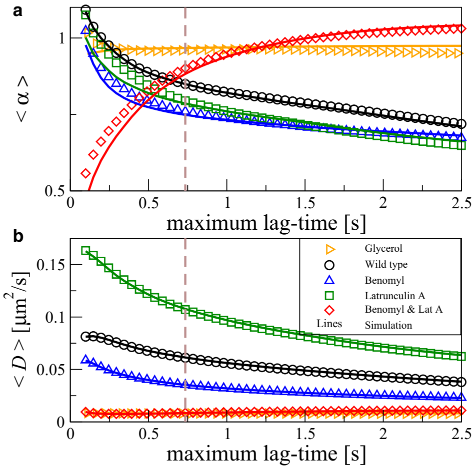

FIGURE 5 Lag-time dependence of the local MSD exponent $\langle\alpha\rangle$ (*a*) and the mean effective diffusion coefficient $\langle D\rangle$ (*b*) in various cytoskeleton states: WT cells (experiments as *black circles*, simulations as *black line*), Benomyl-assisted MT depolymerization (exp: *blue triangles*, sim: *blue line*), Latrunculin A-assisted F-actin depolymerization (*green squares*, *green line*), simultaneous MT and F-actin depolymerization (*red diamonds*, *red line*), and as reference NP diffusion in glycerol (*yellow triangles*, *yellow line*) for both experimental data (*symbols*) and simulations (*solid lines*). Data shown in Fig. 4 *a* correspond to a lag time of 0.735 s (*vertical dashed line*).

Microtubule and F-actin depolymerization

In cells of simultaneous MT and F-actin depolymerization, response is twofold: At lag times larger than 1.0 s, intracellular motion is nearly Brownian with $\alpha \approx 1$ and low diffusion coefficients, consistently below 1.1×10^{-2} μm^2/s, comparable to the glycerol data. This result stresses the active role these cytoskeleton components play in subdiffusion and highlights the importance of the cytoskeleton at these lag times. In this case, subdiffusion can be observed up to lag times of 0.8 s with diffusion constants of 7.6×10^{-3} μm^2/s at lag times between 0.25 and 0.30 s. This is a sign of near standstill of the tracer particle motion, due to absence of MT and F-actin dynamics. However, remnants of the polymer networks persist, acting as cages on small timescales, in addition to intracellular crowding effects.

In the case of an intact WT cytoskeleton, the drop in α from diffusion to subdiffusion at $\langle\alpha\rangle \approx 0.75$ occurs over a lag time range from hundreds of ms to ~2 s, as investigated in other cell types in (11). At lag times of tens of seconds, a return to diffusive behavior is expected to occur, which is not investigated in this context.

Microtubule depolymerization

Benomyl-treated cells show a faster transition from diffusion to subdiffusion between $t = 100$ ms and $t = 750$ ms than WT cells. The mean value of α decreases from 1 to $\langle\alpha\rangle = 0.75$, as investigated in other cell types in (11). In WT cells, the latter value is approached not until a time lag of ~2 s. For large lag times, the WT and Benomyl-treated cells show similar $\langle\alpha\rangle$ values, indicating a vanishing

contribution of MT sweeping motion at large lag times. The effect of MT seems to be viscosifying, as indicated by consistently higher α values in the presence of MT. A possible explanation for the enhanced viscous properties is given by MT motion actively stirring the cytoplasm. The viscosifying effect is most pronounced at lag times between 0.5 and 1 s, in accordance with previous findings on MT sweeping motion, highlighting their pronounced motion and activity at lag times of ~1 s (37).

F-actin depolymerization

Latrunculin A-treated cells show a decrease in α from ~1 to 0.75 in the lag time range from 0.1 to 1.2 s, for shorter lag times than in the WT case and larger than in the Benomyl case. Actin-depleted cells show smaller $\langle\alpha\rangle$ values than WT cells. This leads us to conclude that F-actin exerts a viscosifying effect on the cytoskeleton, accounting for higher α values and apparently enhancing the motion of tracer particles, possibly by active driving forces generated by actin cortex rearrangements. At the same time, the diffusion coefficient is consistently smaller in the presence of F-actin, resulting from mostly lag time-independent hindrance of tracer particle motion, possibly in a cage-like fashion. Compared to WT cells, this might also indicate that MT motion is hindered by the presence of actin polymerization, as observed in neuronal growth cones (38).

CONCLUSION

We quantified the influence of MT and F-actin on subdiffusion in living cells and identified typical timescales. Our results clearly show that for a complete description of diffusive and subdiffusive motion phases in intracellular nanoscale transport, we have to consider both, the MSD exponent and the effective diffusion coefficient to understand cooperative and counterbalancing effects of MT and F-actin dynamics. We applied a local MSD analysis to distinguish ballistic from diffusive intracellular motion states, as extracted from NP traces and focused purely on subdiffusive motion states.

Our study revealed that subdiffusive dynamics can be described by a Brownian motion with correlated Gaussian velocity fluctuations. Although the real increments of intracellular motion are Gaussian only to a certain approximation and although we did not incorporate higher order or nonlinear correlations in our model, we were able to reproduce the marginal distributions of local exponent and diffusion coefficient (resulting from the local MSD analysis). Our data-driven Gaussian model helped us to understand which aspects of the parameter distributions are intrinsic to the algorithm (typically, the width of distributions, which is mainly determined by the finite-sample noise) and which are characteristic of intracellular motion (e.g., the mean value of α). We showed that reasonable approximations, i.e., assuming Gaussian increment statistics and neglecting higher-order correlations, allowed for a great simplification. Our aim was not to find a minimal model here. We want to illustrate that for a variety of cytoskeletal states, the more complicated statistics of the local MSD algorithm could be understood as a consequence of the much simpler increment statistics of the random motion, so the second-order statistics of the increments and a Gaussian assumption (the simpler statistics) to a large extent explains the more complicated statistics of the local MSD algorithm (α and D distribution), which is not used as fitting statistics. However, it is worth pointing out that our data-driven model does not give a physical description of intracellular motility. Future modeling of subdiffusive intracellular motion (e.g., in the framework of active gel theory incorporating fluctuations) can nevertheless profit from our simplification because such modeling can be limited to capture the correct linear increment correlation—a task that is certainly more readily accomplished than matching in a model a specific local MSD statistics (joint and marginal distributions of α and D).

To summarize our results on intracellular motion, we found that i), microtubule sweeping liquefies the cytoplasm on all investigated timescales, ii), actin-microtubule cross talk generates a viscosifying effect at timescales larger than 0.2 s, and iii), the F-actin-induced decrease in effective diffusion coefficients occurs at all investigated timescales (50 ms–2.5 s). It is the interplay of these effects, at these particular timescales, which mediates viable transport in living cells. These timescales are of particular interest because they correspond to the typical durations of alternating ballistic and diffusive phases. In the absence of both, MT sweeping motion and actin cortex rearrangement, intracellular motion becomes more similar to Brownian motion, which is an indicator for the major influence of dynamic cytoskeleton components on subdiffusion.

Alternations between subdiffusive and ballistic phases occur when a particle reaches close proximity to a MT. Thus, motor-driven, directed long-distance transport along MT shuttles NPs across the cell, but remains ineffective without well-defined short-range subdiffusion for the binding to targets (24). This brings about major biological implications, mostly for transport-driven cellular processes, such as migration (14): Cellular movements build upon the reliable supply of essential signaling molecules. Actin polymerization-related proteins, most notably PIP3 (phosphatidylinositol (3,4,5)-trisphosphate) accumulate at the cell membrane and lead to enhanced local actin polymerization. In consequence, cell protrusions are generated for migration. This process was shown to be controlled by spatiotemporally controlled, external chemotactic stimuli (39). A detailed understanding of the role of subdiffusion for governing complex cellular functions might promote a wide range of applications, aiming at externally controlling cell functions. This could be accomplished by means of NPs, carrying stimulus drugs, which are then inserted into living cells to controllably induce cell functions, for example directed migration.

D.H. acknowledges funding by the Deutsche Forschungsgemeinschaft (fund HE5958/2-1). Furthermore, we thank G. Gerisch (Max Planck Institute for Biochemistry in Martinsried, Germany) for the provision of the cell cultures.

REFERENCES

1. Sasaki, S., and M. Iwata. 1996. Impairment of fast axonal transport in the proximal axons of anterior horn neurons in amyotrophic lateral sclerosis. *Neurology.* 47:535–540.
2. Williamson, T. L., and D. W. Cleveland. 1999. Slowing of axonal transport is a very early event in the toxicity of ALS-linked SOD1 mutants to motor neurons. *Nat. Neurosci.* 2:50–56.
3. Hafezparast, M., R. Klocke, …, E. M. Fisher. 2003. Mutations in dynein link motor neuron degeneration to defects in retrograde transport. *Science.* 300:808–812.
4. Trushina, E., R. B. Dyer, …, C. T. McMurray. 2004. Mutant huntingtin impairs axonal trafficking in mammalian neurons in vivo and in vitro. *Mol. Cell. Biol.* 24:8195–8209.
5. Parent, C. A., and P. N. Devreotes. 1999. A cell's sense of direction. *Science.* 284:765–770.
6. Insall, R., A. Müller-Taubenberger, …, G. Gerisch. 2001. Dynamics of the *Dictyostelium* Arp2/3 complex in endocytosis, cytokinesis, and chemotaxis. *Cell Motil. Cytoskeleton.* 50:115–128.
7. Konopka, C. A., J. B. Schleede, …, S. Y. Bednarek. 2006. Dynamin and cytokinesis. *Traffic.* 7:239–247.
8. Fletcher, D. A., and R. D. Mullins. 2010. Cell mechanics and the cytoskeleton. *Nature.* 463:485–492.
9. Caspi, A., R. Granek, and M. Elbaum. 2000. Enhanced diffusion in active intracellular transport. *Phys. Rev. Lett.* 85:5655–5658.
10. Loverdo, C., O. Bénichou, …, R. Voituriez. 2008. Enhanced reaction kinetics in biological cells. *Nat. Phys.* 4:134–137.
11. Caspi, A., R. Granek, and M. Elbaum. 2002. Diffusion and directed motion in cellular transport. *Phys. Rev. E.* 66:011916–011927.
12. Hänggi, P., and F. Marchesoni. 2009. Artificial Brownian motors: controlling transport on the nanoscale. *Rev. Mod. Phys.* 81:387–442.
13. Trepat, X., G. Lenormand, and J. J. Fredberg. 2008. Universality in cell mechanics. *Soft Matter.* 4:1750–1759.
14. Weiss, M., M. Elsner, …, T. Nilsson. 2004. Anomalous subdiffusion is a measure for cytoplasmic crowding in living cells. *Biophys. J.* 87:3518–3524.
15. Kammerer, A., F. Höfling, and T. Franosch. 2008. Cluster-resolved dynamic scaling theory and universal corrections for transport on percolating systems. *Europhys. Lett.* 84:66002.
16. Lenormand, G., J. Chopin, …, J. P. Butler. 2007. Directional memory and caged dynamics in cytoskeletal remodelling. *Biochem. Biophys. Res. Commun.* 360:797–801.
17. Weihs, D., T. G. Mason, and M. A. Teitell. 2007. Effects of cytoskeletal disruption on transport, structure, and rheology within mammalian cells. *Phys Fluids (1994).* 19:103102.
18. Robert, D., T.-H. Nguyen, …, C. Wilhelm. 2010. In vivo determination of fluctuating forces during endosome trafficking using a combination of active and passive microrheology. *PLoS ONE.* 5:e10046.
19. Weeks, E. R., and D. A. Weitz. 2002. Subdiffusion and the cage effect studied near the colloidal glass transition. *Chem. Phys.* 284:361–367.
20. Weeks, E. R., and D. A. Weitz. 2002. Properties of cage rearrangements observed near the colloidal glass transition. *Phys. Rev. Lett.* 89:095704.
21. Bursac, P., G. Lenormand, …, J. J. Fredberg. 2005. Cytoskeletal remodelling and slow dynamics in the living cell. *Nat. Mater.* 4:557–561.
22. Fabry, B., G. N. Maksym, …, J. J. Fredberg. 2001. Scaling the microrheology of living cells. *Phys. Rev. Lett.* 87:148102.
23. Alcaraz, J., L. Buscemi, …, D. Navajas. 2003. Microrheology of human lung epithelial cells measured by atomic force microscopy. *Biophys. J.* 84:2071–2079.
24. Brangwynne, C. P., G. H. Koenderink, …, D. A. Weitz. 2009. Intracellular transport by active diffusion. *Trends Cell Biol.* 19:423–427.
25. Fey, P., A. S. Kowal, …, R. L. Chisholm. 2007. Protocols for growth and development of *Dictyostelium discoideum. Nat. Protoc.* 2:1307–1316.
26. Prassler, J., A. Murr, …, G. Marriott. 1998. DdLIM is a cytoskeleton-associated protein involved in the protrusion of lamellipodia in *Dictyostelium. Mol. Biol. Cell.* 9:545–559.
27. Schilling, J., E. Sackmann, and A. R. Bausch. 2004. Digital imaging processing for biophysical applications. *Rev. Sci. Instrum.* 75:2822–2827.
28. Cox, D. R., and P. A. W. Lewis. 1966. The Statistical Analysis of Series of Events. Chapman and Hall, London.
29. Arcizet, D., B. Meier, …, D. Heinrich. 2008. Temporal analysis of active and passive transport in living cells. *Phys. Rev. Lett.* 101:248103.
30. Box, G. E. P., G. M. Jenkins, and G. C. Reinsel. 1994. Time Series Analysis: Forecasting and Control. Prentice-Hall, Upper Saddle River, NJ.
31. Weber, S. C., A. J. Spakowitz, and J. A. Theriot. 2010. Bacterial chromosomal loci move subdiffusively through a viscoelastic cytoplasm. *Phys. Rev. Lett.* 104:238102.
32. Mahowald, J., D. Arcizet, and D. Heinrich. 2009. Impact of external stimuli and cell micro-architecture on intracellular transport states. *ChemPhysChem.* 10:1559–1566.
33. Bursac, P., B. Fabry, …, S. S. An. 2007. Cytoskeleton dynamics: fluctuations within the network. *Biochem. Biophys. Res. Commun.* 355: 324–330.
34. Liu, J., M. L. Gardel, …, D. A. Weitz. 2006. Microrheology probes length scale dependent rheology. *Phys. Rev. Lett.* 96:118104.
35. Tolić-Nørrelykke, I. M., E. L. Munteanu, …, K. Berg-Sørensen. 2004. Anomalous diffusion in living yeast cells. *Phys. Rev. Lett.* 93:078102.
36. Gardel, M. L., M. T. Valentine, …, D. A. Weitz. 2003. Microrheology of entangled F-actin solutions. *Phys. Rev. Lett.* 91:158302.
37. Heinrich, D., and E. Sackmann. 2006. Active mechanical stabilization of the viscoplastic intracellular space of *Dictyostelia* cells by microtubule-actin crosstalk. *Acta Biomater.* 2:619–631.
38. Lowery, L. A., and D. Van Vactor. 2009. The trip of the tip: understanding the growth cone machinery. *Nat. Rev. Mol. Cell Biol.* 10:332–343.
39. Meier, B., A. Zielinski, …, D. Heinrich. 2011. Chemotactic cell trapping in controlled alternating gradient fields. *Proc. Natl. Acad. Sci. USA.* 108:11417–11422.

6 Conclusion and Outlook

The present thesis addresses the question of parallelization and miniaturization of protein interaction studies at the single–molecule and single–cell level. After introduction of the scientific context, three exemplary studies of interaction force measurements conducted in the context of this thesis were presented. Although different in methods employed and in systems studied, they consistently highlight the importance of gathering dynamic information about protein interactions and mechanics: In Chapter 3, a microfluidic workflow integrates on–chip protein synthesis with AFM force spectroscopy for determination of *molecular mechanics*. In Chapter 4, a microfluidic chip to probe protein–DNA interactions was introduced, characterized and applied to the proof–of–principle study of the DNA–binding of endonuclease EcoRI *binding mechanics*. In Chapter 5, the study of interactions between actin filaments and microtubules revealed the impact of cytoskeleton depolymerizing drugs on *cellular mechanics*.

To put it in a nutshell, three main conclusions can be drawn:

- Microfluidic chips can be employed to attain a gain in parallelization and sample–to–sample comparability for AFM–based Single–Molecule Force Spectroscopy (SMFS) studies. The chip enables a simple workflow from gene array to molecular mechanics, particularly destined for protein–protein studies.
- The Molecular Force Assay (MFA) can be transferred to a microfluidic format without loss in resolution or sensitivity. Its capabilities are expanded in terms of miniaturization and parallelization. It is ideally suited for the study of protein–DNA interactions.
- The viscoelastic properties of the living *Dictyostelium discoideum* cell are held in a precious balance by the presence of both microtubules and actin. The cellular mechanics can only be described by taking into account the interaction between these two types of cytoskeletal elements.

With respect to future investigations, a few routes are particularly promising and build upon the work presented in this thesis:

- Building on the microfluidic protein patterning for AFM–based single–molecule force spectroscopy, a rather slight and simple modification of the experimental design will allow for single–molecule cut–and–paste (SMC&P) of the expressed enzymes (*cf.* Figure 12). In the SMC&P method, a functionalized AFM cantilever and a three–fold rupture force hierarchy are used to transfer single molecules from a depot zone to a target zone at nanometer-resolution [2].
  With respect to the MITOMI chip design and the work presented in Chapter 3, it can be envisioned to co–express depot and transfer proteins in some chambers – the depot proteins featuring a ybbR tag for covalent immobilization and the transfer proteins featuring no ybbR tag but a low–force binding affinity to the depot protein. In the other chambers, target proteins are expressed and covalently immobilized by the ybbR tag. If the transfer proteins feature a medium–force binding affinity to the cantilever functionalization and a high–force binding affinity to the target proteins a force hierarchy can be designed. Possible implementations of this configuration include the use of cohesin proteins as depot and target and the use of dockerin proteins as transfer fused to a cellulolytic enzyme of interest. The transfer dockerin – target cohesin pair being a native fit, the use of

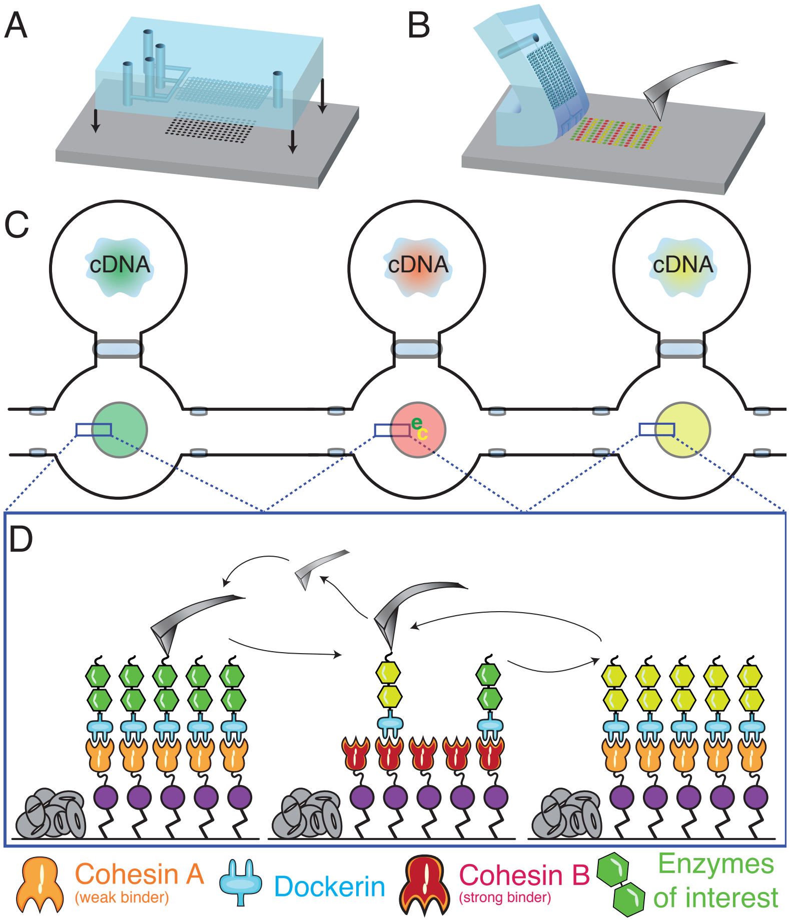

Figure 12: **On–chip SMC&P** of *in vitro* synthesized proteins: The presented microfluidic protein micro arraying for AFM SMFS is suited for application as AFM SMC&P depot and target zones. (A) and (B) show the macroscopic workflow from DNA microarraying (A) to AFM cantilever approach (B). (C) shows three adjacent chambers on the chip with spotted cDNA used to express three protein configurations (green, red, and yellow). The center chamber (red) serves as target zone for enzyme complexes (ec) to be assembled by on-chip SMC&P. (D) shows these three adjacent protein configurations with two depot zones (left and right) with weakly binding depot cohesins (orange) and enzymes to be transported (green and yellow), and a target zone (center) with strongly binding target cohesins (red).

an interspecies or mutated cohesin as depot protein for reduced binding force is promising. For the medium–force transfer handle, a short polypeptide tag of interest is GCN4(7P14P) [102], whose binding to a recombinant antibody single-chain Fv fragment is well–characterized [103] and has been applied to protein-based SMP&P [104]. This implementation will enable the heterogenic assembly (*e.g.* of enzyme complexes) from multiple depots, contrary to the current implementations, which draw on a single depot with a single type of molecule. Furthermore, the handling of proteins is facilitated by the use of cell–free gene expression. In combination with sophisticated and sensitive biomass degradation assays [105, 106], this might allow for screening for optimal enzymatic cocktails in next-generation biofuel production [107].

- The Molecular Force Assay (MFA) can be integrated with *in vitro* protein synthesis, as sketched in Figure 13. The *in vitro* protein synthesis capabilities of the utilized MITOMI chip design rest on the use of the expression chamber, which lay bare in the work presented in Chapter 4, but were exploited in the work presented in Chapter 3. The feasibility of combining the on–chip

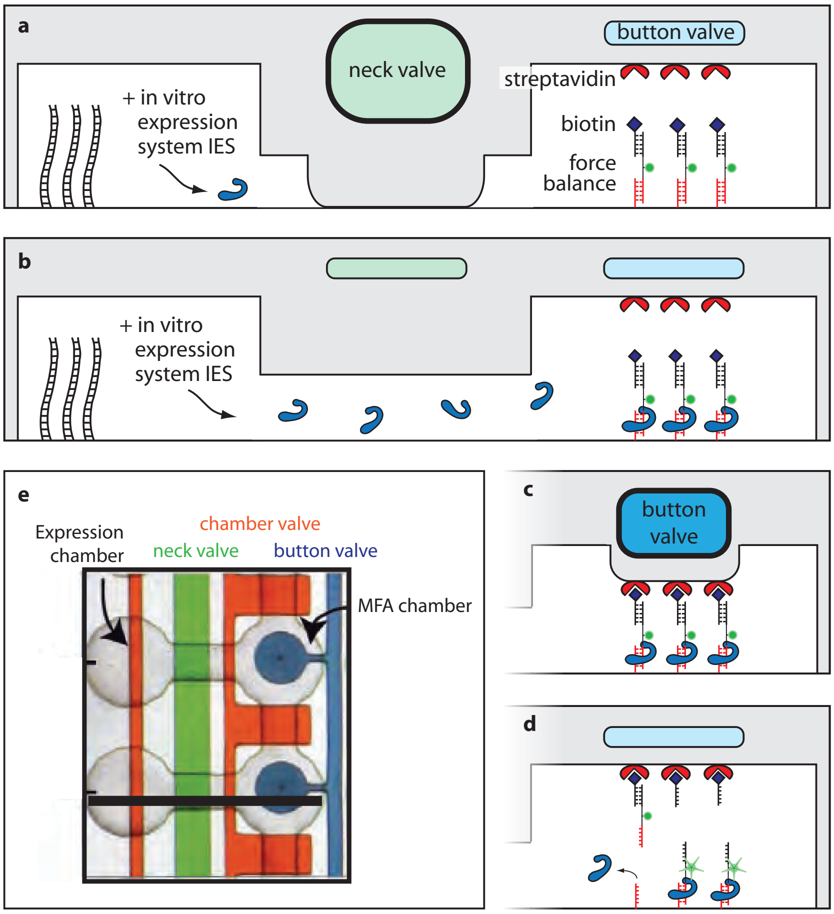

Figure 13: Extension of the on–chip MFA using cell–free gene synthesis: The multiplexing capabilities of the MFA can be expanded if the DNA–binding proteins of interest is synthesized in parallel and on–chip.

MFA with *in vitro* protein synthesis is thus founded. The gain in capabilities is noticeable: Rather than simple row–by–row multiplexing (of DNA recognition sequences or reference strands), a chamber–by–chamber multiplexing of DNA–binding protein is achievable. The use of cell–free protein synthesis kits facilitates the extension from bacterial to more complex, eucaryotic systems, such as *Drosophila melanogaster* extracts.
Further multiplexing capabilities are attainable if not only the cDNA for proteins of interest are spotted, but also the force probes. In this way, the on–chip MFA would arguably constitute the first truly high–throughput protein–DNA interaction force measurement method, where DNA recognition sequence, DNA–binding protein of interest, and reference and be tuned simultaneously. A highly promising field is the study of transcription factors.

- The study of macromolecular assemblies and cell mechanics has rapidly advanced further. In particular, force mapping sensors are constructed in sophisticated ways: with respect to cell–internal force mapping, Förster Resonance Energy Transfer (FRET) signals between two genetically encoded fluorescent proteins, separated by a force–sensitive spider silk protein domain, can switch upon force load [108]. With respect to membrane–level force mapping, mechano–sensitive transmembrane receptors (*e.g.* integrin) can pull apart defined dsDNA tethers in perfect analogy to MFA probes (*cf.* Chapter 4) upon receptor–ligand binding [109]. With respect to 3D tissue force mapping, confocal fluorescent imaging of oil microdroplets reveals their deformation and stresses

> exerted by the cells [110]. The MFA principle having recently been transferred to live–cell experiments [109, 111], and microfluidic chips being ideally suited for both live–cell culturing [89] and parallelized MFA (*cf.* Chapter 4), the combination of both promises to be a candidate for integrated and parallelized cell culturing and interaction force measurements in the future.

Thus, the findings presented in this thesis arguably show ways to transfer the detailed single-molecule and single-cell investigation of protein interactions onto a level of parallelization, which was not attainable thus far.

A Appendix

A.1 Technical information

A.1.1 Pneumatic setup and operation

The pneumatic setup is sketched in Figure 14. The pressure reservoir of choice is a bottle of compressed nitrogen ($V = 50\,l$ at $p = 200\,bar$), down–regulated manually to a pressure of 15 psi[1] (relative to ambient pressure) and connected to the inlet ports of solenoid valves, assembled in parallel on three 8-fold manifolds.

The solenoid valves can be switched between open and closed states: Upon application of electric current, the solenoid generates a magnetic field which moves a coaxially located core, used to make or break the gas seal. Upon release of the electric current, the core is replaced to its original position by springs.

The valves are built in a three–way architecture: If the valve is open, the pressure reservoir is connected to the outlet. If the valve is closed, the ambient port is connected to the outlet. The valves exist in normally open (N.O.) and in normally closed (N.C.) configurations, defined by their state in the absence of electric current. In the context of this thesis, both types were used to minimize long–term operation of solenoid valves: Control layer elastomeric valves which are typically pressurized (*i.e.* the flow layer inlet control valves) are connected to N.O. solenoid valves. Control layer elastomeric valves which are typically not pressurized and flow layer inlets are connected to N.C. solenoid valves. It is important to note that the state of solenoid valves and elastomeric valves is inversed: An *open* solenoid pressurizes and thereby *closes* an elastomeric valve!

One manifold is serving the Tygon tubing which is connected to flow layer inlets and thus requires an upstream pressure regulator adjusted to 4 psi. The other two manifolds serve the control layer inlets (one N.C., one N.O.). For a high–precision pressure control, rather than mere open/close actuation, the device of choice is an electrically controlled proportional pressure valve, which can be implemented upstream or downstream of the solenoid valves. For the work presented in Chapter 4, it was used to linearly pressurize the button membrane valve from 0 to 15 psi over time and was placed downstream of the corresponding solenoid valve.

The power supply to the solenoid valves is controlled *via* a custom–built unit, featuring a 24-bit USB controller. The USB controller is connected to the USB port of a control computer and actuated using LabView software. The USB controller including printed circuit board (PCB) design, amplifier circuitry and the USB–based input/output, has been described in high detail by Rafael Gómez-Sjöberg of Lawrence Berkeley National Laboratory [2]. The setup further comprises an imaging unit, which is described below, and hybrid DC/piezo sample positioning motors in x- and y-directions.

---

[1] Pounds per square inch, $1\,psi = 6.89 \cdot 10^{-2}\,bar$

[2] `https://sites.google.com/site/rafaelsmicrofluidicspage/`

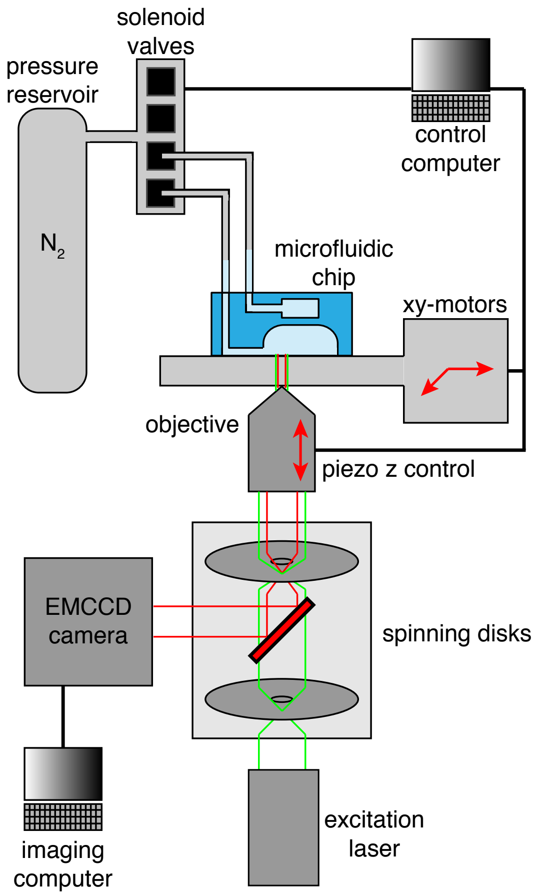

Figure 14: **The microfluidic setup** features electronically actuated solenoid valves, which pressurize microfluidic channels in the flow and control layers. The chip and sample are positioned using xy-motors and imaged through an inverted confocal spinning disk fluorescence microscopy setup. Adapted with kind permission from Ref. [112]

A.1.2 Liquid dispensing

Minituarization and parallelization of established laboratory methods, such as the microfluidic ones presented in Chapters 3 and 4 of this thesis, rely fundamentally on according sample preparation. For surface–bound methods, this requires precisely controlled surface deposition of small volume droplets of biosolutions, *e.g.* DNA.

One particularly promising and advantageous fluid microplotter method relies on ultrasonic excitation of a glass micropipette attached to a piezoelectric element [113]. This way, picoliter volumes of DNA solutions can be deposited. The micropipette is a tapered glass capillary with a tip diameter of $30\mu m$. It can be filled by simple fluid contact by the capillary effect. It is then excited at its resonant frequency, typically on the order of 500 kHz, to induce droplet formation and ideally contact–less droplet printing onto the surface. The tip and piezo are mounted on a motorized xyz-stage for accurate and reproducible positioning of sample spots. Ambient humidity can be held constant (*e.g.* at a level of 70%) for improved droplet formation and slowed down evaporation. The formed spots are on the order of $40\mu m$, depending on the wetting behavior between droplet and surface. In the work presented in Chapter 3, this size is a good compromise between both sufficient sample amount and sufficient miniaturization for fitting hundreds of spots into a chip, one spot per cDNA chamber.

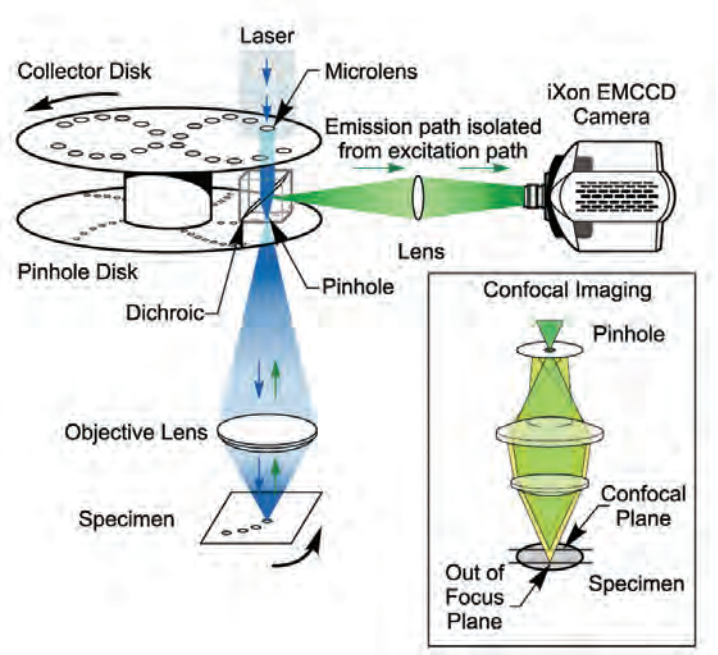

Figure 15: Confocal spinning disk microscopy takes advantage of the conventional pinhole–based exclusion of out–of–focus light, similar to laser scanning confocal imaging. As further refinement, it features an array of thousands of pinholes on a rotating disk for faster scanning and an additional microlens disk for minimized illumination losses: The majority of laser light intensity of an expanded beam is collected onto the pinholes. A dichroic mirror between the disks ensures that excitation light passes through both disks, whereas emission light only passes the pinhole disk and is then projected onto a camera for detection, in the present case a sensitive EMCCD device. Reproduced from Ref. [114]

A.1.3 Confocal fluorescence microscopy

Fluorescence imaging has advanced fundamental research in the life sciences tremendously. It relies on the red–shift of photons emitted upon previous photon absorption, similar to phosphorescence (the latter involving an additional inter–system crossing from singlet to triplet states). Some fluorophore molecules are particularly suited for efficient fluorescence imaging due to their high conversion rates and quantum efficiencies.

Confocal fluorescence imaging permits the selective imaging of optical sections. In conventional confocal laser scanning microscopy, a pinhole is used to exclude out–of–focus light, but images can only be acquired pixel–by–pixel by scanning the desired field of view. As a consequence, image acquisition is lengthy and an undesired time shift between the first and last pixels of the same image is introduced.

In particular for bioimaging purposes, a fast acquisition rate is desired. To achieve this, the concept of confocal *spinning disk* microscopy was introduced: As shown in Figure 15, instead of a single pinhole, thousands of pinholes are assembled on a disk and the laser beam is expanded in diameter to illuminate a portion of the disk, rather than a single pinhole. By spinning the disk in the primary image plane of the microscope, the image is scanned. Both excitation and emission light passes through these pinholes.

Yet, this setup lacks high–rate image acquisition: the laser intensity at the specimen is greatly reduced by two orders of magnitude, because most of the incoming laser light does not go through any pinhole. Therefore, another disk, the microlens disk, is introduced: It spins co–axially and in phase with the pinhole disk and the lenses are placed in a way to focus 60% of the incoming light through pinholes. These two parallel spinning disks thus achieve video–rate imaging with multiple scans of each pixel in the image. Typical spinning rates are 1500-5000 rpm, while the disks feature 12 identical pinhole or lens sectors with a total number of 20 000 pinholes , each $50\mu m$ in size. In addition, a dichroic mirror is placed between the two disks: This way, the emission light is reflected to the camera without being re–expanded by the microlenses. Typically, a sensitive EMCCD camera (Quantum efficiency of 90%) is used for fast–rate acquisition.

A.1.4 *in vitro* expression

Gene expression refers to the synthesis of proteins from a DNA template. With this terminology, the synthesis of functional, non–coding RNA such as ribosomal RNA (rRNA), small nuclear RNA (snRNA) or microRNA (miRNA) is excluded, although of great interest. The underlying mechanism of gene expression is similar for both procaryotes and eucaryotes and can be essentially divided in two consecutive parts (Fig. 16): transcription synthesizes RNA from a DNA template by complementarity and translation synthesizes proteins from this messenger RNA. In eucaryotes, the RNA transcript is typically capped at the 5’ end, polyadenylated at the 3’ end and spliced [3] before export from the nucleus and translation. In procaryotes, these steps are absent.

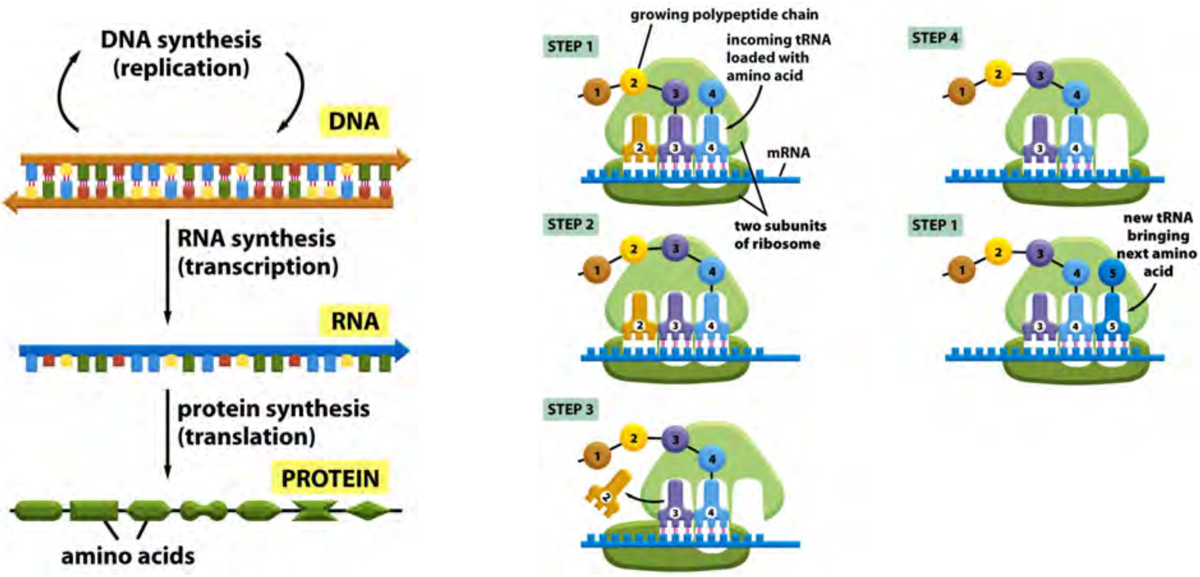

(a) Protein expression **(b)** Translation

Figure 16: **(a) Protein expression** consists of a two–step process, the RNA synthesis from a DNA template and the protein synthesis from RNA. **(b) Translation**, the synthesis of protein from RNA is carried out by the ribosome, a macromolecular assembly in a well–organized series of steps. Reproduced from Ref. [115]. ©Garland Science 2008.

Transcription is carried out by RNA polymerase enzymes, including the DNA helix unwinding, complementary base–pairing, polymerization and movement along the dsDNA from 5’ to 3’ ends. In bacteria, it is initiated by the formation of an energetically favorable complex with the σ factor at characteristic promoter regions upstream of the gene of interest. In the context of this thesis, the T7 promoter (`TAATACGACTCACTATAGGGAGA`) and the corresponding RNA polymerase from the T7 bacteriophage were used. The transcription initiation in eucaryotes is more intricate [115].

Translation is carried out by ribosomes, which are large, sensitive macromolecular assemblies (2.5 MDa in size in procaryotes) of both RNA and proteins. A ribosome consists of a smaller subunit for reading mRNA information and a larger subunit for formation of according polypeptide chains. mRNA information is read in three–letter codons, each corresponding to one amino acid and decoded by tRNA molecules, which are equipped with the corresponding amino acid by tRNA synthetases. The polypeptide chain producing subunit of the ribosome assembles these amino acids into a protein primary struc-

---

[3] removal of non–coding intron sequences

ture from N to C termini, starting at ribosome–binding sites (RBS) and halting at stop codons on the mRNA. The protein can then fold into higher–order structures.

This short introduction highlights the complexity of carrying out gene expression *in vitro*. These cell–free systems have attracted wide attention and are increasingly well characterized [99]. In the context of this thesis, an S30 extract from *e. coli* was used [116]. The corresponding *e. coli* strain B is deficient in OmpT endoproteinase and Lon protease for improved protein stability. The extract is designed to work with the exogenous phage T7 promoter. Furthermore, a mixture of amino acids, rNTPs, tRNAs, IPTG [4], an ATP–regenerating system and various salts, are added to the extract. Adding additional T7 RNA polymerase and nuclease inhibitors improve protein yield. Although the microfluidic chip is not nuclease–free by design, all other reagents are nuclease–free. Protein yield can be influenced by a vast number of factors: gene context, size, relative position to the RBS, terminal untranslated regions (UTR), fusion tags, codon usage[5], and structure and stability of mRNA. A step–by–step preparation protocol for a non–commercial S30 T7 cell–free protein expression system is provided by the European Molecular Biology Laboratory [6].

This extract and protein synthesis mix is of prokaryotic origin. Nevertheless, eucaryotic extracts and lysates do exist, for example from wheat germ or rabbit reticulocyte. These eucaryotic extracts are often designed for translation (from mRNA to protein) only, and coupled *in vitro* with a (prokaryotic) phage RNA polymerase.

A.1.5 ybbR tag – CoenzymeA pull–down chemistry

Force spectroscopy experiments require specific immobilization of the molecules of interest to control the pulling geometry. Furthermore, the immobilization must withstand high forces, at least higher than the weakest link in the pulling geometry. Established immobilization chemistry includes NiNTA:Histidine, biotin:avidin, or maleimide:thiol [7]. Out of these three, only maleimide:thiol is covalent with its carbon–sulfur bond. One must bear in mind, that maleimide ($C_4H_3NO_2$) is prone to hydrolysis. In the context of this thesis, a recently introduced [98] method was chosen for covalent immobilization of *in vitro* synthesized proteins, known as ybbR tag / CoenzymeA chemistry.

The ybbR tag consists of a 11-residue polypeptide (`DSLEFIASKLA`), which can be genetically encoded flanking any gene of interest. In the presence of Sfp phosphopantetheinyl transferase (Sfp), a covalent bond between the serine residue at position 2 of the ybbR tag and the 4'-phosphopantetheinyl group of CoenzymeA is catalyzed. (*cf.* Figure 17).

CoenzymeA (CoA) is a coenzyme involved in the citric acid cycle of aerobic energy generation and essentially consists of an adenosine diphosphate (ADP) nucleotide, pantothenic acid (vitamin B5) and the amino acid cysteine (with slight modifications upon linkage). Thus, in the context of ybbR tag chemistry, CoA can at the same time be linked to a maleimide (and thereby to a polyethylene glycol linker) *via* disulfide bond on the thiol (SH) group of its cysteine subunit.

---

[4] Isopropyl-β-D-thiogalactopyranosid, an inducer for various promoters, including *lac* and T7

[5] In the context of this thesis, codons were typically optimized for *e. coli*.

[6] `http://www.embl.de/pepcore/pepcore_services/protein_expression/ecoli/lysate/index.html`

[7] The thiol group being for example on native or introduced cysteine residues.

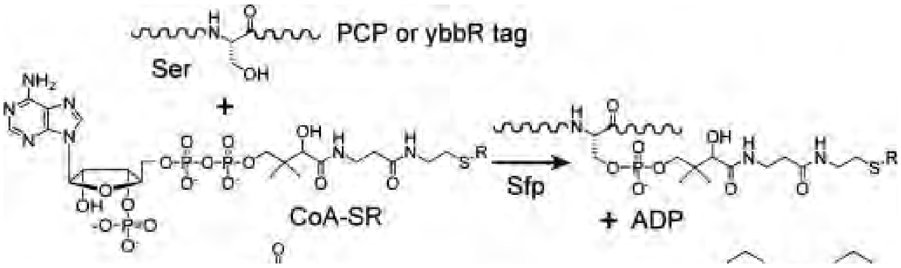

Figure 17: **ybbR tag and CoenzymeA** can be covalently linked by enzymatic catalysis by Sfp. Reproduced from Ref. [98]

.

A.1.6 Bell–Evans model

A model theory to predict and describe the dissociation of molecular bonds under force application used in the context of this thesis is the Bell–Evans model [117]. Figure 18 sketches its key assumptions: A bound state ($x = a$) and a dissociated state ($x \rightarrow \infty$) are separated by a barrier in free energy. The barrier is described by its height ΔG and the potential well width Δx. Association and dissociation are thermally driven at rates k_{on} and k_{off}. Application of force lowers the potential landscape linearly as a function of force F and distance from the bound state $(x - a)$.

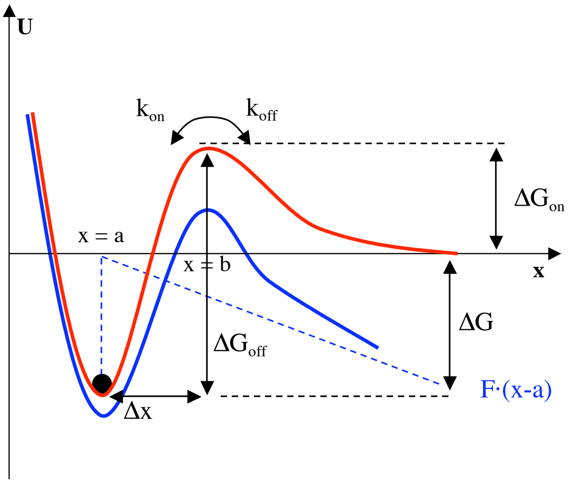

Figure 18: **Bell–Evans model:** A free energy landscape (red) describes the thermal association and dissociation of molecular bonds in a simple two–state model under the application of force (blue). Reproduced from Ref. [118]

.

Building on the Van't–Hoff–Arrhenius law, the dissociation rate is then force–dependent:

$$k_{off}(F) = k_{off}^{F=0} \cdot exp\left(\frac{F \cdot \Delta x}{k_B T}\right)$$

The number of bound complexes N decreases at rate k_{off} and is thus given as the solution to the differential equation:

$$\frac{dN}{dt} = -k_{off}(t) \cdot N$$

And the bond dissociation probability distribution is then given as the the force derivative of the number of unbound complexes: $p = \frac{d(N_{total}-N)}{dF} = -\frac{dN}{dF}$. This gives, as function of applied force F and force loading rate $F' = \frac{dF}{dt}$:

$$p(F,F') = \frac{k_{off}^{F=0}}{F'} \cdot exp\left(\frac{f \cdot \Delta x}{k_B T}\right) \cdot exp\left(-\frac{k_{off}^{F=0}}{F'} \cdot \int_0^F exp\left(\frac{f \cdot \Delta x}{k_B T}\right) df\right)$$

From this expression, the most probable rupture force can be determined (by differentiation $\frac{d}{dF}p(F,F') = 0$), which is used in SMFS experiments similar to those presented in Chapter 3, to determine energy landscape characteristics (k_{off} and Δx) from loading rate dependencies.

For the case of the bond of interest being a DNA duplex, the logarithmic off rate $\log_{10}(k_{off})$ and the potential well width Δx are assumed to be linear functions of oligomer length n, as used in Chapter 4:

$$k_{off} = 10^{\alpha-\beta\cdot n} s^{-1}$$

$$\Delta x = (t + n \cdot m)$$

A.2 Supplementary information to associated manuscript M1

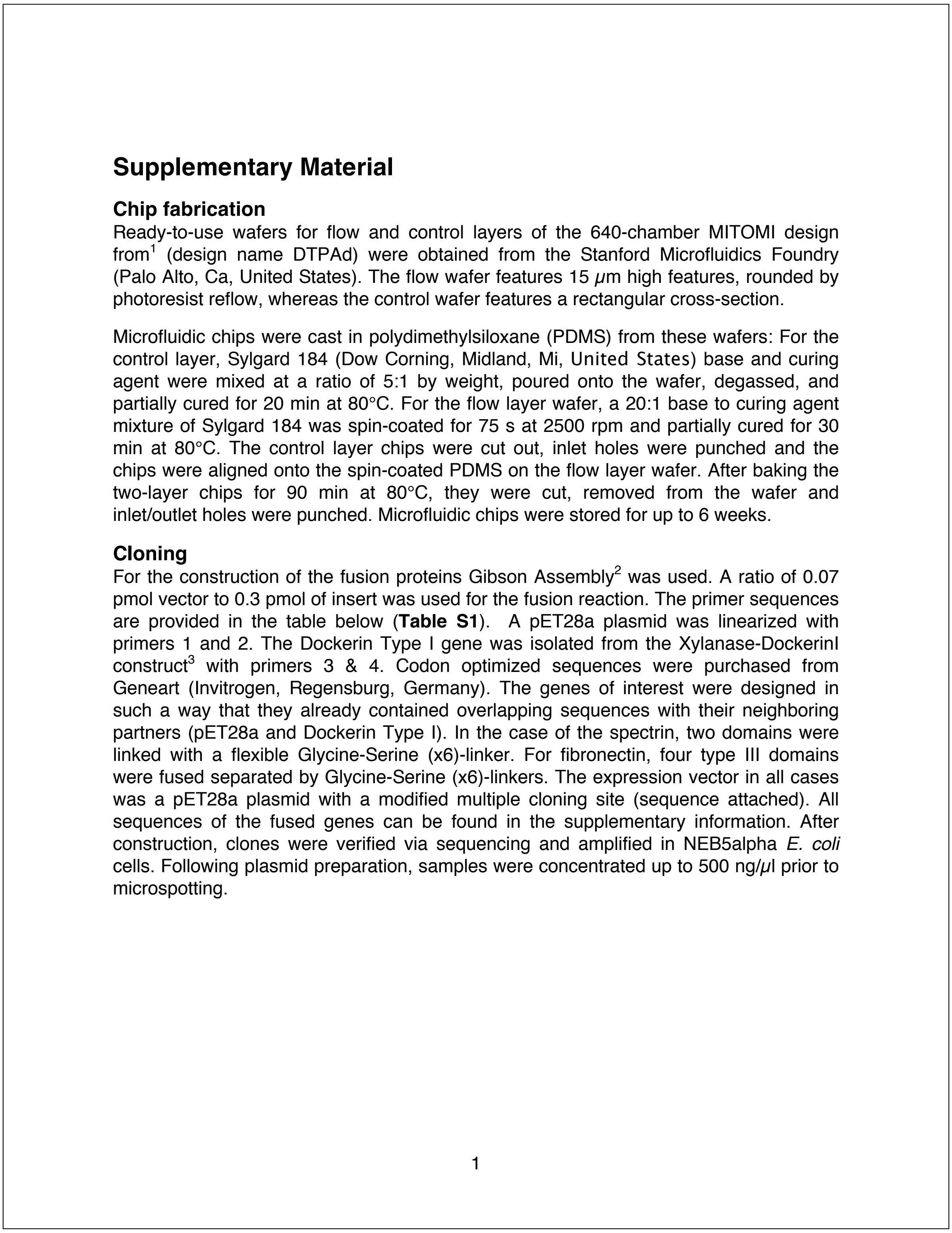

Supplementary Material

Chip fabrication

Ready-to-use wafers for flow and control layers of the 640-chamber MITOMI design from[1] (design name DTPAd) were obtained from the Stanford Microfluidics Foundry (Palo Alto, Ca, United States). The flow wafer features 15 μm high features, rounded by photoresist reflow, whereas the control wafer features a rectangular cross-section.

Microfluidic chips were cast in polydimethylsiloxane (PDMS) from these wafers: For the control layer, Sylgard 184 (Dow Corning, Midland, Mi, United States) base and curing agent were mixed at a ratio of 5:1 by weight, poured onto the wafer, degassed, and partially cured for 20 min at 80°C. For the flow layer wafer, a 20:1 base to curing agent mixture of Sylgard 184 was spin-coated for 75 s at 2500 rpm and partially cured for 30 min at 80°C. The control layer chips were cut out, inlet holes were punched and the chips were aligned onto the spin-coated PDMS on the flow layer wafer. After baking the two-layer chips for 90 min at 80°C, they were cut, removed from the wafer and inlet/outlet holes were punched. Microfluidic chips were stored for up to 6 weeks.

Cloning

For the construction of the fusion proteins Gibson Assembly[2] was used. A ratio of 0.07 pmol vector to 0.3 pmol of insert was used for the fusion reaction. The primer sequences are provided in the table below (**Table S1**). A pET28a plasmid was linearized with primers 1 and 2. The Dockerin Type I gene was isolated from the Xylanase-DockerinI construct[3] with primers 3 & 4. Codon optimized sequences were purchased from Geneart (Invitrogen, Regensburg, Germany). The genes of interest were designed in such a way that they already contained overlapping sequences with their neighboring partners (pET28a and Dockerin Type I). In the case of the spectrin, two domains were linked with a flexible Glycine-Serine (x6)-linker. For fibronectin, four type III domains were fused separated by Glycine-Serine (x6)-linkers. The expression vector in all cases was a pET28a plasmid with a modified multiple cloning site (sequence attached). All sequences of the fused genes can be found in the supplementary information. After construction, clones were verified via sequencing and amplified in NEB5alpha *E. coli* cells. Following plasmid preparation, samples were concentrated up to 500 ng/μl prior to microspotting.

	Name	Sequence
1	FW-w/o C-Tags MCS	TAACTCGAGTAAGATCCGGCTGC
2	REV-N-Tags MCS	GCTAGCACTAGTCCATGGGTG
3	FW-DocI GA	AAAGTGGTACCTGGTACTCC
4	REV-XylDocI-GA	CGGATCTTACTCGAGTTAGTTCTTGTACGGCAATGTATC
5	FW 10FNIII GA	CGCACCGGCTCTGGCTCTGGCTCTGTTAGTGATGTTCCGCGTG
6	REV 10 FNIII GA	GGAGTACCAGGTACCACTTTGGTGCG
7	REV 10FNIII (auf GS Li) GA	ACTAACAGAGCCAGAGCCAGAGCCGGTGCGATAATTGATTGAAATC
8	FW sfGFP (auf MCS) GA	CACCCATGGACTAGTGCTAGCAGCAAAGGTGAAGAACTGTTTAC
9	REV sfGFP (auf DocI) GA	GGAGTACCAGGTACCACTTTCTTATACAGCTCATCCATACCATG

Table S1: Overview of primers

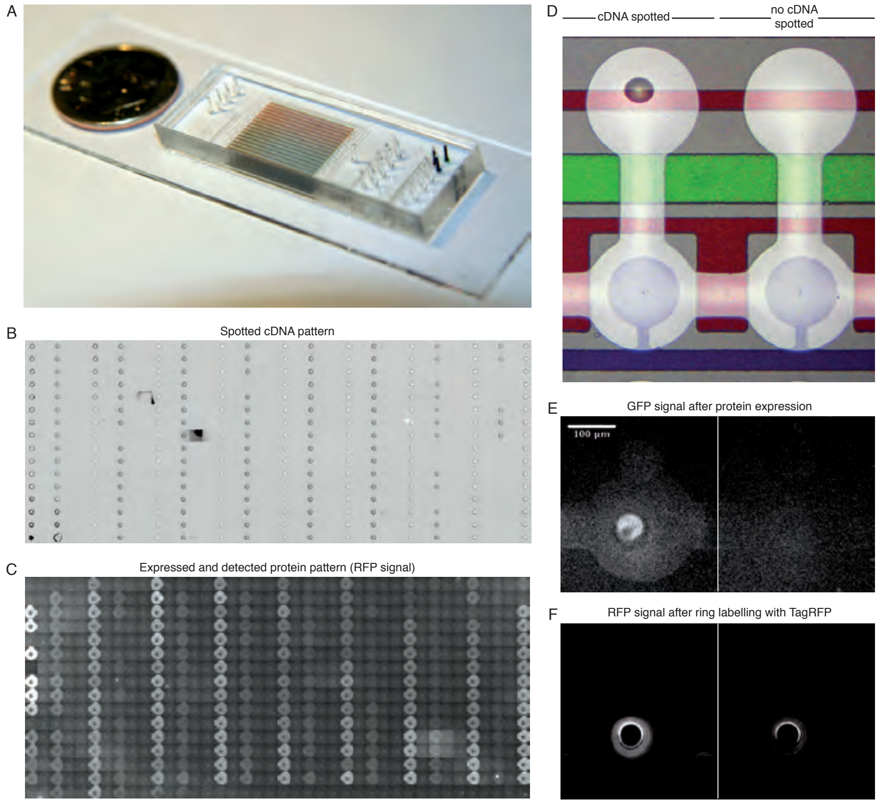

Figure S1. (A) Photograph of a microfluidic chip bonded to a glass slide with a US quarter coin for size comparison. Control channels are filled with food dye for better visualization. (B) Collage assembled from 640 single micrographs according to chip layout shows cDNA pattern after spotting (assembly not to scale). (C) A typical fluorescence collage assembled from 640 single fluorescence micrographs shows pattern of expressed protein (assembly not to scale). Fluorescence signal of TagRFP reveals expression levels and dockerin specificity. Here, low passivation of the protein chamber facilitates visualization. (D) Two of 640 adjacent dumbbell-shaped chambers, one with cDNA spotted (left) and one negative control without cDNA (right). Control channels are visualized with food dye: neck valve (green), sandwich valve (red), and button valve (blue). (E) Fluorescence images showing GFP signal from immobilized ybbR-GFP-dockerin (left) with negative control lacking the spotted cDNA (right). (F) RFP-cohesin staining of an outer concentric ring of the immobilized ybbR-GFP-dockerin (left), with the corresponding negative control (right).

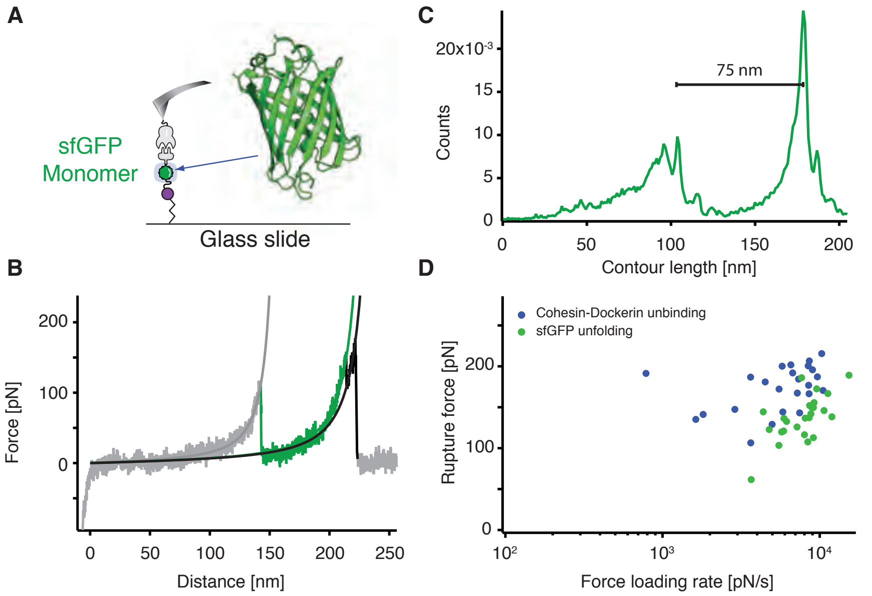

Figure S2. Force spectroscopy data for the superfolder GFP. (A) Schematic of on-chip pulling experiment with crystal structure. (B) Single-molecule unfolding trace with worm-like chain fits. (C) Contour length histogram (n=25) for GFP unfolding. (D) Scatter plot of rupture force vs. force loading rate for GFP unfolding and cohesin-dockerin complex rupture.

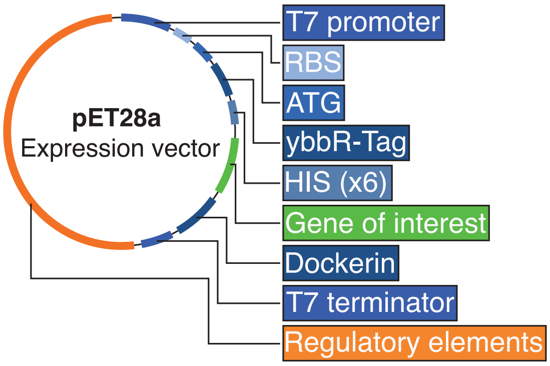

Figure S3. Diagram of the expression vector pET28a with an individual gene of interest.

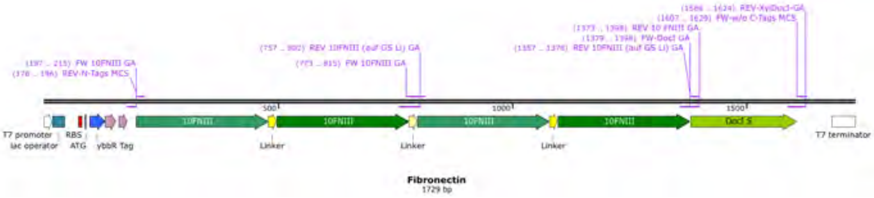

Figure S4. Schematic of fibronectin tetramer gene cassette.

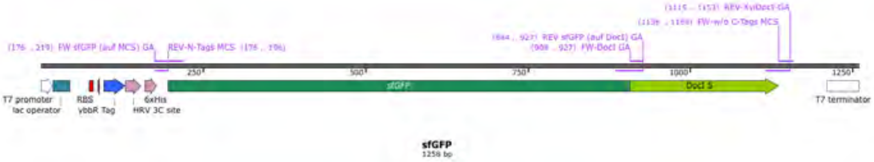

Figure S5. Schematic of sfGFP gene cassette.

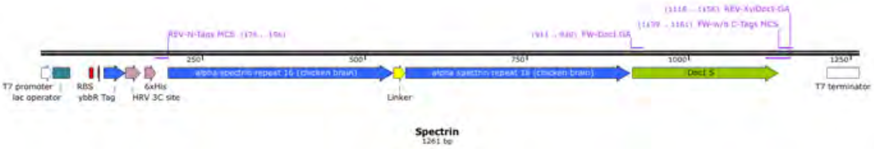

Figure S6. Schematic of spectrin dimer gene cassette.

Figure S7. Schematic of xylanase gene cassette.

DNA microspotting

A 24x60mm #1 thickness coverslip (Plano, Wetzlar, Germany) was silanized with 3-Aminopropyldimethyl-ethoxysilane (ABCR, Karlsruhe, Germany) following literature protocols[4].

The DNA solution containing 1% nuclease-free Bovine Serum Albumin (BSA, Carl Roth, Karlsruhe, Germany) in nuclease-free water, was micro-spotted under humid atmosphere onto the silanized coverslip using the GIX Microplotter II (Sonoplot, Middleton, Wi, United States) and a glass capillary (30 μm tip diameter, World Precision Instruments, Sarasota, Fl, United States) according to the manufacturer's instructions in a rectangular 40x16 pattern with 320 μm column pitch and 678 μm row pitch. Alignment of the cDNA array and the microfluidic chip was done manually using a stereo microscope. Bonding between the glass cover slip and microfluidic device was achieved by thermal bonding for 5 h at 80°C on a hot plate.

Device operation

The microfluidic device was operated at a pressure of 4 psi in the flow layer and 15 psi in the control layer. Operation started with the button and neck valves actuated for surface passivation. The flow layer was passivated by flushing with standard buffer (25 mM TRIS, 75 mM NaCl, 1 mM $CaCl_2$, pH 7.2) for 5 min and 2% BSA (in PBS) for 60 min.

S30 T7 HY (Promega, Madison, Wi, United States) in vitro transcription and translation mix, supplemented with 1 μL T7 polymerase (Promega) and 0.5 μL RNase inhibitor (invitrogen, Carlsbad, Ca, United States) was then flushed into the chip, filling the DNA chambers (neck valve open). The neck valve was then closed and the chip flushed with borate buffer (50 mM sodium borate, pH 8.5) for 5 min to remove expression mix from the front chambers. Next the button valve was opened, and the borate buffer was flushed for 30 min to thoroughly deprotonate aminosilane groups on the glass surface.

For maleimide / Coenzyme A functionalization, a solution of 5mM NHS-PEG-Maleimide (M_W 513 Da, Thermo-Scientific, Rockford, Il, United States) in borate buffer was flushed for 45 min. The device was then rinsed with nuclease-free H_2O for 2 min, followed by 30 min of 20 mM Coenzyme A (Merck, Darmstadt, Germany) in coupling buffer (50 mM sodium phosphate pH 7.2, 50 mM NaCl, 10 mM EDTA), and 5 min of rinsing with standard buffer.

The button valve was then actuated, and the channels filled with Sfp phosphopantetheinyl transferase in Sfp buffer (50 mM HEPES, 10 mM $MgCl_2$). The neck valves were then opened and the sandwich valves closed to avoid chamber-to-chamber cross-contamination. The chip was incubated at 37°C for 2.5 h on a hot plate. After the first 1 h of incubation, the button valve was opened to allow linkage of expressed protein onto the Coenzyme A – functionalized area below the button. After incubation, the neck and button valves were closed, the sandwich valve was opened and the chip was flushed with standard buffer for 20 min.

To check for successful in vitro transcription and translation, fluorescence detection was used. The detection solution consisting of TagRFP-Cohesin Type 1 (2 μg/ml) in standard buffer was flushed through the device for 5 min with the button valve actuated. The sandwich valves were then actuated, and the button valve partially released by decreasing the pressure to 13 psi. After an incubation of 20 min, the button valve was fully actuated (15 psi), the sandwich valves opened, and the chip flushed with standard buffer for 20 min. Fluorescence images of all chambers were recorded on an inverted microscope with a 10x objective (Carl Zeiss, Jena, Germany), featuring an EMCCD Camera (Andor, Belfast, United Kingdom). Prior to force spectroscopy experiments, the chip was stored at 4°C under humid atmosphere for up to 24 h.

Cantilever Functionalization

A silicon-nitride cantilever bearing a silicon tip with a tip radius of ~10 nm (Biolever mini, Olympus) was silanized with 3-aminopropyl-dimethyl-ethoxysilane (ABCR, Karlsruhe, Germany) as described previously[4]. The protein functionalization was performed in a similar way as reported previously[5]. Briefly, a 50 μM solution of A2C CBM-Cohesin from *Clostridium thermocellum* in standard buffer was incubated with 1:2 (v/v) TCEP beads (Tris (2-carboxyethyl) phosphine disulfide reducing gel, Thermo Scientific, Rockford, IL, United States), previously washed with standard buffer, for 2.5 h. The cantilever was soaked in borate buffer for 45 min to deprotonate primary amine groups on the silanized surface, then incubated with 20mM NHS-PEG-Maleimide (M_W 5 kDa, Thermo Scientific, Rockford, Il, United States) in borate buffer for 60 min.

The cantilever was rinsed in three sequential beakers of deionized H_2O. TCEP beads were separated from the protein solution by centrifugation at 1 krpm for 1 min. Next the cantilever was incubated for 60 min with reduced protein solution, mixed 3:1 (v/v) with standard buffer. The cantilever was then rinsed in three sequential beakers of standard buffer and stored submerged in standard buffer in humid atmosphere at 4°C for up to 24 h prior to use.

Force Spectroscopy

For the force spectroscopy measurements, a custom-built TIRF (total internal reflection fluorescence) - AFM (atomic force microscope) hybrid[6] was used. The TIRF microscope was used to image fluorophores in up to three different color channels simultaneously using an ‘iChrome MLE-S’ 4-colour laser (Toptica Photonics AG, Gräfelfing, Germany), an ‘Optosplit III’ triple emission image splitter (Cairn Research Ltd., Kent, United Kindom) and a ‘Xion3’ EMCCD camera (Andor, Belfast, United Kingdom). A long-range xy piezo nano-positioning system (ANC350, Attocube Systems AG, Munich, Germany) allowed access to the whole microchip array as well as fine spatial sampling of different surface molecules separated from one another on the nanometer scale within each protein spot. Cantilever actuation in the z-direction was performed by a ‘LISA’ piezo-actuator (Physik Instrumente GmbH & Co. KG, Karlsruhe/Palmbach, Germany) driven by a ‘MFP3D’ AFM controller (Asylum Research, Santa Barbara, CA, United States).

The same force spectroscopy protocol was performed repeatedly in each functionalized protein target area, and consisted of a cantilever approach velocity of 3000nm/s, a dwell time at the surface of 10ms, and a retract velocity of 800nm/s. Data were recorded at a

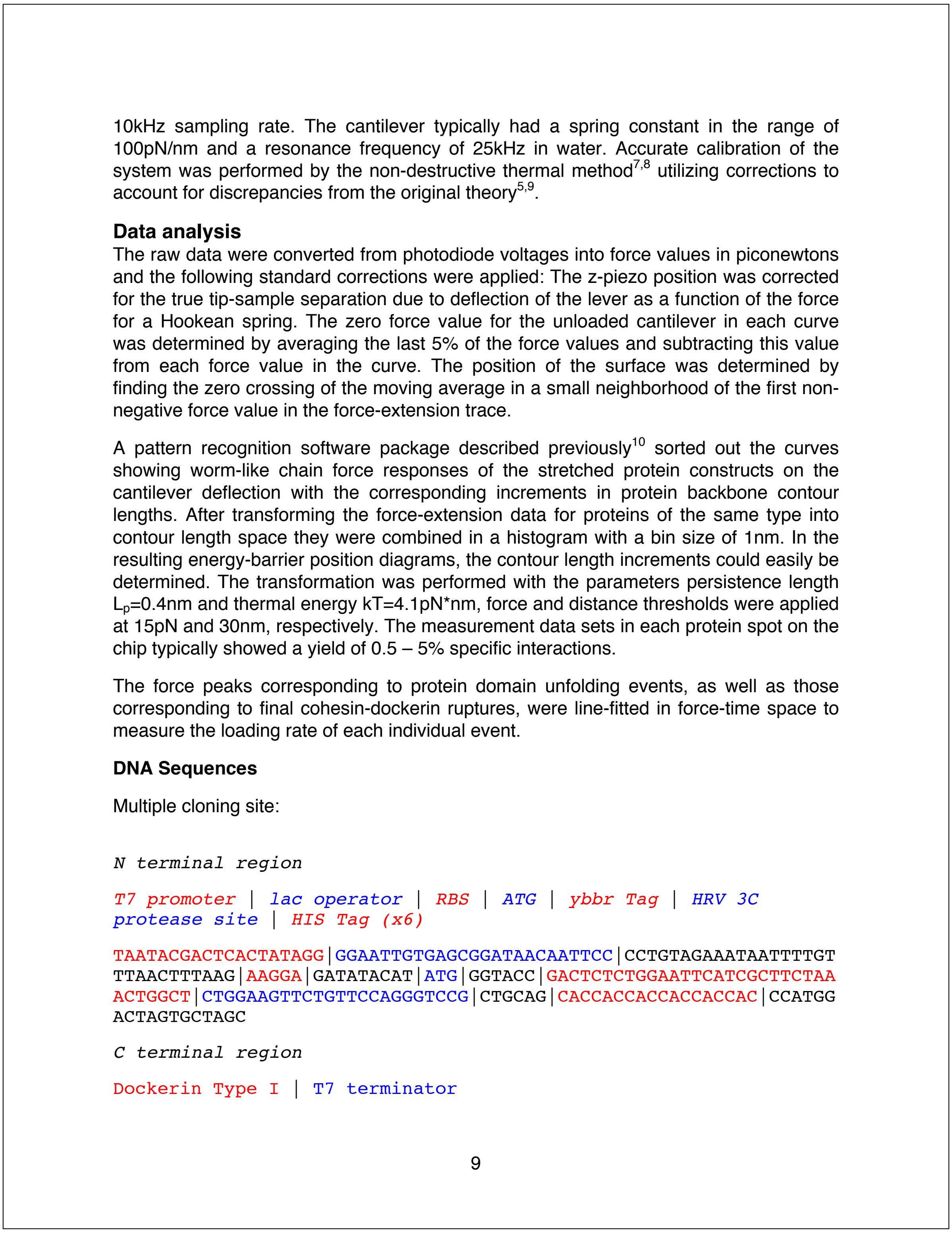

10kHz sampling rate. The cantilever typically had a spring constant in the range of 100pN/nm and a resonance frequency of 25kHz in water. Accurate calibration of the system was performed by the non-destructive thermal method[7,8] utilizing corrections to account for discrepancies from the original theory[5,9].

Data analysis

The raw data were converted from photodiode voltages into force values in piconewtons and the following standard corrections were applied: The z-piezo position was corrected for the true tip-sample separation due to deflection of the lever as a function of the force for a Hookean spring. The zero force value for the unloaded cantilever in each curve was determined by averaging the last 5% of the force values and subtracting this value from each force value in the curve. The position of the surface was determined by finding the zero crossing of the moving average in a small neighborhood of the first non-negative force value in the force-extension trace.

A pattern recognition software package described previously[10] sorted out the curves showing worm-like chain force responses of the stretched protein constructs on the cantilever deflection with the corresponding increments in protein backbone contour lengths. After transforming the force-extension data for proteins of the same type into contour length space they were combined in a histogram with a bin size of 1nm. In the resulting energy-barrier position diagrams, the contour length increments could easily be determined. The transformation was performed with the parameters persistence length L_p=0.4nm and thermal energy kT=4.1pN*nm, force and distance thresholds were applied at 15pN and 30nm, respectively. The measurement data sets in each protein spot on the chip typically showed a yield of 0.5 – 5% specific interactions.

The force peaks corresponding to protein domain unfolding events, as well as those corresponding to final cohesin-dockerin ruptures, were line-fitted in force-time space to measure the loading rate of each individual event.

DNA Sequences

Multiple cloning site:

N terminal region

T7 promoter | lac operator | RBS | ATG | ybbr Tag | HRV 3C protease site | HIS Tag (x6)

TAATACGACTCACTATAGG|GGAATTGTGAGCGGATAACAATTCC|CCTGTAGAAATAATTTTGT TTAACTTTAAG|AAGGA|GATATACAT|ATG|GGTACC|GACTCTCTGGAATTCATCGCTTCTAA ACTGGCT|CTGGAAGTTCTGTTCCAGGGTCCG|CTGCAG|CACCACCACCACCACCAC|CCATGG ACTAGTGCTAGC

C terminal region

Dockerin Type I | T7 terminator

aaagtggtacctggtactccttctactaaattatacggcgacgtcaatgatgacggaaaagttaa
ctcaactgacgctgtagcattgaagagatatgttttgagatcaggtataagcatcaacactgaca
atgccgatttgaatgaagacggcagagttaattcaactgacttaggaattttgaagagatatatt
ctcaaagaaatagatacattgccgtacaagaac|TAA|CTCGAGTAAGATCCGGCTGCTAACAAA
GCCCGAAAGGAAGCTGAGTTGGCTGCTGCCACCGCTGAGCAATAA|CTAGCATAACCCCTTGGGG
CCTCTAAACGGGTCTTGAGGGGTTTTTT

10 FibronectinIII (4x):

Glycin-Serin Linker (x6)

GTTAGTGATGTTCCGCGTGATCTGGAAGTTGTTGCAGCAACCCCGACCAGCCTGCTGATTAGCTG
GGATGCACCGGCAGTTACCGTTCGTTATTATCGTATTACCTATGGTGAAACCGGTGGTAATAGTC
CGGTTCAAGAATTTACCGTTCCGGGTAGCAAAAGCACCGCAACCATTAGCGGTCTGAAACCGGGT
GTTGATTACACCATTACCGTTTATGCCGTTACCGGTCGTGGTGATTCACCGGCAAGCAGCAAACC
GATTAGCATTAACTATCGTACCGGTAGCGGTAGTGGTAGCGTTTCAGATGTGCCTCGCGACCTGG
AAGTGGTGGCTGCCACACCGACCTCACTGCTGATCTCATGGGATGCCCCTGCCGTGACCGTGCGC
TATTATCGCATCACATATGGCGAGACAGGTGGCAATTCACCTGTGCAAGAATTCACAGTTCCTGG
TTCAAAAAGTACCGCCACAATTTCTGGCCTGAAACCTGGCGTGGATTACACAATCACAGTGTATG
CAGTGACAGGTCGCGGTGATAGTCCGGCAAGTTCAAAACCGATTTCAATCAATTATCGCACCGGC
TCTGGCTCTGGCTCTGTTAGTGATGTTCCGCGTGATCTGGAAGTTGTTGCAGCAACCCCGACCAG
CCTGCTGATTAGCTGGGATGCACCGGCAGTTACCGTTCGTTATTATCGTATTACCTATGGTGAAA
CCGGTGGTAATAGTCCGGTTCAAGAATTTACCGTTCCGGGTAGCAAAAGCACCGCAACCATTAGC
GGTCTGAAACCGGGTGTTGATTACACCATTACCGTTTATGCCGTTACCGGTCGTGGTGATTCACC
GGCAAGCAGCAAACCGATTAGCATTAACTATCGTACCGGTAGCGGTAGTGGTAGCGTTTCAGATG
TGCCTCGCGACCTGGAAGTGGTGGCTGCCACACCGACCTCACTGCTGATCTCATGGGATGCCCCT
GCCGTGACCGTGCGCTATTATCGCATCACATATGGCGAGACAGGTGGCAATTCACCTGTGCAAGA
ATTCACAGTTCCTGGTTCAAAAAGTACCGCCACAATTTCTGGCCTGAAACCTGGCGTGGATTACA
CAATCACAGTGTATGCAGTGACAGGTCGCGGTGATAGTCCGGCAAGTTCAAAACCGATTTCAATC
AAttaTCGCACC

sfGFP:

AGCAAAGGTGAAGAACTGTTTACCGGTGTTGTTCCGATTCTGGTTGAACTGGATGGTGATGTTAA
TGGCCACAAATTTTCAGTTCGTGGTGAAGGCGAAGGTGATGCAACCATTGGTAAACTGACCCTGA
AATTTATCTGTACCACCGGCAAACTGCCGGTTCCGTGGCCGACCCTGGTTACCACCCTGACCTAT
GGTGTTCAGTGTTTTAGCCGTTATCCGGATCATATGAAACGCCACGATTTTTTCAAAAGCGCAAT
GCCGGAAGGTTATGTTCAAGAACGTACCATCTCCTTTAAAGACGACGGTAAATACAAAACCCGTG
CCGTTGTTAAATTTGAAGGTGATACCCTGGTGAATCGCATTGAACTGAAAGGCACCGATTTTAAA
GAGGATGGTAATATCCTGGGCCACAAACTGGAATATAATTTCAATAGCCACAACGTGTATATCAC
CGCAGACAAACAGAAAAATGGCATCAAAGCCAATTTTACCGTGCGCCATAATGTTGAAGATGGTA
GCGTGCAGCTGGCAGATCATTATCAGCAGAATACCCCGATTGGTGATGGTCCGGTTCTGCTGCCG
GATAATCATTATCTGAGCACCCAGACCGTTCTGAGCAAAGATCCGAATGAAAAACGTGATCATAT
GGTGCTGCATGAGTATGTTAATGCAGCAGGTATTACCCATGGTATGGATGAGCTGTATAAG

alpha-Spectrin repeat 16 (chicken brain) (x2):

Glycin-Serine Linker (x6)

CGTGCTAAACTGAACGAATCTCACCGTCTGCACCAGTTCTTCCGTGACATGGACGACGAAGAATC
TTGGATCAAAGAAAAAAAACTGCTGGTTTCTTCTGAAGACTACGGTCGTGACCTGACCGGTGTTC

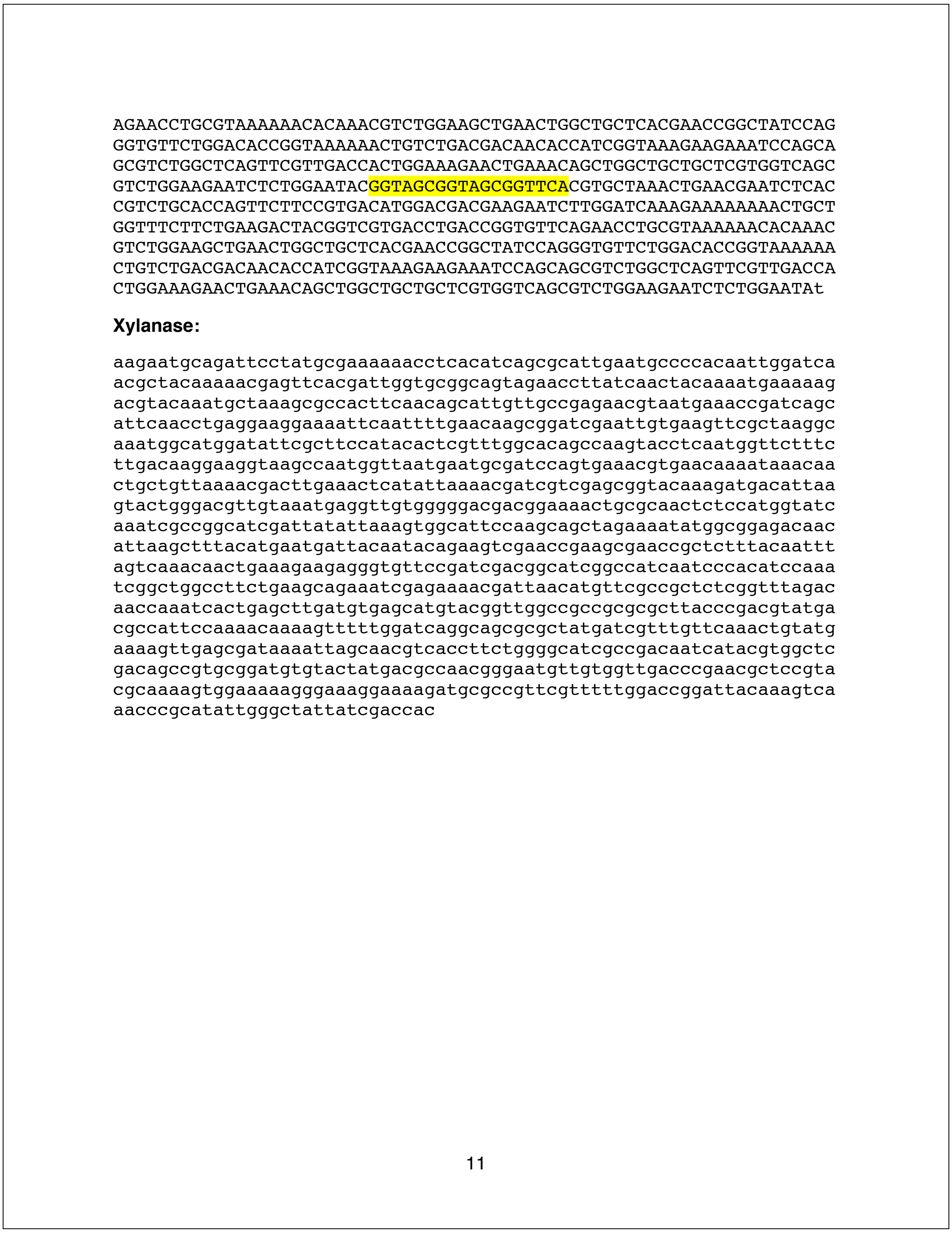

```
AGAACCTGCGTAAAAAACACAAACGTCTGGAAGCTGAACTGGCTGCTCACGAACCGGCTATCCAG
GGTGTTCTGGACACCGGTAAAAAACTGTCTGACGACAACACCATCGGTAAAGAAGAAATCCAGCA
GCGTCTGGCTCAGTTCGTTGACCACTGGAAAGAACTGAAACAGCTGGCTGCTGCTCGTGGTCAGC
GTCTGGAAGAATCTCTGGAATACGGTAGCGGTAGCGGTTCACGTGCTAAACTGAACGAATCTCAC
CGTCTGCACCAGTTCTTCCGTGACATGGACGACGAAGAATCTTGGATCAAAGAAAAAAAACTGCT
GGTTTCTTCTGAAGACTACGGTCGTGACCTGACCGGTGTTCAGAACCTGCGTAAAAAACACAAAC
GTCTGGAAGCTGAACTGGCTGCTCACGAACCGGCTATCCAGGGTGTTCTGGACACCGGTAAAAAA
CTGTCTGACGACAACACCATCGGTAAAGAAGAAATCCAGCAGCGTCTGGCTCAGTTCGTTGACCA
CTGGAAAGAACTGAAACAGCTGGCTGCTGCTCGTGGTCAGCGTCTGGAAGAATCTCTGGAATAt
```

Xylanase:

```
aagaatgcagattcctatgcgaaaaaacctcacatcagcgcattgaatgccccacaattggatca
acgctacaaaaacgagttcacgattggtgcggcagtagaaccttatcaactacaaaatgaaaaag
acgtacaaatgctaaagcgccacttcaacagcattgttgccgagaacgtaatgaaaccgatcagc
attcaacctgaggaaggaaaattcaattttgaacaagcggatcgaattgtgaagttcgctaaggc
aaatggcatggatattcgcttccatacactcgtttggcacagccaagtacctcaatggttctttc
ttgacaaggaaggtaagccaatggttaatgaatgcgatccagtgaaacgtgaacaaaataaacaa
ctgctgttaaaacgacttgaaactcatattaaaacgatcgtcgagcggtacaaagatgacattaa
gtactgggacgttgtaaatgaggttgtgggggacgacggaaaactgcgcaactctccatggtatc
aaatcgccggcatcgattatattaaagtggcattccaagcagctagaaaatatggcggagacaac
attaagctttacatgaatgattacaatacagaagtcgaaccgaagcgaaccgctctttacaattt
agtcaaacaactgaaagaagagggtgttccgatcgacggcatcggccatcaatcccacatccaaa
tcggctggccttctgaagcagaaatcgagaaaacgattaacatgttcgccgctctcggtttagac
aaccaaatcactgagcttgatgtgagcatgtacggttggccgccgcgcgcttacccgacgtatga
cgccattccaaaacaaaagtttttggatcaggcagcgcgctatgatcgtttgttcaaactgtatg
aaaagttgagcgataaaattagcaacgtcaccttctggggcatcgccgacaatcatacgtggctc
gacagccgtgcggatgtgtactatgacgccaacgggaatgttgtggttgacccgaacgctccgta
cgcaaaagtggaaaaagggaaaggaaaagatgcgccgttcgtttttggaccggattacaaagtca
aacccgcatattgggctattatcgaccac
```

References

1. Maerkl, S.J. & Quake, S.R. A systems approach to measuring the binding energy landscapes of transcription factors. Science 315, 233-237 (2007).

2. Gibson, D. G. et al. Enzymatic assembly of DNA molecules up to several hundred kilobases. Nat Meth 6, 343–345 (2009).

3. Stahl, S. W. et al. Single-molecule dissection of the high-affinity cohesin-dockerin complex. Proceedings of the National Academy of Sciences 109, 20431–20436 (2012).

4. Zimmermann, J. L., Nicolaus, T., Neuert, G. & Blank, K. Thiol-based, site-specific and covalent immobilization of biomolecules for single-molecule experiments. Nature Protocols 5, 975–985 (2010).

5. Jobst, M. A., Schoeler, C., Malinowska, K. & Nash, M. A. Investigating Receptor-ligand Systems of the Cellulosome with AFM-based Single-molecule Force Spectroscopy. JoVE (Journal of Visualized Experiments) e50950–e50950 (2013).

6. Meyer, P., Strackharn, M., Baumann, S. & Lang, M. A multicolor TIRF microscope. (TOPTICA Photonics AG, 2012).

7. Hutter, J. L. & Bechhoefer, J. Calibration of atomic-force microscope tips. Rev. Sci. Instrum. 64, 1868–1873 (1993).

8. Cook, S. M. et al. Practical implementation of dynamic methods for measuring atomic force microscope cantilever spring constants. Nanotechnology 17, 2135–2145 (2006).

9. Proksch, R., Schäffer, T. E., Cleveland, J. P., Callahan, R. C. & Viani, M. B. Finite optical spot size and position corrections in thermal spring constant calibration. Nanotechnology 15, 1344–1350 (2004).

10. Puchner, E. M., Franzen, G., Gautel, M. & Gaub, H. E. Comparing Proteins by Their Unfolding Pattern. Biophysical Journal 95, 426–434 (2008).

A.3 Supplementary information to associated publication P1

Electronic Supplementary Information

Methods

Chip fabrication

Flow and control wafers were obtained from the Stanford Microfluidics Foundry, design name DTPAd, according to the 640-chamber MITOMI design from [1]. This design features 15 μm high flow channels, rounded by photoresist reflow, and a rectangular control channel cross-section for optimal valve closing operation. PDMS chips were fabricated as follows: For the control layer, a 5:1 mixture of Sylgard 184 (Dow Corning) base:curing agent was poured onto the wafer, degassed, partially cured at 80°C for 20 min. The flow layer wafer was spin-coated at 2500 rpm for 75 s with a 20:1 base:curing agent mixture of Sylgard 184 and partially cured at 80°C for 30 min. The control layers were cut out, holes were punched and control layers were aligned onto the flow layer PDMS on the flow layer wafer. Assembled chips were baked at 80°C for 90 min, cut, peeled off the flow layer wafer and holes were punched. After fabrication, PDMS chips were stored under Argon atmosphere for no more than 1 month.

Chip functionalization

The chip was bonded onto a clean glass slide at 80°C for 5 h. hydrochloric acid (12.5 %) was flushed into the chip for overnight storage in humid atmosphere. Silanization was prepared by flushing with ethanol for 20 min. A mixture of 70 % 3-Aminopropyldimethyl-ethoxysilane (ABCR), 5 % H_2SO_4, 25% ddH_2O was prepared, stirred for 1 h, mixed 1:4 with EtOH, and flowed through the chip for 30 min, followed by 10 min rinsing with ethanol. The silanization was consolidated by baking the chip at 80°C after peeling it off the glass slide. PEGylation was prepared by 30 min pre-incubation in borate buffer (50 mM sodium borate, pH 8.5) and accomplished by incubating the chip with 0.25 mg/ml NHS-PEG-Maleimide (MW 5000, Rapp Polymere), dissolved in borate buffer, and covered with a glass slip. The chip was then rinsed with ddH_2O and bonded for 30 min at 80°C onto a clean glass slide. For DNA functionalization, strand 1 (oligo sequences below) at 2 μM in coupling buffer (50 mM sodium phosphate pH 7.2, 50mM NaCl, 10 mM EDTA) was first flowed through the chip for 60 minutes, with the unused back chambers of the flow chambers sealed off using the corresponding valve. DNA oligos 2 and 3 were pre-incubated in 5x phosphate buffered saline (PBS) for 2 hours at concentrations of 2 μM (strand 2) and 4 μM (strand 3) and then flushed through the chip for 60 min. In parallel, a #1 thickness cover slip was prepared to serve as stamping counterpart: Therefore, it was amino-silanized (30 min), treated with NHS-PEG-Biotin (60 min, 0.25 mg/mL in Borate buffer, MW 3000, Rapp Polymere), and incubated with Neutravidin (60 min, 1 mg/mL in PBS), and rinsed with ddH_2O. Finally, the chip was rinsed and prepared for quick transfer onto the Neutravidin-presenting glass slide with a solution of 30 mM Trehalose and 5 ppm Tween in PBS allowed for short-term wetting and stabilization of the PDMS-surface-bound DNA oligomers. For all of these steps, flow layer pressure was kept constant at 4 psi.

Oligomer sequences

All oligomers were purchased from IBA GmbH. 5’-GAA TTC-3’ is the palindromic recognition sequence of EcoRI and is displayed in the duplex of strands 1 and 2. For the all-DNA probe experiments, the following three strands were used:

Strand 1: (SH)-5'-tttttttttt-CTG CAG GAA TTC GAT ATC AAG CTT ATC GAT-3'

Strand 2: 3'-GAC GTC CTT AAG CTA TAG TTC GAA TAG CTA C-ttttttt-5'-(Cy5)-5'-ttttttt-C GAC GTC CTT AAG CTA TAG TTC GAA TAG CTA-3'

Strand 3: Biotin-5'-tttttttttt-TAG CTA TTC GAA CTA TAG CTT AAG GAC GTC-(Cy3)-3'

For the multiplexing experiments, the following strands were used in various combinations:

Strand 1-consensus: (SH)-5'-tttttttttt-TAGACCGGAATGAATTCGCTTATCT-3'

Strand 1-star: (SH)-5'-tttttttttt-TAGACCGGAATGAATTGGCTTATCT-3'

Strand 2-consensus: 3'-ATCTGGCCTTACTTAAGCGAATAGA-ttttttt-5'-(cy5)-5'-ttttttt-TTAGTAAGGGAGCATATTGCATACGTTGAGGACTTATCAG-3'

Strand 2-star: 3'-ATCTGGCCTTACTTAACCGAATAGA-ttttttt-5'-(cy5)-5'-ttttttt-TTAGTAAGGGAGCATATTGCATACGTTGAGGACTTATCAG-3'

Strand 3-25bp: Biotin-5'-tttttttttt-CTGATAAGTCCTCAACGTATGCAAT (Cy3)-3'

Strand 3-30bp: Biotin-5'-tttttttttt-CTGATAAGTCCTCAACGTATGCAATATGCT (Cy3)-3'

Strand 3-35bp: Biotin-5'-tttttttttt-CTGATAAGTCCTCAACGTATGCAATATGCTCCCTT (Cy3)-3'

Strand 3-40bp: Biotin-5'-tttttttttt-CTGATAAGTCCTCAACGTATGCAATATGCTCCCTTACTAA (Cy3)-3'

Prior to each experiment, Thiol-containing strands were reduced with 5 mM TCEP (Thermo Fischer Scientific), purified by ethanol precipitation and resuspended in coupling buffer. EcoRI was purchased from New England Biolabs and flushed into the chip at a concentration of 10 nM in a buffer solution (pH 7.6) containing 10 mM HEPES, 170 mM NaCl, 1 mM EDTA, 50 μM DTT, and 100 μg/mL BSA.

Contacting mechanism

The functionalized chip, bound to the Neutravidin glass slide, was flushed with 1x PBS at a reduced pressure of 0.5 psi prior to button actuation (“stamping”) and measurement. The button valve pressure was linearly increased from 0 psi to 15 psi over 150 s. After a contact time of 10 min, the button was retracted by lowering the pressure to 0 psi linearly over 150 s.

Readout

Data acquisition was performed chamber-by-chamber, scanning the microfluidic chip. Confocal stacks of up to 25 images at a vertical distance of 1 μm were recorded for the cy3 and cy5 channels using a spinning disk unit (Yokogawa) and an EMCCD Camera (Andor) on an inverted microscope through a 40x / 1.3 NA oil immersion objective (Carl Zeiss). The chip was scanned using hybrid DC/piezo motors (Physik Instrumente) for x- and y-directions, an objective piezo positioner (Physik Instrumente) for z-direction and a custom-designed scan software (Labview, National Instruments). Excitation lasers at 532 nm (cy3 channel) and 640 nm (cy5 channel) were used in combination with emission filters at 593 nm and 676 nm (AHF Analysentechnik). The exposure time was set to 100 ms to balance data quality and experiment duration. Thus, a 640-chamber chip can be scanned and imaged in 60-90 minutes. If time constraints apply, reducing the exposure time and/or increasing the confocal slice-to-slice distance will speed up readout at the expense of raw data signal-to-noise and fit quality.

Analysis

The recorded stacks of confocal fluorescent images were analyzed by choosing two distinct circular regions of interest (ROI): Region 1 corresponds to the button valve contact area, while region 2 does not overlap with the contact area. Vertical mean intensity profiles were plotted for each region and fluorescent channel. These profiles were fitted with the sum of two Gaussian functions and a constant background offset in the case of contacted region 1, and the sum of a single Gaussian and a constant background in the case of no-contact region 2. These Gaussian fit data yield integrated intensity values for each region, channel, and location (top/bottom). From these, relative rupture probabilities are computed, namely the value of normalized fluorescence. Its value between 0 and 1 denotes the fraction of probes under load, which rupture at the bottom bond.

Bell-Evans model

The multiplexing application data can be fitted with a Bell-Evans model simulation, as described in high detail previously [2]. In short, both the probe and reference bonds can be described by a two-state rupture probability depending on force f, force loading rate f', potential width Δx and rate k_{off}:

$$p(f,f') = \frac{k_{off}}{f'} \cdot \exp\left(\frac{f \cdot \Delta x}{k_B T}\right) \cdot \exp\left(-\frac{k_{off}}{f'} \cdot \int_0^f du \cdot \exp\left(\frac{u \cdot \Delta x}{k_B T}\right)\right)$$

Δx and $\log(k_{off})$ are assumed to be linear functions of oligomer length n:

$$k_{off} = 10^{\alpha - \beta \cdot n} s^{-1}$$

$$\Delta x = (t + n \cdot m) \cdot 10^{-10} m$$

α, β, t and m are the independent fit parameters. For dsDNA, previous experimental studies have found: $\alpha = (3 \pm 1)$, $\beta = (0.5 \pm 0.1)$, t = (7 ± 3), m = (0.7 ± 0.3)[3]. The loading rate of 10^5 pN s^{-1} was estimated experimentally from PDMS stamp separation velocity, effective spring constants of the PEG linkers and the functionalization density [4]. The oligomer length dependence of normalized fluorescence is then given by:

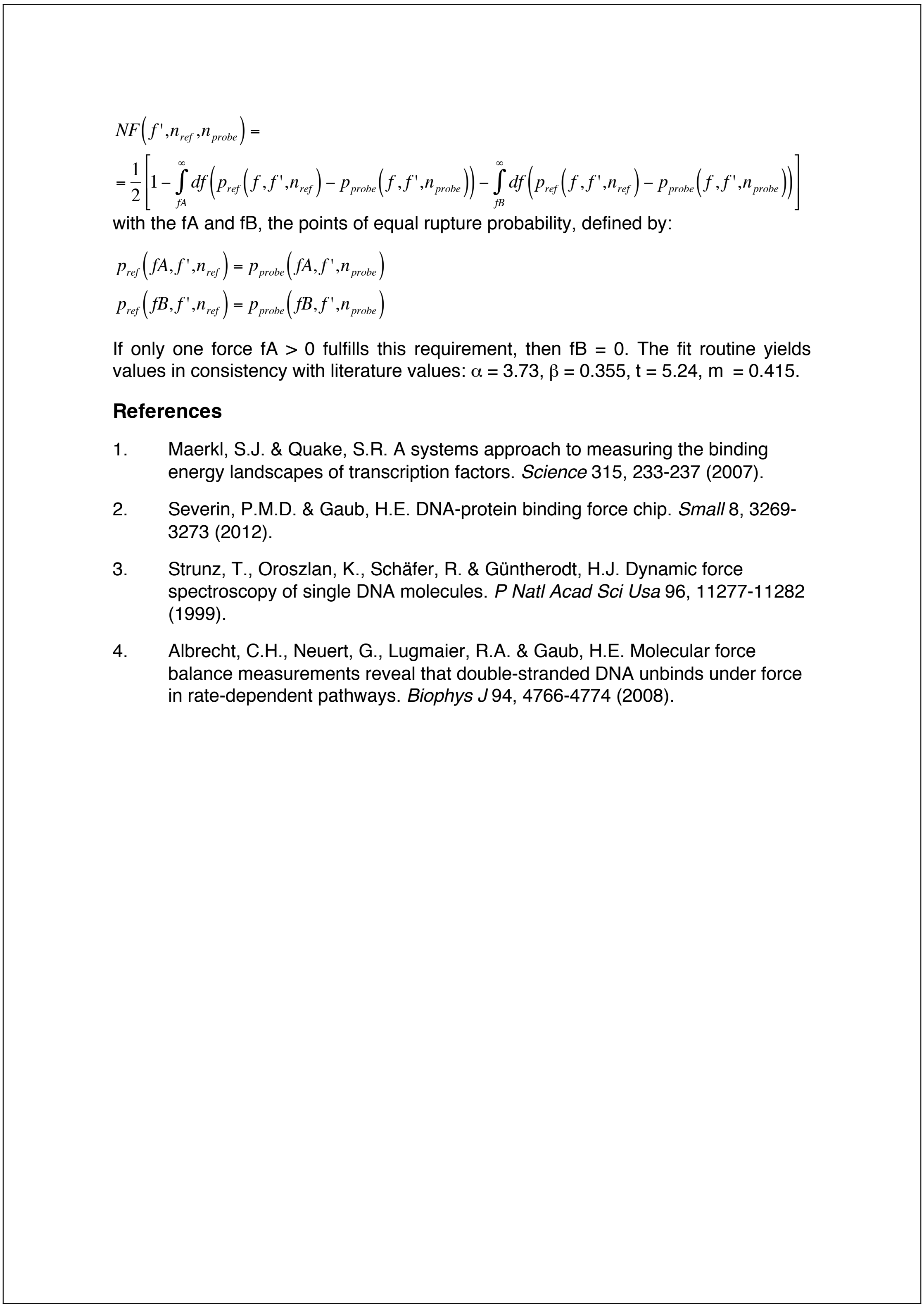

$$NF\left(f', n_{ref}, n_{probe}\right) =$$

$$= \frac{1}{2}\left[1 - \int_{fA}^{\infty} df \left(p_{ref}\left(f, f', n_{ref}\right) - p_{probe}\left(f, f', n_{probe}\right)\right) - \int_{fB}^{\infty} df \left(p_{ref}\left(f, f', n_{ref}\right) - p_{probe}\left(f, f', n_{probe}\right)\right)\right]$$

with the fA and fB, the points of equal rupture probability, defined by:

$$p_{ref}\left(fA, f', n_{ref}\right) = p_{probe}\left(fA, f', n_{probe}\right)$$

$$p_{ref}\left(fB, f', n_{ref}\right) = p_{probe}\left(fB, f', n_{probe}\right)$$

If only one force fA > 0 fulfills this requirement, then fB = 0. The fit routine yields values in consistency with literature values: $\alpha = 3.73$, $\beta = 0.355$, $t = 5.24$, $m = 0.415$.

References

1. Maerkl, S.J. & Quake, S.R. A systems approach to measuring the binding energy landscapes of transcription factors. *Science* 315, 233-237 (2007).
2. Severin, P.M.D. & Gaub, H.E. DNA-protein binding force chip. *Small* 8, 3269-3273 (2012).
3. Strunz, T., Oroszlan, K., Schäfer, R. & Güntherodt, H.J. Dynamic force spectroscopy of single DNA molecules. *P Natl Acad Sci Usa* 96, 11277-11282 (1999).
4. Albrecht, C.H., Neuert, G., Lugmaier, R.A. & Gaub, H.E. Molecular force balance measurements reveal that double-stranded DNA unbinds under force in rate-dependent pathways. *Biophys J* 94, 4766-4774 (2008).

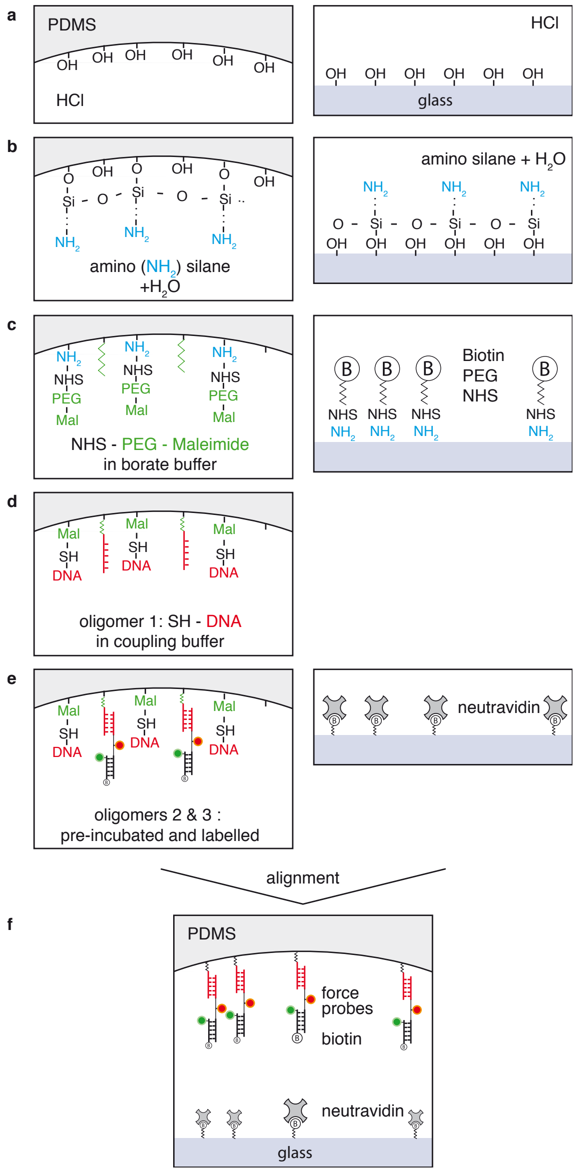

Supplemental Figure 1

Chip and slide functionalization. (a)-(e) schematically summarize the multistep functionalization procedure of chip and slide as described in the online method section. (f) shows the resulting setup after chip and slide alignment.

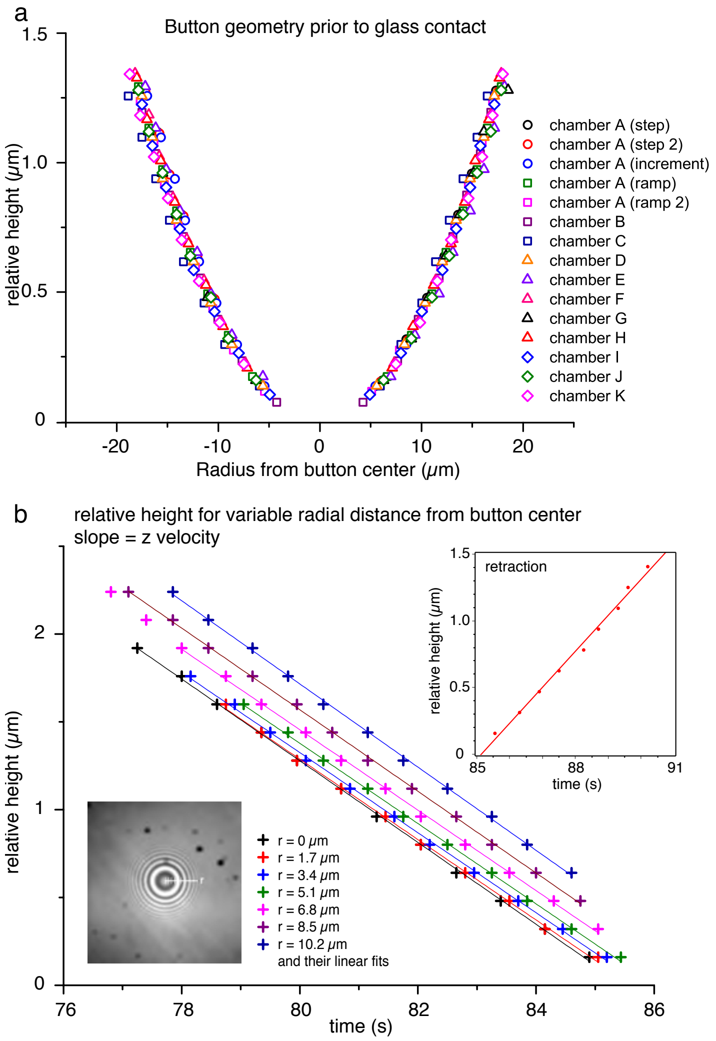

Supplemental Figure 2

Button geometry and dynamics. (a) Button geometry just prior to glass contact in multiple chambers, determined by interference patterns between glass and PDMS in microscopy. (b) PDMS-Glass distance plotted against time. Various radial distances from button valve center (cf. bottom-left inset) are plotted for approach dynamics (main graph) and compared to a typical retraction curve (top-right inset). These data are collected from time-course interference pattern changes. Data (crosses) are fitted with linear functions (lines). The slope of each fit allows for the determination of approach or retraction velocities.

Bibliography

[1] Rothemund, P.W.K. (2006). Folding DNA to create nanoscale shapes and patterns. *Nature*, **440**(7082), 297–302.

[2] Kufer, S.K., Puchner, E.M., Gumpp, H., Liedl, T., and Gaub, H.E. (2008). Single-molecule cut-and-paste surface assembly. *Science*, **319**(5863), 594–596.

[3] Howorka, S., Cheley, S., and Bayley, H. (2001). Sequence-specific detection of individual DNA strands using engineered nanopores. *Nat Biotechnol*, **19**(7), 636–9.

[4] Eid, J., Fehr, A., Gray, J., Luong, K., Lyle, J., *et al.* (2009). Real-time DNA sequencing from single polymerase molecules. *Science*, **323**(5910), 133–8.

[5] Davis, M.E., Chen, Z.G., and Shin, D.M. (2008). Nanoparticle therapeutics: an emerging treatment modality for cancer. *Nat Rev Drug Discov*, **7**(9), 771–82.

[6] Petros, R.A. and DeSimone, J.M. (2010). Strategies in the design of nanoparticles for therapeutic applications. *Nat Rev Drug Discov*, **9**(8), 615–27.

[7] Giot, L., Bader, J.S., Brouwer, C., Chaudhuri, A., Kuang, B., *et al.* (2003). A protein interaction map of Drosophila melanogaster. *Science*, **302**(5651), 1727–1736.

[8] Ozdemir, A. and Stathopoulos, A. (2011). Exciting times: bountiful data to facilitate studies of cis-regulatory control. *Nat Methods*, **8**(12), 1016–1017.

[9] Puchner, E. and Gaub, H. (2012). Single-molecule mechanoenzymatics. *Annual Review of Biophysics*, **41**, 497–518.

[10] Fletcher, D.A. and Mullins, R.D. (2010). Cell mechanics and the cytoskeleton. *Nature*, **463**(7280), 485–92.

[11] Haeberle, S. and Zengerle, R. (2007). Microfluidic platforms for lab-on-a-chip applications. *Lab Chip*, **7**(9), 1094–110.

[12] Dobson, C.M. (1999). Protein misfolding, evolution and disease. *Trends Biochem Sci*, **24**(9), 329–32.

[13] Chiti, F. and Dobson, C.M. (2006). Protein misfolding, functional amyloid, and human disease. *Annu Rev Biochem*, **75**, 333–66.

[14] Wüthrich, K. (2003). NMR studies of structure and function of biological macromolecules. *Angewandte Chemie*, **42**(29), 3340–63.

[15] Sotomayor, M. and Schulten, K. (2007). Single-molecule experiments in vitro and in silico. *Science*, **316**, 1144–1148.

[16] Boehr, D.D. and Wright, P.E. (2008). How Do Proteins Interact? *Science*, **320**(5882), 1429–1430.

[17] Shoemaker, B.A. and Panchenko, A.R. (2007). Deciphering Protein–Protein Interactions. Part I. Experimental Techniques and Databases. *PLoS Comput Biol*, **3**(3), 337–344.

[18] Krogan, N.J., Cagney, G., Yu, H., Zhong, G., Guo, X., *et al.* (2006). Global landscape of protein complexes in the yeast Saccharomyces cerevisiae. *Nature*, **440**(7084), 637–643.

[19] Li, S., Armstrong, C.M., Bertin, N., Ge, H., Milstein, S., *et al.* (2004). A Map of the Interactome Network of the Metazoan C. elegans. *Science*, **303**(5657), 540–543.

[20] Hakes, L., Pinney, J.W., Robertson, D.L., and Lovell, S.C. (2007). Protein-protein interaction networks and biology—what's the connection? *Nat Biotechnol*, **26**(1), 69–72.

[21] Bizzarri, A.R. and Cannistraro, S. (2010). The application of atomic force spectroscopy to the study of biological complexes undergoing a biorecognition process. *Chem. Soc. Rev.*, **39**(2), 734.

[22] Himmel, M.E., Xu, Q., Luo, Y., Ding, S.Y., Lamed, R., *et al.* (2010). Microbial enzyme systems for biomass conversion: emerging paradigms. *Biofuels*, **1**(2), 323–341.

[23] Stahl, S., Nash, M., Fried, D., Slutzki, M., Barak, Y., *et al.* (2012). Single-molecule dissection of the high-affinity cohesin–dockerin complex. *Proc. Natl. Acad. Sci. USA*, **109**(50), 20431–20436.

[24] Hornung, V. and Latz, E. (2010). Intracellular DNA recognition. *Nat Rev Immunol*, **10**(2), 123–30.

[25] Jiricny, J. (2006). The multifaceted mismatch-repair system. *Nat Rev Mol Cell Biol*, **7**(5), 335–46.

[26] Jackson, S.P. and Bartek, J. (2009). The DNA-damage response in human biology and disease. *Nature*, **461**(7267), 1071–8.

[27] Koirala, D., Yangyuoru, P.M., and Mao, H. (2013). Mechanical affinity as a new metrics to evaluate binding events. *Reviews in Analytical Chemistry*, **32**(3), 197–208.

[28] Arlett, J.L., Myers, E.B., and Roukes, M.L. (2011). Comparative advantages of mechanical biosensors. *Nat Nanotechnol*, **6**(4), 203–215.

[29] Stormo, G.D. and Zhao, Y. (2010). Determining the specificity of protein-DNA interactions. *Nat Rev Genet*, **11**(11), 751–60.

[30] Weirauch, M.T., Cote, A., Norel, R., Annala, M., Zhao, Y., *et al.* (2013). Evaluation of methods for modeling transcription factor sequence specificity. *Nat Biotechnol*, **31**(2), 126–34.

[31] Nutiu, R., Friedman, R., Luo, S., Khrebtukova, I., Silva, D., *et al.* (2011). Direct measurement of DNA affinity landscapes on a high-throughput sequencing instrument. *Nat Biotechnol*, **29**(7), 659–664.

[32] Karpova, T.S., Kim, M.J., Spriet, C., Nalley, K., Stasevich, T.J., *et al.* (2008). Concurrent fast and slow cycling of a transcriptional activator at an endogenous promoter. *Science*, **319**(5862), 466–469.

[33] Lickwar, C.R., Mueller, F., Hanlon, S.E., Mcnally, J.G., and Lieb, J.D. (2012). Genome-wide protein-DNA binding dynamics suggest a molecular clutch for transcription factor function. *Nature*, **484**(7393), 251–255.

[34] Xie, Z., Hu, S., Qian, J., Blackshaw, S., and Zhu, H. (2011). Systematic characterization of protein-DNA interactions. *Cellular and Molecular Life Sciences*, **68**, 1657–1668.

[35] Yokoe, H. and Anholt, R.R. (1993). Molecular cloning of olfactomedin, an extracellular matrix protein specific to olfactory neuroepithelium. *Proc. Natl. Acad. Sci. USA*, **90**(10), 4655–9.

[36] Li, J.J. and Herskowitz, I. (1993). Isolation of ORC6, a component of the yeast origin recognition complex by a one-hybrid system. *Science*, **262**(5141), 1870–4.

[37] Massie, C.E. and Mills, I.G. (2008). ChIPping away at gene regulation. *EMBO Rep*, **9**(4), 337–43.

[38] Bulyk, M.L., Huang, X., Choo, Y., and Church, G.M. (2001). Exploring the DNA-binding specificities of zinc fingers with DNA microarrays. *Proc. Natl. Acad. Sci. USA*, **98**(13), 7158–63.

[39] Badis, G., Berger, M.F., Philippakis, A.A., Talukder, S., Gehrke, A.R., *et al.* (2009). Diversity and complexity in DNA recognition by transcription factors. *Science*, **324**(5935), 1720–3.

[40] Hens, K., Feuz, J.D., Isakova, A., Iagovitina, A., Massouras, A., *et al.* (2011). Automated protein-DNA interaction screening of Drosophila regulatory elements. *Nat Methods*, **8**(12), 1065–1070.

[41] Lesser, D.R., Kurpiewski, M.R., and Jen-Jacobson, L. (1990). The energetic basis of specificity in the Eco RI endonuclease–DNA interaction. *Science*, **250**(4982), 776–86.

[42] Jen-Jacobson, L. (1997). Protein–DNA Recognition Complexes: Conservation of Structure and Binding Energy in the Transition State. *Biopolymers*, **44**(2), 153–180.

[43] Kim, Y.C., Grable, J.C., Love, R., Greene, P.J., and Rosenberg, J.M. (1990). Refinement of Eco RI endonuclease crystal structure: a revised protein chain tracing. *Science*, **249**(4974), 1307–9.

[44] Wittmann, T., Hyman, A., and Desai, A. (2001). The spindle: a dynamic assembly of microtubules and motors. *Nature Cell Biology*, **3**(1), E28–34.

[45] Parent, C.A. and Devreotes, P.N. (1999). A cell's sense of direction. *Science*, **284**(5415), 765–70.

[46] Rodriguez, O.C., Schaefer, A.W., Mandato, C.A., Forscher, P., Bement, W.M., *et al.* (2003). Conserved microtubule–actin interactions in cell movement and morphogenesis. *Nature Cell Biology*, **5**(7), 599–609.

[47] Ren, X.D., Kiosses, W.B., and Schwartz, M.A. (1999). Regulation of the small GTP-binding protein Rho by cell adhesion and the cytoskeleton. *EMBO J*, **18**(3), 578–85.

[48] Cook, T.A., Nagasaki, T., and Gundersen, G.G. (1998). Rho guanosine triphosphatase mediates the selective stabilization of microtubules induced by lysophosphatidic acid. *J Cell Biol*, **141**(1), 175–85.

[49] Etienne-Manneville, S. and Hall, A. (2002). Rho GTPases in cell biology. *Nature*, **420**(6916), 629–35.

[50] Wiche, G. (1998). Role of plectin in cytoskeleton organization and dynamics. *J Cell Sci*, **111**(17), 2477–86.

[51] Loverdo, C., Bénichou, O., Moreau, M., and Voituriez, R. (2008). Enhanced reaction kinetics in biological cells. *Nature Physics*, **4**, 134–137.

[52] Dix, J.A. and Verkman, A.S. (2008). Crowding effects on diffusion in solutions and cells. *Annual Review of Biophysics*, **37**, 247–63.

[53] Binnig, G., Quate, C., and Gerber, C. (1986). Atomic force microscope. *Phys Rev Lett*, **56**(9), 930–933.

[54] Moy, V.T., Florin, E.L., and Gaub, H.E. (1994). Intermolecular forces and energies between ligands and receptors. *Science*, **266**(5183), 257–9.

[55] Gumpp, H., Stahl, S.W., Strackharn, M., Puchner, E.M., and Gaub, H.E. (2009). Ultrastable combined atomic force and total internal reflection fluorescence microscope. *Rev Sci Instrum*, **80**(6), 063704.

[56] Puchner, E.M., Franzen, G., Gautel, M., and Gaub, H.E. (2008). Comparing proteins by their unfolding pattern. *Biophys J*, **95**(1), 426–34.

[57] Puchner, E.M. and Gaub, H.E. (2009). Force and function: probing proteins with AFM-based force spectroscopy. *Curr Opin Struct Biol*, **19**(5), 605–14.

[58] Puchner, E.M., Alexandrovich, A., Kho, A.L., Hensen, U., Schäfer, L., *et al.* (2008). Mechanoenzymatics of titin kinase. *Proc. Natl. Acad. Sci. USA*, **105**(36), 13385–13390.

[59] Rico, F., Gonzalez, L., Casuso, I., Puig-Vidal, M., and Scheuring, S. (2013). High-Speed Force Spectroscopy Unfolds Titin at the Velocity of Molecular Dynamics Simulations. *Science*, **342**(6159), 741–743.

[60] Neuman, K.C. and Nagy, A. (2008). Single-molecule force spectroscopy: optical tweezers, magnetic tweezers and atomic force microscopy. *Nat Methods*, **5**(6), 491–505.

[61] Severin, P.M.D., Ho, D., and Gaub, H.E. (2011). A high throughput molecular force assay for protein-DNA interactions. *Lab Chip*, **11**(5), 856–862.

[62] Albrecht, C.H., Blank, K., Lalic-Mülthaler, M., Hirler, S., Mai, T., *et al.* (2003). DNA: a programmable force sensor. *Science*, **301**(5631), 367–70.

[63] Severin, P.M.D., Zou, X., Gaub, H.E., and Schulten, K. (2011). Cytosine methylation alters DNA mechanical properties. *Nucleic Acids Res*, **39**(20), 8740–8751.

[64] Severin, P.M.D., Zou, X., Schulten, K., and Gaub, H.E. (2013). Effects of Cytosine hydroxymethylation on DNA strand separation. *Biophys J*, **104**(1), 208–15.

[65] Severin, P.M.D. and Gaub, H.E. (2012). DNA-protein binding force chip. *Small*, **8**(21), 3269–73.

[66] Limmer, K., Aschenbrenner, D., and Gaub, H. (2013). Sequence-specific inhibition of Dicer measured with a force-based microarray for RNA ligands. *Nucleic Acids Res*, **41**(6), e69.

[67] Spiller, D.G., Wood, C.D., Rand, D.A., and White, M.R.H. (2010). Measurement of single-cell dynamics. *Nature*, **465**(7299), 736–745.

[68] Radmacher, M. (2007). Studying the mechanics of cellular processes by atomic force microscopy. *Methods Cell Biol*, **83**, 347–72.

[69] Tao, N.J., Lindsay, S.M., and Lees, S. (1992). Measuring the microelastic properties of biological material. *Biophys J*, **63**(4), 1165–9.

[70] Rotsch, C. and Radmacher, M. (2000). Drug-induced changes of cytoskeletal structure and mechanics in fibroblasts: an atomic force microscopy study. *Biophys J*, **78**(1), 520–35.

[71] Gardel, M.L., Shin, J.H., MacKintosh, F.C., Mahadevan, L., Matsudaira, P., *et al.* (2004). Elastic Behavior of Cross-Linked and Bundled Actin Networks. *Science*, **304**, 1301–1306.

[72] Bursac, P., Lenormand, G., Fabry, B., Oliver, M., Weitz, D.A., *et al.* (2005). Cytoskeletal remodelling and slow dynamics in the living cell. *Nat Mater*, **4**, 557–561.

[73] Wirtz, D. (2009). Particle-Tracking Microrheology of Living Cells: Principles and Applications. *Annual Review of Biophysics*, **38**(1), 301–326.

[74] Arcizet, D., Meier, B., Sackmann, E., Rädler, J., and Heinrich, D. (2008). Temporal Analysis of Active and Passive Transport in Living Cells. *Phys Rev Lett*, **101**, 248103.

[75] Unger, M., Chou, H.P., Thorsen, T., Scherer, A., and Quake, S.R. (2000). Monolithic microfabricated valves and pumps by multilayer soft lithography. *Science*, **288**(5463), 113–116.

[76] Duffy, D.C., McDonald, J.C., Schueller, O.J., and Whitesides, G.M. (1998). Rapid Prototyping of Microfluidic Systems in Poly(dimethylsiloxane). *Anal Chem*, **70**(23), 4974–84.

[77] Melin, J. and Quake, S.R. (2007). Microfluidic large-scale integration: The evolution of design rules for biological automation. *Annu Rev Bioph Biom*, **36**, 213–231.

[78] Thorsen, T., Maerkl, S.J., and Quake, S.R. (2002). Microfluidic large-scale integration. *Science*, **298**(5593), 580–584.

[79] Maerkl, S.J. and Quake, S.R. (2007). A systems approach to measuring the binding energy landscapes of transcription factors. *Science*, **315**(5809), 233–237.

[80] Gerber, D., Maerkl, S.J., and Quake, S.R. (2009). An in vitro microfluidic approach to generating protein-interaction networks. *Nat Methods*, **6**(1), 71–74.

[81] Martin, L., Meier, M., Lyons, S.M., Sit, R.V., Marzluff, W.F., *et al.* (2012). Systematic reconstruction of RNA functional motifs with high-throughput microfluidics. *Nat Methods*, **9**(12), 1192–4.

[82] Meier, M., Sit, R.V., and Quake, S.R. (2013). Proteome-wide protein interaction measurements of bacterial proteins of unknown function. *Proc. Natl. Acad. Sci. USA*, **110**(2), 477–82.

[83] Geertz, M., Shore, D., and Maerkl, S. (2012). Massively parallel measurements of molecular interaction kinetics on a microfluidic platform. *Proc. Natl. Acad. Sci. USA*, **109**(41), 16540–16545.

[84] Fordyce, P.M., Gerber, D., Tran, D., Zheng, J., Li, H., *et al.* (2010). De novo identification and biophysical characterization of transcription-factor binding sites with microfluidic affinity analysis. *Nat Biotechnol*, **28**(9), 970–976.

[85] Squires, T. and Quake, S.R. (2005). Microfluidics: Fluid physics at the nanoliter scale. *Rev Mod Phys*, **77**(3), 977–1026.

[86] Mosadegh, B., Kuo, C.H., Tung, Y.C., suke Torisawa, Y., Bersano-Begey, T., *et al.* (2010). Integrated elastomeric components for autonomous regulation of sequential and oscillatory flow switching in microfluidic devices. *Nature Physics*, **6**, 433–437.

[87] Mosadegh, B., Bersano-Begey, T., Park, J.Y., Burns, M.A., and Takayama, S. (2011). Next-generation integrated microfluidic circuits. *Lab Chip*, **11**(17), 2797–3016.

[88] Lee, C.C., Sui, G., Elizarov, A., Shu, C.J., Shin, Y.S., *et al.* (2005). Multistep Synthesis of a Radiolabeled Imaging Probe Using Integrated Microfluidics. *Science*, **310**(5755), 1793–1796.

[89] Balagaddé, F.K., You, L., Hansen, C.L., Arnold, F.H., and Quake, S.R. (2005). Long-Term Monitoring of Bacteria Undergoing Programmed Population Control in a Microchemostat. *Science*, **309**(5731), 137–140.

[90] Hong, J.W., Studer, V., Hang, G., Anderson, W.F., and Quake, S.R. (2004). A nanoliter-scale nucleic acid processor with parallel architecture. *Nat Biotechnol*, **22**(4), 435–439.

[91] Fan, H.C., Wang, J., Potanina, A., and Quake, S.R. (2011). Whole-genome molecular haplotyping of single cells. *Nat Biotechnol*, **29**(1), 51–59.

[92] Mark, D., Haeberle, S., Roth, G., Stetten, F.V., and Zengerle, R. (2010). Microfluidic lab-on-a-chip platforms: requirements, characteristics and applications. *Chem. Soc. Rev.*, **39**(3), 1153.

[93] Lee, B.S., a Jung-Nam Lee, a Jong-Myeon Park, a Jeong-Gun Lee, a Suhyeon Kim, *et al.* (2009). A fully automated immunoassay from whole blood on a disc. *Lab Chip*, **9**, 1548–1555.

[94] Friend, J. and Yeo, L.Y. (2011). Microscale acoustofluidics: Microfluidics driven via acoustics and ultrasonics. *Rev Mod Phys*, **83**(2), 647–704.

[95] Agresti, J.J., Antipov, E., Abate, A.R., Ahn, K., Rowat, A.C., *et al.* (2010). Ultrahigh-throughput screening in drop-based microfluidics for directed evolution. *Proc. Natl. Acad. Sci. USA*, **107**(9), 4004–9.

[96] Guo, M.T., Rotem, A., Heyman, J.A., and Weitz, D.A. (2012). Droplet microfluidics for high-throughput biological assays. *Lab Chip*, **12**(12), 2146–2155.

[97] Leng, X., Zhang, W., Wang, C., Cui, L., and Yang, C.J. (2010). Agarose droplet microfluidics for highly parallel and efficient single molecule emulsion PCR. *Lab Chip*, **10**(21), 2841.

[98] Yin, J., Straight, P.D., McLoughlin, S.M., Zhou, Z., Lin, A.J., *et al.* (2005). Genetically encoded short peptide tag for versatile protein labeling by Sfp phosphopantetheinyl transferase. *Proc. Natl. Acad. Sci. USA*, **102**(44), 15815–20.

[99] Stögbauer, T., Windhager, L., Zimmer, R., and Rädler, J.O. (2012). Experiment and mathematical modeling of gene expression dynamics in a cell-free system. *Integr. Biol.*, **4**(5), 494–501.

[100] Otten, M., Wolf, P., and Gaub, H.E. (2013). Protein–DNA force assay in a microfluidic format. *Lab Chip*, **13**(21), 4198–4204.

[101] Otten, M., Nandi, A., Arcizet, D., Gorelashvili, M., Lindner, B., *et al.* (2012). Local Motion Analysis Reveals Impact of the Dynamic Cytoskeleton on Intracellular Subdiffusion. *Biophys J*, **102**(4), 758–767.

[102] Zahnd, C., Spinelli, S., Luginbühl, B., Amstutz, P., Cambillau, C., *et al.* (2004). Directed in vitro evolution and crystallographic analysis of a peptide-binding single chain antibody fragment (scFv) with low picomolar affinity. *J Biol Chem*, **279**(18), 18870–7.

[103] Morfill, J., Blank, K., Zahnd, C., Luginbühl, B., Kühner, F., *et al.* (2007). Affinity-matured recombinant antibody fragments analyzed by single-molecule force spectroscopy. *Biophys J*, **93**(10), 3583–90.

[104] Strackharn, M., Pippig, D.A., Meyer, P., Stahl, S.W., and Gaub, H.E. (2012). Nanoscale arrangement of proteins by single-molecule cut-and-paste. *J Am Chem Soc*, **134**(37), 15193–6.

[105] Saar, B.G., Zeng, Y., Freudiger, C.W., Liu, Y.S., Himmel, M.E., *et al.* (2010). Label-Free, Real-Time Monitoring of Biomass Processing with Stimulated Raman Scattering Microscopy. *Angewandte Chemie*, **49**, 5476–5479.

[106] Malinowska, K.H., Verdorfer, T., Meinhold, A., Funk, V., and Nash, M.A. (2014). Redox-Initiated Hydrogel System for Detection and Real-Time Imaging of Cellulolytic Enzyme Activity. Submitted for peer-review.

[107] Himmel, M.E., Ding, S.Y., Johnson, D.K., Adney, W.S., Nimlos, M.R., *et al.* (2007). Biomass recalcitrance: Engineering plants and enzymes for biofuels production. *Science*, **315**(5813), 804–807.

[108] Grashoff, C., Hoffman, B.D., Brenner, M.D., Zhou, R., Parsons, M., *et al.* (2010). Measuring mechanical tension across vinculin reveals regulation of focal adhesion dynamics. *Nature*, **466**(7303), 263–6.

[109] Wang, X. and Ha, T. (2013). Defining Single Molecular Forces Required to Activate Integrin and Notch Signaling. *Science*, **340**(6135), 991–994.

[110] Campàs, O., Mammoto, T., Hasso, S., Sperling, R.A., O'Connell, D., *et al.* (2014). Quantifying cell-generated mechanical forces within living embryonic tissues. *Nat Methods*, **11**, 183–189.

[111] Wienken, U. and Gaub, H.E. (2013). Stamping Vital Cells-a Force-Based Ligand Receptor Assay. *Biophys J*, **105**(12), 2687–94.

[112] Wolf, P. (2013). *Bringing the Molecular Force Assay to Microfluidics*. Master's thesis, Ludwig-Maximilians-Universität München.

[113] Larson, B.J., Gillmor, S., and Lagally, M.G. (2004). Controlled deposition of picoliter amounts of fluid using an ultrasonically driven micropipette. *Rev Sci Instrum*, **75**(4), 832–836.

[114] AndorTechnology (2012). *Spinning disk confocal microscopy*. Tech. rep.

[115] Alberts, B. (2008). *Molecular biology of the Cell*. Garland Science, 5th edn.

[116] Zubay, G. (1973). In vitro synthesis of protein in microbial systems. *Annu Rev Genet*, **7**, 267–87.

[117] Evans, E. and Ritchie, K. (1999). Strength of a weak bond connecting flexible polymer chains. *Biophys J*, **76**(5), 2439–2447.

[118] Morfill, J. (2005). *Hochauflösende Einzelmolekülkraftspektroskopie von doppelsträngiger DNA*. Master's thesis, Ludwig-Maximilians-Universität München.

List of Figures

Acknowledgments

I would like to **thank**...

Prof. Dr. **Hermann E. Gaub** for his encouraging and thoughtful supervision with space for own ideas and motivational pushes into the right directions,

Prof. Dr. **Stephen R. Quake** and Dr. **Matthias Meier** of Stanford University for invaluable help in setting up the microfluidic experiments and for a warm welcome at Stanford,

Daniela Aschenbrenner and Dr. **Katja Limmer** for enlightening scientific discussions about the molecular force assay and inspiring tea breaks with discussions beyond science, and Dr. **Philip Severin** for all the preliminary work, for sharing all his hands-on knowledge, experimental ideas and for kick-starting the microfluidics setup,

my co-authors Dr. **Michael Nash**, **Markus Jobst**, **Wolfgang Ott** for great, seam–less team–work, and my students **Anita Ladenburger**, **Philip Wolf**, **Magnus Bauer** for teaching me as much as I could hopefully teach them,

the technicians **Angelika Kardinal**, **Tom Nicolaus**, **Christian Holopirek**, **Philipp Altpeter**, and **Jürgen Aust** (and his machine shop crew) for impeccable work and for keeping the lab running, and the CeNS and NIM staff, in particular **Marilena Pinto** and **Dr. Susanne Hennig**, for their organizational support,

all current and former colleagues, in particular but not only, Dr. **Stephan Heucke**, **Fabian Baumann**, Dr. **Diana Pippig**, Dr. **Ingo Stein**, Dr. **Stefan Scheuer**, **Jochen Müller** (thanks for the fruitful discussions about cytoskeleton mechanics!), **Tobias Verdorfer** (good to know the microfluidics in your hands!), **Constantin Schöler**, and the rest of the Lehrstuhl Gaub for an inspiring and fun working atmosphere,

my former teachers Prof. Dr. **David A. Weitz**, Prof. Dr. **Joachim Rädler**, and Prof. Dr. **Friedrich C. Simmel** for instilling and nurturing the fascination for biophysics,

and, last but not least, I would like to thank my family and friends for endless support and encouragement.

Curriculum vitae

Marcus Bernd Manuel Otten

Ich versichere, die Arbeit selbstständig angefertigt und dazu nur die im Literaturverzeichnis angegebenen Quellen benutzt zu haben.

München, den 18. Februar 2014